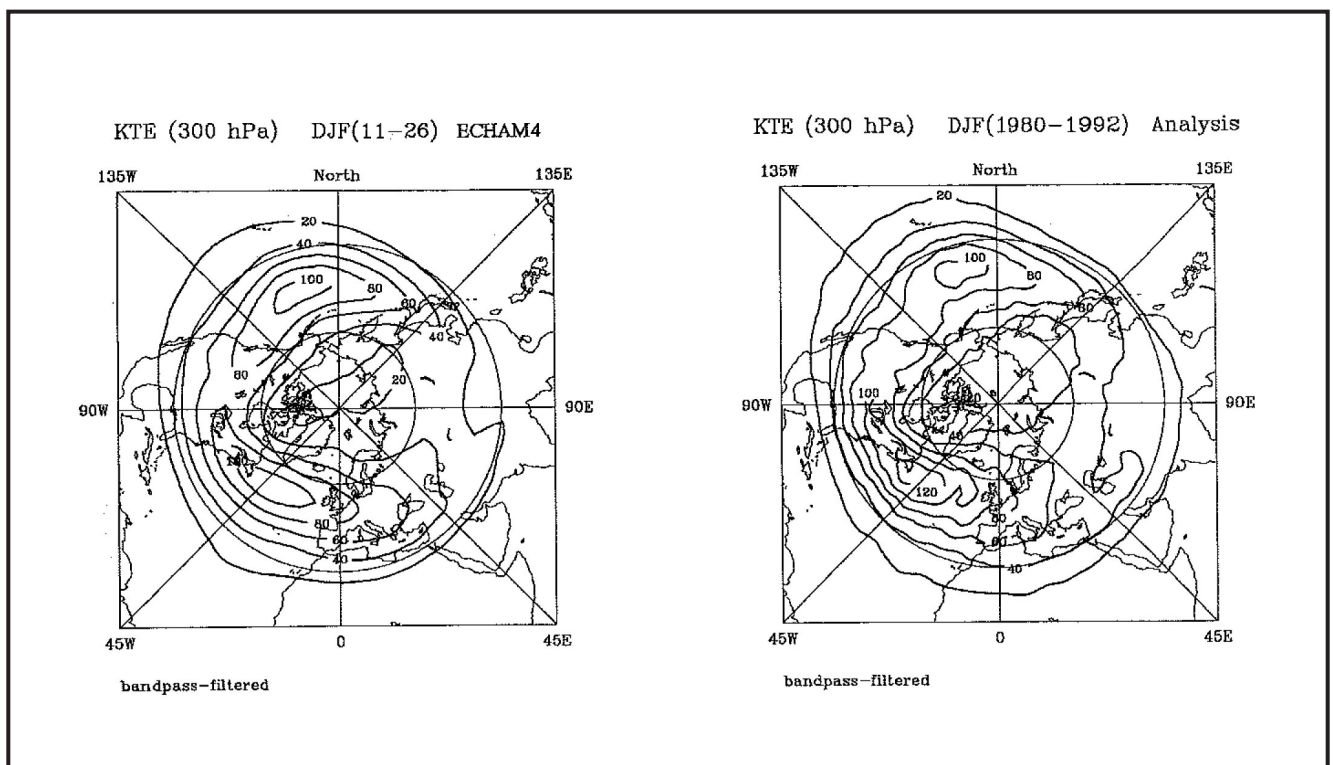# Max-Planck-Institut für Meteorologie

REPORT No. 218

THE ATMOSPHERIC GENERAL CIRCULATION MODEL ECHAM-4: MODEL DESCRIPTION AND SIMULATION OF PRESENT-DAY CLIMATE

by

E. Roeckner - K. Arpe - L. Bengtsson - M. Christoph - M. Claussen - L. Dümenil
M. Esch - M. Giorgetta - U. Schlese - U. Schulzweida

The atmospheric general circulation model ECHAM-4: Model description and simulation of present-day climate

E. Roeckner[1], K. Arpe[1], L. Bengtsson[1], M. Christoph[1], M. Claussen[3], L. Dümenil[1], M. Esch[1], M. Giorgetta[1], U. Schlese[2] and U. Schulzweida[1]

[1] Max-Planck-Institut für Meteorologie, Hamburg

[2] Deutsches Klimarechenzentrum (DKRZ), Hamburg

[3] Potsdam-Institut für Klimafolgenforschung (PIK), Potsdam

Abstract

A detailed description of the fourth-generation ECHAM model is presented. Compared to the previous version, ECHAM-3, a number of substantial changes have been introduced in both the numerics and physics of the model. These include a semi-Lagrangian transport scheme for water vapour, cloud water and trace substances, a new radiation scheme (ECMWF) with modifications concerning the water vapour continuum, cloud optical properties and greenhouse gases, a new formulation of the vertical diffusion coefficients as functions of turbulent kinetic energy, and a new closure for deep convection based on convective instability instead of moisture convergence. Minor changes concern the parameterizations of horizontal diffusion, stratiform clouds and land surface processes. Also, a new dataset of land surface parameters have been compiled for the new model.

The climatology of the model, derived from two extended AMIP simulations at T42L19 resolution, is documented and compared with ECMWF operational analyses. Some of the biases noted for the previous model version remain virtually unchanged. For example, the polar upper troposphere and lower stratosphere is much too cold, and the zonal wind errors become very large above the 200 hPa level. Furthermore, the low-frequency variability is still too small but the errors are reduced by about 50% compared to ECHAM-3. The tropospheric temperature and zonal wind errors are generally smaller than in the previous model, except for the tropics, where the overestimation of Walker-type circulations in the equatorial plane is even more pronounced in the new model and the simulation of the Indian summer monsoon is less realistic. The most substantial improvements, compared to ECHAM-3, are found for the land surface climate. The temperature and precipitation errors are generally smaller than before, and the biome distributions derived from these parameters are more realistic in ECHAM-4. These improvements can be attributed to an improved represention of surface radiation fluxes via larger absorption of solar radiation in the atmosphere due to both water vapour and clouds.

1.   INTRODUCTION

The fourth-generation atmospheric general circulation model (ECHAM-4) developed at the Max Planck Institute for Meteorology (MPI) is the most recent in a series evolving originally from the spectral weather prediction model of the European Centre for Medium Range Weather Forecasts (ECMWF; Simmons et al., 1989). This new model has still many features in common with the current ECMWF model, but some of the physical parameterizations have either been replaced or modified for climate applications. Furthermore, different from the current operational ECMWF model which employs a semi-Lagrangian advection scheme for all variables, ECHAM-4 still uses the spectral transform method for 'dry dynamics' while only water vapour, cloud water and trace constituents are advected by using a shape preserving semi-Lagrangian scheme (Williamson and Rasch, 1994).

The motivation for developing ECHAM-4 was to overcome a number of limitations of the previous model version, in particular,

- to eliminate the most apparent shortcomings of the previous version ECHAM-3 (Roeckner et al., 1992), due partly to using the spectral transform method for positive definite variables like water vapour and cloud water, but primarily due to deficiencies of the physical parameterizations resulting, for example, in a poor reproduction of the land surface climate due to a deficient simulation of the surface radiation fluxes (Wild et al., 1995),

- to allow for including the transport (both large-scale and subgrid-scale) of atmospheric trace gases and aerosols,

- to allow for calculating the radiative effect of all relevant greenhouse gases and aerosols, and

- to improve the physical basis of the model in general.

A short summary of design and performance of ECHAM-4 can be found in Roeckner and Arpe (1995). Moreover, a number of validation studies using satellite data, in general, but also in-situ measurements have been published, such as those on the ECHAM-4 water vapour distribution (Chen et al., 1996), top-of-atmosphere radiation fluxes (Chen and Roeckner, 1996a), cloud cover (Chen and Roeckner, 1996b), surface radiation fluxes (Wild et al., 1996), tropospheric and stratospheric temperature fluctuations (Stendel and Bengtsson, 1996) and on the interaction between SST, convection and water vapour during the Central Equatorial Pacific Experiment (Lohmann et al., 1995).

ECHAM-4 has also been coupled to an ocean general circulation model (OPYC, Oberhuber, 1993), and the simulated ENSO dynamics in the upper ocean as well as the atmospheric response are documented in Bacher et al. (1996) and Roeckner et al. (1996), respectively. The atmospheric sulfur cycle has been implemented and studied by Feichter et al. (1996), and a 39-layer middle

atmosphere version with top at 0.01 hPa has been developed by Manzini et al. (1996).

In this report, only the standard L19 version of ECHAM-4 is documented. The extended versions have partly been described in the studies mentioned above. In addition to the T42 simulations presented in this study, analogous experiments have been performed at both lower resolution (T21 and T30) and higher resolution (T106). The impact of these changes in horizontal resolution on the simulated climate is subject of a separate study (Arpe et al., 1996).

In the first part of this report, the physics of the standard ECHAM-4 model is described in some detail, with emphasis on those parts which have been changed compared to the previous model version. In the second part, the climate statistics of ECHAM-4/T42L19 as derived from two extended AMIP-type realizations (**A**tmospheric **M**odel **I**ntercomparison **P**roject; Gates, 1992) with prescribed monthly mean SST and sea ice limits from 1979 to 1994 is analysed and compared to ECMWF operational analyses for about the same period.

2. MODEL STRUCTURE

The model structure of ECHAM-4, including dynamics and numerics, is in most parts identical to that of ECHAM-3, documented in detail in Roeckner et al. (1992) and DKRZ (1992). Therefore, only the main features are summarized here.

The model is based on the primitive equations. Prognostic variables are vorticity, divergence, logarithm of surface pressure, temperature, specific humidity, mixing ratio of total cloud water (liquid and ice phase together) and, optionally, a number of trace gases and aerosols. Except for the water components and trace substances, the prognostic variables are represented by truncated series of spherical harmonics with triangular truncation at wavenumber 42 (T42) in the standard version. Nonlinear terms and most of the parameterized physics is calculated on the associated Gaussian transform grid which has a resolution of about 2.8° x 2.8° in latitude and longitude. A semi-implicit time stepping scheme is used together with a weak time filter to avoid a decoupling of the solutions at the two time levels of the time stepping scheme. The time step is 24 minutes for dynamics and physics, except for radiation which is calculated at 2-hour intervals. The vertical domain extends up to a pressure level of 10 hPa, corresponding to a height of approximately 30 km. A hybrid sigma-pressure coordinate system is used (Simmons and Strüfing, 1981) with 19 irregularly spaced levels and with the highest resolution in the atmospheric boundary layer. The lowest level is placed at a height of about 30 m above the surface which corresponds roughly to the height of the surface layer. The upper part of the boundary layer, up to a height of about 1.5 km above the surface, is resolved by four additional levels . Both seasonal and diurnal cycles in solar forcing are simulated.

Different from ECHAM-3, the three-dimensional transport of water vapour, cloud water and trace constituents is calculated by using a semi-Lagrangian scheme. The scheme has been

developed by Williamson and Rasch (1994) for use in the NCAR CCM2 (Hack et al., 1993). The scheme uses a shape preserving interpolation form which avoids the generation of spurious minima or maxima. Therefore, other than the spectral tranform method, the semi-Lagrangian scheme does not produce negative values or spurious rain through generation of supersaturation by the transport of water vapour. However, the scheme is not inherently conservative, and mass conservation has to be enforced by a 'conservation fixer' applied at every timestep through a variational adjustment of the respective variable which weights the amplitude of the adjustment in proportion to the advection tendencies and the field itself (Rasch and Williamson, 1990).

Most of the land surface data are prescribed invariably during the course of the integration such as orography, background albedo, roughness length, vegetation type, leaf area index and soil parameters like water holding capacity, heat capacity and thermal conductivity. A new dataset of annual mean land surface parameters has been compiled for ECHAM-4 (Claussen et al., 1994), consistent with the Olson et al. (1983) definition of ecosystem complexes. The generation procedure is outlined in Appendix A.

3.   MODEL PHYSICS

Compared to the previous version, ECHAM-4 has undergone a number of partly substantial changes in the physical parameterizations which are summarized below.

1. Horizontal diffusion: Within the troposphere, horizontal diffusion is parameterized by a high-order scheme (∇^{10}) which essentially confines the damping to the high-wavenumber end of the spectrum, in a way similar to ECHAM-3 where a ∇^4 operator is applied only beyond a specified cut-off wavenumber. To avoid fictituous reflection at the upper boundary, a high-diffusion sponge zone is realized through a gradual decrease of the order of the scheme in the lower stratosphere, i.e., from 10 within the whole troposphere down to 2 at the upper two model layers. Independent of height, the damping time scale of the highest resolvable wavenumber is about 9 hours (at T42 resolution). The diffusion operator is applied to all wavenumbers, but not to those variables which are advected by means of the semi-Lagrangian scheme, i.e., the water components and trace constituents.

2. Surface fluxes and vertical diffusion: As in ECHAM-3, the turbulent fluxes at the surface are calculated from Monin-Obukhov similarity theory. However, different from ECHAM-3, a higher-order closure scheme is used to compute the turbulent transfer of momentum, heat, moisture, cloud water and tracers within and above the atmospheric boundary layer. The eddy diffusion coefficients are calculated as functions of the turbulent kinetic energy E which is obtained from the respective rate equation (Brinkop and Roeckner, 1995), including turbulent transport of E, generation/destruction by wind shear and buoyancy flux, and dissipation (but neglecting advection of E). The interaction between cloud and turbulence is represented by processes such as the vertical exchange of turbulent kinetic energy generated through radiative

cooling at cloud top, the impact of cloud water on the buoyancy flux, and cloud top entrainment through the turbulent flux of cloud water.

3. Land surface processes: With a minor exception, land surface processes are parameterized as in ECHAM-3. The soil model comprises the budgets of heat and water in the soil, the snow pack over land and the heat budget of land ice. Vegetation effects such as the interception of rain and snow in the canopy and the stomatal control of evapotranspiration are parameterized in a highly idealized way. The local runoff scheme is based on catchment considerations and takes into account subgrid-scale variations of field capacity over inhomogeneous terrain. The only change in the scheme is related to a new dataset of spatially varying water holding capacity of the soil (see Appendix A). To avoid fictituous evaporation in those areas where the water holding capacity is large, the total reservoir is split into two parts, and only water from the upper reservoir is accessible to evaporation in the non-vegetated part of a grid box.

4. Gravity wave drag: This parameterization remains unchanged. Drag associated with orographic gravity waves is simulated after the method of McFarlance (1987) and Palmer et al. (1986), as modified by Miller et al. (1989), using directionally dependent subgrid-scale orographic variances obtained from a high-resolution U.S. Navy dataset. Surface stress due to gravity waves excited by stably stratified flow over irregular terrain is calculated from linear theory and dimensional considerations. The surface wave stress is a function of low-level wind, orographic variance and buoyancy frequency. In addition, high-drag states are considerd when the flow becomes hydraulic at low levels due to the breaking of lee waves. The vertical profile is calculated from a local wave Richardson which describes the onset of turbulence due to convective instability and the turbulent breakdown approaching a critical level.

5. Cumulus convection: As in ECHAM-3, the parameterization of cumulus convection (shallow, mid-level, and deep), is based on the bulk mass flux concept of Tiedtke (1989). However, according to the suggestions of Nordeng (1996), organized entrainment is related to buoyancy instead of moisture convergence, organized detrainment is computed for a spectrum of clouds detraining at different heights, and an adjustment-type closure is used for deep cumulus convection instead of the moisture convergence closure applied in ECHAM-3. Moreover, the water loading is now considered in the buoyancy calculation, the cloud water detrained at the top of cumulus clouds is entering as a source term in the stratiform cloud water equation (see 6.), and the physics of the stratocumulus regime is now part of the boundary layer scheme (see 2.).

6. Stratiform clouds: As in ECHAM-3, the stratiform cloud water content is calculated from the respective budget equation including sources and sinks due to phase changes and precipitation formation by coalescence of cloud droplets and gravitational settling of ice crystals. Different from ECHAM-3, the convective cloud water detrained at the top of cumulus clouds is used as a source term in the stratiform cloud water equation (see 5.). The formation of thin maritime stratus forming under a low-level inversion is favoured by accounting for subgrid-scale cloudiness in the vertical, realized through a reduction of condensation threshold and saturation limit below the inversion.

7. Radiation: The radiation code has been adopted from the ECMWF model (Fouquart and Bonnel, 1980; Morcrette et al., 1986) with a few modifications like the consideration of additional greenhouse gases (methane, nitrous oxide and 16 CFCs), the 14.6 μm band of ozone and various types of aerosols (optionally). Moreover, the water vapour continuum has been revised to include temperature weighted band averages of e-type absorption and also a band dependent ratio of (p-e)-type to e-type continuum absorption (Giorgetta and Wild, 1995). The single scattering properties of cloud droplets and ice crystals are derived from Mie theory with suitable adaptation to the broad-band model (Rockel et al., 1991), and the effective radius of droplets and ice crystals is parameterized in terms of the liquid and ice water content, respectively (Roeckner, 1995).

3.1. HORIZONTAL DIFFUSION

Different from the other parameterizations which are computed in grid point space, the horizontal diffusion is formulated in spectral space. Moreover, the treatment of horizontal diffusion differs from that of the other processes in that it does not involve a physical model of subgrid-scale processes, but rather a numerically convenient form of scale selective diffusion with coefficients determined empirically to ensure a realistic behavior of the resolved scales. As in many other models, the horizontal diffusion tendency is expressed in the form of a hyper-Laplacian,

$$\frac{\partial \chi}{\partial t} = -(-1)^q K_\chi \nabla^{2q} \chi \tag{1}$$

where χ is vorticity, divergence or temperature (no horizontal diffusion is applied to water components or trace constituents), K_χ is a constant diffusion coefficient for the respective variable, and q is a positive integer. In spectral space, for any wavenumber n,

$$\frac{\partial \chi_n}{\partial t} = -K_\chi \{n(n+1)a^{-2}\}^q \chi_n \tag{2}$$

where a is the Earth's radius. For convenience, K_χ is replaced by the e-folding damping time τ of the highest resolvable wavenumber n_0,

$$\tau(n_0) = \tau_0 = K_\chi^{-1} \{n_0(n_0+1)a^{-2}\}^{-q} \tag{3}$$

so that (2) can be expressed in terms of the order of the scheme ($2q$) and damping time τ_0. The scale selectivity of the scheme increases with increasing q.

At T42 resolution, a high-order scheme ($2q = 10$) is applied throughout the troposphere. However, in order to prevent spurious wave reflection at the upper model boundary, the diffusion

is enhanced in the upper layers by gradually decreasing the order of the scheme with height, from $2q = 10$ below level 6 (about 150 hPa) to $2q = 2$ in the upper two levels. A damping time of $\tau_0 = \tau(n_0{=}42) = 9$ hours is prescribed at all model levels, so that the diffusion coefficient can be calculated from (3).

3.2. SURFACE FLUXES AND VERTICAL DIFFUSION

The turbulent flux of a variable χ at the surface is calculated according to the bulk transfer relation

$$\overline{(w'\chi')}_S = -C_\chi |V_L|(\chi_L - \chi_S) \tag{4}$$

where C_χ is the transfer coefficient. The subscripts L and S refer to values at the lowest model level (representing the top of the surface layer) and the surface, respectively, and V_L is the horizontal wind vector at level L. The transfer coefficients are obtained from Monin-Obukhov similarity theory by integrating the flux-profile relationships over the lowest model layer. As in the ECMWF model, approximate analytical expressions derived by Louis (1979) are employed, differently for momentum (subscript m) and heat (subscript h: used for water vapour, cloud water and tracers as well)

$$C_{m,h} = C_N \cdot f_{m,h}\left(Ri_B, \frac{z_L}{z_{0m}} + 1, \frac{z_L}{z_{0h}} + 1\right) \tag{5}$$

$$C_N = \frac{k^2}{\ln\left(\frac{z_L}{z_{0m}} + 1\right) \cdot \ln\left(\frac{z_L}{z_{0h}} + 1\right)} \tag{6}$$

where C_N is the neutral transfer coefficient, k the van Kármán constant, z_L the height of the lowest model level, z_{0m} and z_{0h} the roughness length for momentum and heat, respectively, and Ri_B the 'moist' bulk Richardson number of the surface layer, defined in terms of cloud conservative variables (total water content and liquid water potential temperature; e.g., Smith, 1990; Brinkop and Roeckner, 1995). The stability functions for momentum and heat, f_m and f_h, which represent the ratio of $C_{m,h}$ to their respective values under neutral conditions, are defined according to Louis (1979) for unstable conditions ($Ri_B < 0$)

$$f_{m,h} = 1 - \frac{a_{m,h} Ri_B}{1 + 3c^2 C_N \sqrt{-Ri_B \cdot \left(\frac{z_L}{z_{0m}} + 1\right)}} \tag{7}$$

and for stable conditions ($Ri_B \geq 0$)

$$f_m = \frac{1}{1 + a_m Ri_B / \sqrt{1 + cRi_B}} \tag{8}$$

$$f_h = \frac{1}{1 + a_h Ri_B \sqrt{1 + cRi_B}} \tag{9}$$

with coefficients specified as $c = 5, a_m = 2c, a_h = 3c$.

Over land, the roughness length is specified as a function of subgrid-scale orography and vegetation (see Appendix A). Over open water, the aerodynamic roughness length z_{0m} is computed from the formula (Charnock, 1955)

$$z_{0m} = max\ (0.032\ u_*^2/g, 1.5 \times 10^{-5}\ m) \tag{10}$$

where u_* is the friction velocity and g the acceleration of gravity. Over sea ice, a constant value of 10^{-3} m is prescribed for both z_{0m} and z_{0h}. For the transfer of heat and water vapour over sea, the Charnock relation is modified slightly. Different from the momentum transfer which is affected by pressure fluctuations in the turbulent wakes behind the roughness elements, heat and water vapour must be transferred by molecular diffusion across the interfacial sublayer. Observational data (Large and Pond, 1982) suggest that the transfer coefficients for heat and water vapour are largely independent of wind speed. In the model, these empirical results are taken into account by a suitable reduction of the aerodynamic roughness length over sea (10) according to

$$z_{0h} = z_{0m}\ exp\{2. - 86.276\ z_{0m}^{0.375}\} \tag{11}$$

For low wind speed, free convection conditions must prevail. Therefore, in unstable conditions over sea, an empirical interpolation is used between the free convection limit and the neutral approximation (Miller et al., 1992)

$$C_h = C_N (1 + C_R^\gamma)^{1/\gamma} \tag{12}$$

$$C_R = \beta \frac{(\Delta \Theta_v)^{1/3}}{C_N |V_L|} \tag{13}$$

with $\beta = 0.0016$ and $\gamma = 1.25$. $\Delta \Theta_v$ represents the virtual potential temperature difference between the surface and the lowest model level L.

Above the surface layer, the eddy diffusion method is applied, and the vertical turbulent fluxes are related to the gradient of the respective variable according to

$$\overline{w'\chi'} = -K_\chi \frac{\partial \chi}{\partial z} \tag{14}$$

where K_χ is the vertical eddy diffusion coefficient. Analogous to the surface layer, different coefficients are used for momentum and heat. The eddy viscosity K_m and eddy diffusivity K_h are parameterized in terms of the turbulent kinetic energy E (e.g., Garrat, 1992)

$$K_{m,h} = \Lambda_{m,h} \sqrt{E} \tag{15}$$

with $E = (u'^2 + v'^2 + w'^2)/2$ and length scales $\Lambda_{m,h} = l\, S_{m,h}$, where $l = kz(1 + kz/\lambda)^{-1}$ is the mixing length (Blackadar, 1962). The asymptotic mixing length λ is set constant (300 m) for both heat and momentum throughout the atmospheric boundary layer. In the free atmosphere, λ is assumed to decrease exponentially with height, approaching about 30m in the upper troposphere (Holtslag and Boville, 1993). Analogous to the transfer coefficients in the surface layer, the functions $S_{m,h}$ are defined as a product of neutral coefficients S_{Nm}, S_{Nh} for momentum and heat, respectively, and stability functions $g_{m,h}$,

$$S_m = S_{N,m} \cdot g_m \tag{16}$$

$$S_h = S_{N,h} \cdot g_h \tag{17}$$

where the neutral coefficients are defined according to Mellor and Yamada (1982)

$$S_{Nh} = 3A_2 \gamma_1 \sqrt{2} \tag{18}$$

$$\frac{S_{Nm}}{S_{Nh}} = \frac{A_1}{A_2}\left(\frac{\gamma_1 - C_1}{\gamma_1}\right) \tag{19}$$

with $A_1 = 0.92$, $A_2 = 0.74$, $B_1 = 16.6$, $C_1 = 0.08$ and $\gamma_1 = 1/3 - 2A_1/B_1$.

The stability functions $g_{m,h}$ are defined consistently with $f_{m,h}$ in the surface layer (cf., (7)-(9) and Roeckner et al., 1992), so that for unstable conditions ($Ri_B < 0$),

$$g_{m,h} = 1 - \frac{a_{m,h} Ri_B}{1 + 3c^2 l^2 \left[\left(\frac{\Delta z}{z} + 1\right)^{1/3} - 1\right]^{3/2} \cdot \left[\frac{\sqrt{-Ri_B}}{(\Delta z)^{3/2}\sqrt{z}}\right]} \tag{20}$$

and for stable conditions ($Ri_B \geq 0$),

$$g_m = \frac{1}{1 + 2cRi_B/\sqrt{1 + cRi_B}} \tag{21}$$

$$g_h = \frac{1}{1 + 2cRi_B\sqrt{1 + Ri_B}} \tag{22}$$

where z is height, Δz the layer thickness, and Ri_B the 'moist' bulk Richardson number for the respective model layer. Different from ECHAM-3, vertical diffusion in the free atmosphere is

9

also calculated in stable stratification.

A simplified form of the turbulent kinetic equation is solved, as described by Brinkop and Roeckner (1995), with advection of E neglected,

$$\frac{\partial E}{\partial t} = -\frac{\partial}{\partial z}(\overline{w'E} + \overline{w'p'}/\rho) - \overline{u'w'}\frac{\partial u}{\partial z} - \overline{v'w'}\frac{\partial v}{\partial z} + \frac{g}{\Theta_v}\overline{w'\Theta'}_v - \varepsilon \qquad (23)$$

All turbulent fluxes in (23) are computed from (14), with coefficients according to (15). $K_E = K_m$ is used for computing the turbulent transport of E (first term, where $w'p'$ /ρ is the pressure correlation term and ρ is density), for computing the shear terms as well as for the buoyancy flux $g(\overline{w'\Theta'_v})/\Theta_v$ which is formulated in terms of total water content and liquid water potential temperature (Brinkop and Roeckner, 1995). As usual, the dissipation rate is set $\varepsilon = E^{3/2}/\Lambda_1$ with a dissipation length of $\Lambda_1 = 15\ l$. The solution of (23) requires the specification of a surface boundary condition for E. Here, the formulation of Mailhot and Benoit (1982) is adopted, and the turbulent kinetic energy close to the surface is defined as

$$E_0 = 3.75\ u_*^2 \text{ (stable surface layer)} \qquad (24)$$
$$E_0 = 3.75\ u_*^2 + 0.2\ w_*^2 + (-z_L/L_{MO})^{2/3}\ u_*^2 \text{ (unstable surface layer)} \qquad (25)$$

where $w_* = \{gH(\overline{w'\Theta'_v})_s/\Theta_{vs}\}^{1/3}$ is a convective velocity scale, L_{MO} the Monin-Obukhov length, and H the height of the boundary layer. The surface buoyancy flux $(\overline{w'\Theta'_v})_s$ is computed according to (4)-(13).

3.3. LAND SURFACE PROCESSES

The parameterization of the land surface processes comprises the evolution of the temperature profile in the soil, the soil hydrology and the snow pack over land. Apart from a few changes described below, the scheme is identical to that used in ECHAM-3. Therefore, only its basic features are summarized in this Section. A comprehensive documentation can be found in Roeckner et al. (1992).

The temperature profile in the soil (or in the glacier if present), is calculated from a numerical solution of the heat conduction equation in a five-layer model where the thicknesses of the individual layers increase with depth (from 0.065m for the upper layer to 5.7m for the lowest one). At the lower boundary of the domain, i.e., at a depth of 10m approximately, a zero heat flux condition is imposed in order to close the energy budget of the Earth-atmosphere system.

For snow depths over land which exceed a threshold of 0.025m water equivalent, the heat conduction equation is solved for an extra layer, and the skin temperature of the snow, which serves as an interface to the atmosphere, is obtained through linear extrapolation from the snow

layer and the upper soil layer. This temperature may not exceed the snow melt temperature. If this would occur, the excess energy is first used to warm the soil underneath. Only if both the snow temperature and the upper soil temperature reach the melting point, further energy input will be used to melt the snow.

The sea-ice temperature is obtained from the total heat flux at the ice surface and the heat conduction through the slab, where the ocean temperature below the slab is fixed at the freezing point for seawater. The ice surface temperature calculated accordingly is representive for the upper 10cm of the slab. As in ECHAM-3, snow falling on sea ice is disregarded.

The parameterization of soil hydrology comprises the budget equations for snow amount, water amount intercepted by the vegetation during rain or snow melt episodes (the so-called skin reservoir) and the water amount in the soil. In these equations, processes such as evaporation, snowmelt, snowfall and rainfall link the soil hydrology to fluxes of water estimated from the parameterizations of the turbulent surface fluxes (Section 3.2) and precipitation formation (Sections 3.5 and 3.6). In nature, and in some coupled atmosphere-ocean models as well, the water cycle is closed through local runoff and rivers which direct the local runoff into the oceans. As in ECHAM-3, and in atmospheric models in general, the water cycle is not closed in ECHAM-4. While local runoff is considered in the water budget through surface runoff, including subgrid-scale effects due to the heterogeneity of the soil, and drainage processes (Dümenil and Todini, 1992), the river runoff is disregarded. Rainwater falling on frozen soil is not allowed to infiltrate but is assumed to run off completetely.

As mentioned earlier, a new set of surface data has been compiled as input for ECHAM-4 (see Appendix A). These parameters are relevent for the heat and water budget of the soil, such as the vegetation index, the heat diffusivity and heat capacity of the soil, and the water holding capacity of the soil. While the latter has been specified in ECHAM-3 as a global constant ($w_{max} = 0.2$m), it varies spatially in ECHAM-4 (Patterson, 1990), ranging from a few centimeters to about one meter, which requires reformulation of evaporation from the soil.

In ECHAM-3, the soil water available for evaporation in the non-vegetated part of a grid box is defined in terms of a 'relative soil water amount' h, in the limits $0 \leq h \leq 1$ for $0 \leq w \leq w_{max}$, where w is the actual soil water amount,

$$h = \left[1 - \cos\left(\pi \cdot \frac{w}{w_{max}} \right) \right] / 2 \qquad (26)$$

According to (26), since $w_{max} = const$ in ECHAM-3, h is completely determined by w so that, for a given set of atmospheric parameters, the evaporation from the soil is a unique function of the water level. In ECHAM-4 this is no longer the case, and unrealistically large evaporation rates could be expected at grid points with large w_{max}. To avoid evaporation from a deep layer, the total reservoir w_{max} is split into two parts, an upper layer w_{top} and a lower one $w_{max} - w_{top}$. In the non-vegetated part of a grid box, only water from the upper reservoir should be accessible

for evaporation. In order to fulfil this requirement, (26) has been reformulated according to

$$h = \left[1 - \cos\left\{\pi \cdot \frac{w - (w_{max} - w_{top})}{w_{top}}\right\}\right] / 2 \qquad (27)$$

for $w > w_{max} - w_{top}$, and $h = 0$ otherwise. The upper reservoir is specified as $w_{top} = 0.1$m for $w_{max} > 0.1$m and $w_{top} = w_{max}$ otherwise. In the latter case, (27) becomes identical to (26).

3.4. GRAVITY WAVE DRAG

The parameterization scheme represents the momentum transport due to subgrid-scale gravity waves exited in stably stratified flow over irregular terrain (Miller et al., 1989). Depending on the atmospheric stability and vertical wind shear, these waves can propagate to high altitudes unless absorbed and/or reflected by critical layers, or unless break as a result of convective or shear instabilities. The scheme is a modified form of that proposed by Palmer et al. (1986) and McFarlane (1987) in which a low-level wave stress is defined together with criteria for the reduction in stress with height as the upward propagating waves are absorbed and/or reflected. Since the scheme used in the new model is identical to that used in ECHAM-3, and documented in Roeckner et al. (1992), only its basic features are summarized here.

The scheme consists of two parts, first a formulation of the surface pressure drag exerted on the subgrid-scale orography and second a modelling of the dissipation/absorption processes which determine the vertical distribution of the wave stress accompanying the surface value. The surface wave stress depends on the low-level Brunt-Väisälä frequency, the low-level horizontal wind and on the subgrid-scale orographic variance. To account for the anisotropic nature of orography, a directional variance has been computed in four sectors (E/W, N/S, NW/SE and NE/SW), but limited according to dynamical constraints. An additional drag is considered when the flow becomes hydraulic at low levels due the breaking of lee waves. The drag below a low-level reference height (corresponding to a pressure of $0.8p_s$, where p_s is surface pressure) represents the effect of low-level wave ducting. The high-level drag is a result of upward wave propagation depending on a local wave Richardson number which attempts to describe the onset of turbulence due to gravity waves becoming convectively unstable or encountering a critical layer. By requiring that the wave Richardson number never falls below a critical value (0.25), values of wave stress are defined progressively from the surface upwards.

3.5. CUMULUS CONVECTION

Cumulus convection is parameterized by a mass flux scheme (Tiedtke, 1989), with modifications according to Nordeng (1996). The contribution of cumulus convection to the large scale budgets of heat, moisture and momentum is represented by an ensemble of clouds

consisting of updrafts and donwdrafts in a steady state. The bulk equations for mass, heat, moisture, cloud water and momentum for an ensemble of cumulus updrafts are

$$\frac{\partial M_u}{\partial z} = E_u - D_u \tag{28}$$

$$\frac{\partial}{\partial z}(M_u s_u) = E_u \bar{s} - D_u s_u + L \bar{\rho} c_u \tag{29}$$

$$\frac{\partial}{\partial z}(M_u q_u) = E_u \bar{q} - D_u q_u - \bar{\rho} c_u \tag{30}$$

$$\frac{\partial}{\partial z}(M_u l_u) = -D_u l_u + \bar{\rho} c_u - \bar{\rho} P_u \tag{31}$$

$$\frac{\partial}{\partial z}(M_u u_u) = E_u \bar{u} - D_u u_u \tag{32}$$

$$\frac{\partial}{\partial z}(M_u v_u) = E_u \bar{v} - D_u v_u \tag{33}$$

where the subscript u denotes updraft variables and the overbar denotes large-scale variables. E is entrainment, D is detrainment, $s=c_p T+gz$ the dry static energy, ρ the air density, q is specific humidity, l the cloud water mixing ratio, c_u the release of latent heat from condensation, P_u the conversion of cloud water to precipitation, and u and v are the components of the horizontal wind vector.

As in ECHAM-3, a corresponding set of equations is used for the cumulus downdrafts which are assumed to originate from mixing of cloud air with environmental air which has been cooled to its wet bulb temperature by evaporation of precipitation generated in the updrafts (Tiedtke, 1989). Features common to both models are also the parameterizations of turbulent entrainment/detrainment, generation and evaporation of precipitation, melting of snow, and the treatment of shallow and mid-level convection.

Different in ECHAM-4 is the treatment of cloud water detrainment in (31), which is used as a source term, $D_u l_u / \bar{\rho}$, in the stratiform cloud water equation (54), while in ECHAM-3 the convective cloud water detrained into the environment is assumed to evaporate instantaneously. Different is also the treatment of stratocumulus clouds. In ECHAM-3, convection associated with the formation of stratocumulus clouds at the top of the boundary layer is parameterized as a turbulent diffusion process with an ad hoc enhancement of the vertical diffusion coefficients. In the new model, the stratocumulus regime is considered as part of the boundary layer scheme (see Section 3.2) which includes the effect of clouds on vertical transport, such as the downward transfer of turbulent kinetic energy generated through radiative cooling at cloud top, the impact of cloud water on the buoyancy flux, as well as cloud top entrainment processes represented by the turbulent diffusion of cloud liquid water (Brinkop and Roeckner, 1995).

Major changes in the ECHAM-4 convection scheme are related to the formulations of organized entrainment, organized detrainment and to an adjustment-type closure for deep cumulus clouds

(Nordeng, 1996), replacing that based on moisture convergence.

3.5.1 Organized entrainment

In Tiedtke (1989), organized entrainment is consistent with the closure and is based on a moisture convergence hypothesis, while Nordeng (1996) assumes organized entrainment to take place as inflow of air into the cloud when cloud parcels accelerate upwards, i.e., when the buoyancy is positive. Organized detrainment, on the other hand, takes place where the air decelerates, i.e., when the buoyancy is negative. Organized entrainment and detrainment are therefore related to the cloud activity itself.

By introducing fractional entrainment and detrainment rates, ε_i and δ_i (Turner, 1963), so that $E_i = M_i \varepsilon_i$ and $D_i = M_i \delta_i$ for an individual updraft i and, for the cloud ensemble,

$$E = M\varepsilon = \sum_i M_i \varepsilon_i = \sum_i E_i \tag{34}$$

$$D = M\delta = \sum_i M_i \delta_i = \sum_i D_i \tag{35}$$

where the cloud ensemble mass flux is defined as

$$M = \sum_i M_i = \sum_i \bar{\rho} \sigma_i w_i \tag{36}$$

with fractional area σ_i and vertical velocity w_i, (28) can be written as

$$\frac{1}{M} \frac{\partial M}{\partial z} = \varepsilon - \delta \tag{37}$$

where the subscript for the updraft u is omitted for convenience (in the following as well). According to Simpson and Wiggert (1969), the steady state vertical momentum equation for an individual updraft is given by

$$w_i \frac{\partial w_i}{\partial z} = b_i - \varepsilon_i w_i^2 \tag{38}$$

where b_i is the buoyancy term which may include water loading and non-hydrostatic effects. Assuming now that the fractional area σ_i of each individual updraft is constant with height (except in the ouflow part, see later), organized entrainment, according to (36) and (37), can be written as

$$\varepsilon_i = \frac{1}{M_i} \frac{\partial M_i}{\partial z} = \frac{1}{w_i} \frac{\partial w_i}{\partial z} + \frac{1}{\bar{\rho}} \frac{\partial}{\partial z} \bar{\rho} \tag{39}$$

whenever the buoyancy is positive ($\delta_i = 0$). By integrating (38) upwards, starting at cloud base ($z = 0$), and combining (34), (38) and (39), the organized entrainment rate of the cloud ensemble becomes

$$\varepsilon = \frac{b}{2\left(w_0^2 + \int_0^{\bar{z}} b\,dz\right)} + \frac{1}{\bar{\rho}}\frac{\partial}{\partial z}\bar{\rho} \tag{40}$$

with the ensemble buoyancy $b = \dfrac{g}{\bar{T}_v}(T_v - \bar{T}_v) - gl$.

3.5.2 Organized detrainment

Organized detrainment is the loss of total massflux due to detrainment of those clouds which are losing their buoyancy. By definition,

$$D = E - \frac{\partial M}{\partial z} = \sum_i \bar{\rho}\sigma_i w_i \left(\frac{1}{w_i}\frac{\partial w_i}{\partial z} + \frac{1}{\bar{\rho}}\frac{\partial}{\partial z}\bar{\rho}\right) - \frac{\partial}{\partial z}\sum_i \bar{\rho}\sigma_i w_i = -\sum_i \bar{\rho}w_i\frac{\partial\sigma_i}{\partial z} \tag{41}$$

Since the fractional area of each individual member of the ensemble is assumed to be constant with height, except for the detrainment level, the only contribution to the sum in (41) comes from those members of the ensemble which detrain at this level (k), i.e.,

$$D = -\sum_k \bar{\rho}w_k\frac{\partial\sigma_k}{\partial z} \approx \frac{\bar{\rho}\sigma_k w_k}{\Delta z} = \frac{M_k}{\Delta z} \tag{42}$$

where Δz is the depth over which the detrainment takes place. Thus, organized detrainment is equal to the change of mass flux with height. Since the in-cloud vertical velocities are primarily a function of the height above cloud base and, hence, $w_k \approx w$, and due to the assumption that individual clouds do not change their area fraction before they start to detrain, the individual cloud cover change is equal to the total, i.e.,

$$\frac{\partial\sigma_k}{\partial z} = \frac{\partial\sigma}{\partial z} \tag{43}$$

so that, according to (42) and (43), the organized detrainment may be parameterized as

$$D = -\frac{M}{\sigma}\frac{\partial\sigma}{\partial z} \tag{44}$$

It remains to determine the variation of cloud cover with height. Having obtained the level where clouds start to detrain (z_d), an analytical function $\sigma = \sigma(z)$ is specified with boundary valus $\sigma(z_d) = \sigma_0$ and $\sigma(z_t) = 0$, where z_t is the highest possible cloud level obtained from undiluted ascent starting at cloud base. In the parameterization, the spectrum of clouds detraining at different

levels is realized through the following function

$$\sigma(z) = \sigma_0 \cos\left[\frac{\pi}{2}\frac{(z-z_d)}{(z_t-z_d)}\right] \tag{45}$$

Other for being continuous at $z = z_d$, and satisfying the boundary conditions specified above, there is no physical reason for chosing this particular function.

3.5.3 Adjustment closure

As an alternative to the moisture-convergence closure for deep convective clouds used in the ECMWF model (and in ECHAM-3 as well), Nordeng (1996) developed an adjustment-type closure which relates the cloud base mass flux to convective instability. The dominant part of the convective heating and the convective drying, respectively, is due to compensating subsidence in the environment (Fritsch and Chappel, 1980), i.e.,

$$\frac{\partial}{\partial t}\bar{T} \approx \frac{1}{\bar{\rho}c_p}M\frac{\partial}{\partial z}\bar{s} \tag{46}$$

$$\frac{\partial}{\partial t}\bar{q} \approx \frac{1}{\bar{\rho}}M\frac{\partial}{\partial z}\bar{q} \tag{47}$$

where M is the massflux.

Convective activity is defined through the convective available potential energy ($CAPE$),

$$CAPE = \int\limits_{base}^{top} \left(\frac{g}{\bar{T}v}[T_v - \bar{T}v] - gl\right) dz \tag{48}$$

where cloud ensemble values are used for T_v and l. The change of $CAPE$ due to convective heating/moistening is approximated by

$$\frac{\partial}{\partial t}CAPE \approx -\int\limits_{base}^{top}\frac{g}{\bar{T}v}\frac{\partial\bar{T}v}{\partial t}dz = -M_B\int\limits_{base}^{top}\left(\frac{[1+\delta\bar{q}]}{c_p\bar{T}v}\frac{\partial}{\partial z}\bar{s} + \delta\frac{\partial}{\partial z}\bar{q}\right)\eta\frac{g}{\bar{\rho}}dz \tag{49}$$

with normalized mass flux η defined as $M = M_B\eta(z)$ where M_B is the cloud base mass flux. Assuming a relaxation time τ, so that

$$\frac{\partial}{\partial t}CAPE = -\frac{CAPE}{\tau} \tag{50}$$

the cloud base mass flux can be computed from (49),

$$M_B = \frac{CAPE}{\tau} \cdot \left\{ \int\limits_{base}^{top} \left[\frac{(1+\delta\bar{q})}{c_p\bar{T}v} \frac{\partial}{\partial z}\bar{s} + \delta\frac{\partial}{\partial z}\bar{q} \right] \eta \frac{g}{\bar{\rho}} dz \right\}^{-1} \tag{51}$$

Since η is not known before the total mass flux is known, *CAPE* is estimated through a first guess $M_B = M_B^*$ obtained, for example, from applying the moisture convergence scheme. The cloud base mass flux necessary for the adjustment closure can then be found according to

$$M_B = \frac{CAPE}{\tau} \cdot M_B^* \cdot \left\{ \int\limits_{base}^{top} \left[\frac{(1+\delta\bar{q})}{c_p\bar{T}v} \frac{\partial}{\partial z}\bar{s} + \delta\frac{\partial}{\partial z}\bar{q} \right] M_B^* \cdot \frac{g}{\bar{\rho}} dz \right\}^{-1} \tag{52}$$

As discussed by Nordeng (1996), the relaxation time τ should become smaller with increasing horizontal resolution and vice versa. In ECHAM-4, a value of $\tau = 3600$ s is used at T42 resolution.

3.6. STRATIFORM CLOUDS

The scheme is based on the approach of Sundqvist (1978) who developed a formalism to include fractional cloud cover (b) in a prognostic scheme. The governing equations for water vapour (q_v) and cloud water (q_w, liquid and ice phase together) are

$$\frac{\partial q_v}{\partial t} = R(q_v) - bC_c - (1-b)C_0 + (1-b)E_0 \tag{53}$$

$$\frac{\partial q_w}{\partial t} = R(q_w) + bC_c + (1-b)C_0 - bP_c \tag{54}$$

where $R(q_v), R(q_w)$ denote the sum over all transport terms of q_v and q_w, respectively, including advection, turbulence and convection (i.e., water vapour and cloud water detrained at the top of cumulus clouds, see Section 3.5). The subcripts c and 0 refer to the cloudy and cloud-free part of a grid box, respectively. The cloud-microphysical terms are condensation of water vapour in the cloudy part ($C_c > 0$), evaporation of cloud water ($C_c < 0$), evaporation of cloud water transported into the cloud-free part of a grid box ($C_0 < 0$), formation of precipitation by coalescence of cloud droplets and sedimentation of ice crystals (P_c), and the evaporation of precipitation falling into the unsaturated part of a grid box (E_0). Fractional cloud cover b is parameterized as a non-linear function of grid-mean relative humidity r (Sundqvist et al., 1989). For $r > r_0$, where $r_0 < r_{sat}$ is a subgrid-scale condensation threshold and r_{sat} ($=1$ in general) is the saturation value,

$$b = 1 - \sqrt{1 - b_0} \tag{55}$$

$$b_0 = \frac{r - r_0}{r_{sat} - r_0} \tag{56}$$

and $b = 0$ otherwise. Condensational growth of cloud droplets occurs if $r > r_0$. Oppositely, an existing cloud is diluted by evaporation if $r < r_0$. The condensation threshold r_0 is specified as a function of height (or pressure), fitted to the results obtained by Xu and Krueger (1991) from experiments with a high-resolution cumulus ensemble model,

$$r_0(p) = r_{0,top} + (r_{0,surf} - r_{0,top})e^{[1 - (p_s/p)^n]} \tag{57}$$

where p is pressure, p_s is surface pressure, $r_{0,top} = 0.6$ and $r_{0,surf} = 0.99$ are the upper and lower values of r_0, and $n = 4$ is a fitting parameter. The function (57) is used for all cloud types except for marine stratus under a low-level inversion. If such an inversion is detected below about 700 hPa, r_0 is reduced to 0.7 below the inversion and $r_{sat} = 0.9$ so that, according to (55) and (56), $b = 1$ is reached already before the whole layer is saturated. This ad hoc parameter setting allows formation of thin stratus clouds under a subsidence inversion which otherwise would not be captured due to the insufficient vertical resolution of the model. The lack of marine stratus clouds is one of the most persistent problems in GCMs.

The mechanism of precipitation formation depends crucially on cloud phase. Therefore, the total cloud water content computed from (54) is empirically split into a liquid phase and ice phase, respectively. Probability functions f_{liq} and f_{ice} were derived by Rockel et al. (1991) through an empirical fit to aircraft measurements of cloud water and ambient temperature ($T < T_0 = 273.16$ K) compiled by Matveev (1984),

$$f_{liq} = a + (1 - a)e^{-b(T - T_0)^2} \tag{58}$$

$$f_{liq} + f_{ice} = 1 \tag{59}$$

with $a = 0.0059$ and $b = 0.003102$, while $f_{liq} = 1$ for $T \geq T_0$.

Accordingly, the liquid and ice fractions of the total in-cloud water content $q_c = q_w/b$ are given by

$$q_c = q_{cl} + q_{ci} \tag{60}$$

where $q_{cl} = f_{liq} \cdot q_c$ represents the in-cloud liquid water content and $q_{ci} = f_{ice} \cdot q_c$ the in-cloud ice water content. The autoconversion of cloud droplets to precipitating rain drops is parameterized in a convenient exponential form (Sundqvist, 1978). In addition, the collision of cloud droplets with larger rain drops is taken into account (Smith, 1990), so that the total coalescence rate is given by

$$P_{cl} = q_{cl} \cdot \left(C_0 \left[1 - e^{-(q_{cl}/q_{cr})^2} \right] + C_1 \langle P \rangle \right) \tag{61}$$

where $\langle P \rangle$ is the rain flux density at the top of the respective cloud layer, and C_0, C_1 and q_{cr} are microphysical constants which determine the efficiency of rain formation and, thus, the cloud lifetime (in ECHAM-4/T42: $C_0 = 2\mathrm{x}10^{-4}\ \mathrm{s}^{-1}$, $C_1 = 1\ \mathrm{m^2/kg}$ and $q_{cr} = 0.5\mathrm{x}10^{-3}$ and $0.3\mathrm{x}10^{-4}$ for continental and maritime clouds, respectively).

Ice crystals settle at a rate which depends on their form and size. Both parameters are not available in the model. However, according to an observational study by Heymsfield (1977), the terminal velocity v_t of the crystals can be parameterized in terms of the ice water content,

$$v_t = \alpha(\rho_a \cdot q_{ci})^\beta \tag{62}$$

where ρ_a is air density and α, β are empirical constants (in ECHAM4/T42: $\alpha = 1.97$ and $\beta = 0.16$). The loss of ice crystals due to sedimentation is given by the divergence of the ice water flux density

$$P_{ci} = g\frac{\partial}{\partial p}(v_t \rho_a q_{ci}) \tag{63}$$

where p is pressure and g the acceleration of gravity. With (61) and (63) the total precipitation rate entering (54) is finally obtained as

$$P_c = P_{cl} + P_{ci} \tag{64}$$

As in ECHAM-3, precipitation falling into the cloud-free part of a grid box is exposed to evaporation which is parameterized in terms of the saturation deficit, and melting of snowfall is assumed whenever the temperature of the respective layer exceeds 2°C (Roeckner et al., 1992).

3.7. RADIATION

The radiation scheme used in the previous ECHAM models has been replaced by the ECMWF scheme (ECMWF Res. Dep., 1991), with a few modifications such as the inclusion of additional greenhouse gases, revised parametrizations for the water vapour continuum and for the cloud optical properties and, as an option, optical properties for 11 types of aerosols according to the GADS dataset (Koepke et al., 1996).

3.7.1 Longwave radiation

The radiative transfer scheme developed for the ECMWF model (Morcrette, 1984; Morcrette and Fouquart, 1985; Morcrette et al., 1986) is derived from the upward (u) and downward (d)

components of the monochromatic flux F_ν at wavenumber ν, assuming a non-scattering atmosphere in local thermodynamic equilibrium,

$$F_\nu^u = [B_\nu(T_s) - B_\nu(T_a)]t_\nu(p_s, p; r) + B_\nu(T_p) - \int_{p_s}^{p} t_\nu(p', p; r)dB_\nu \qquad (65)$$

$$F_\nu^d = [B_\nu(T_{top}) - B_\nu(T_\infty)]t_\nu(p, 0; r) + B_\nu(T_p) - \int_{p}^{0} t_\nu(p, p'; r)dB_\nu \qquad (66)$$

where B_ν is the Planck function (including the π factor), T is temperature (where the subscripts s, a, p and top refer to the surface, surface air, pressure level and top of the model, respectively), $t_\nu(p, p'; r)$ is the monochromatic transmission function of the flux through a slab between pressure levels p and p', and is evaluated in a direction θ to the vertical such that $r = \sec\theta$ is the diffusivity factor (Elsasser, 1942). The integrals in (65) and (66) are evaluated numerically with special attention to the impact of local temperature and pressure (Morcrette and Fouquart, 1985).

The integration over wavenumber ν is performed using a non-isothermal band emissivity method. The longwave spectrum is divided into six spectral regions corresponding to the centres of the absorption bands (Table 1).

Different from the ECMWF code, the effect of minor trace gases is considered in addition, such as the absorption due to CH_4 (7.7 μm), N_2O (7.8, 10.7 and 17 μm), 16 CFC's, HCFC's, and HFC's (IPCC, 1990), as well as the 14.6 μm band of O_3 (v. Dorland, pers. comm.). Another modification concerns the H_2O continuum. In the ECMWF code, following Roberts (1976), the (p-e)-continuum absorption is a constant fraction ($\gamma = 0.002$) of the e-type absorption strength within the spectral region 350-1250 cm^{-1} (bands 2-5). In ECHAM-4, a wavenumber dependence of γ has been introduced (Giorgetta and Wild, 1995), as suggested by Ma and Tipping (1992) on the basis of quantum mechanical calculations, with $\gamma_n = (0.059, 0.017, 0.0025, 0.0018, 0.0025)$ representing the spectral bands $b_n = (350\text{-}500, 500\text{-}800, 800\text{-}970, 970\text{-}1110, 1110\text{-}1250$ cm$^{-1})$, respectively.

Table 1: Longwave spectral bands

Band No.	Spectral region (cm^{-1})	Corresponding absorption bands
1	(0 - 350) and (1450 - 1880)	rotation and vibration-rotation of H_2O
2	(500 - 800)	15 μm CO_2
3	(800 - 970) and (1110 - 1250)	atmospheric window
4	(970 - 1110)	9.6 μm O_3
5	(350 - 500)	25 μm "window"
6	(1250 - 1450) and (1880 - 2820)	wings of H_2O vibration-rotation

Over the spectral regions indicated in Table 1, band averaged fluxes are evaluated with the help of band transmissivities pre-calculated from the narrow-band model of Morcrette and Fouquart (1985). The integration over wavenumber accounts for the temperature dependency involved in atmospheric flux calculation, namely its effect on emission as well as on transmission through the temperature dependence of the intensities and half-widths of the lines absorbing in the respective spectral region. The band transmissivities are non-isothermal, accounting for the temperature dependence that arises from the wavenumber integration of the product of the monochromatic absorption and the Planck function. For computational efficiency, the transmissivities have been developed into Padé approximants

$$t(\overline{up}, T_u) = \sum_{i=0}^{2} C_i \sqrt{u_{eff}}^i / \sum_{j=0}^{2} D_i \sqrt{u_{eff}}^j \qquad (67)$$

where $u_{eff} = r\overline{up} \cdot f(T_u, \overline{up})$ is an effective absorber amount of an absorber which includes the diffusivity factor r, the weighting of the absorber amount u with pressure p and the temperature dependence of the absorption coefficients, with

$$f(T_u, \overline{up}) = \exp[a(\overline{up})(T_u - 250) + b(\overline{up})(T_u - 250)^2] \qquad (68)$$

The temperature dependence due to Wien's law is incorporated although there is no explicit variation of the coefficients C_i and D_j with temperature. These coefficients have been computed for temperatures between 187.5 and 312.5 K with a 12.5 K step, and transmissivities corresponding to the reference temperature closest to the pressure weighted temperature T_u are actually used in the scheme.

The treatment of clouds follows the method of Washington and Williamson (1977). The fluxes for clear and overcast skies are calculated separately and combined subsequently in a manner proportional to cloud amount. For example, assume that a cloud is present in the n-the layer of the model atmosphere, the upward fluxes above the cloud (for $k \geq n$) and downward fluxes below the cloud (for $k < n$) can be expressed, analogous to (65) and (66), by

$$F_n^u(k) = [F_c^u - B_s]t(p_k, p_{n+1}; r) + B(k) + \int_{p_{n-1}}^{p_k} t(p_k, p'; r) dB \qquad (69)$$

$$F_n^d(k) = [F_c^d - B_n]t(p_k, p_n; r) + B(k) + \int_{p_k}^{p_n} t(p', p_k; r) dB \qquad (70)$$

where B is the total Planck function (integrated over the whole longwave spectrum), and F_c^u, F_c^d are the fluxes at the upper and lower boundary of the cloud. Terms under the integrals correspond to exchange of energy between layers in the clear-sky atmosphere and have already been estimated in the first step of the calculation. This step is repeated for all cloud layers. The fluxes for the actual atmosphere (with semi-transparent, fractional and/or multi-layered clouds) are derived from a linear combination of the fluxes calculated at the previous step with some cloud overlap assumption in the case of clouds present in several layers. For contiguous cloud layers,

maximum overlap is assumed and random overlap otherwise. In the case of semi-transparent clouds, the fractional cloudiness entering the calculations is an effective cloud cover equal to the product of the horizontal cloud cover and emissivity which is parameterized in terms of the cloud water path (see Section 3.7.4).

3.7.2 Shortwave radiation

The radiative transfer equation for diffuse radiation L_ν at wavenumber ν, in a direction given by the azimuth angle ϕ and $\mu = cos\ \vartheta$ where ϑ is the zenith angle, may be written in the form

$$\mu\frac{d}{d\delta}[L_\nu(\delta, \mu, \phi)] = L_\nu(\delta, \mu, \phi) - \frac{\omega_\nu(\delta)}{4}\{P_1 - P_2\}$$

$$\text{with}\quad P_1 = P_\nu(\delta, \mu, \phi; \mu_0, \phi_0)F_\nu^{\ 0}e^{-\delta/\mu_0}$$

$$\text{and}\quad P_2 = \int_0^{2\pi}\int_{-1}^{1} P_\nu(\delta, \mu, \phi; \mu', \phi')L_\nu(\delta, \mu', \phi')d\mu'd\phi' \tag{71}$$

$F_\nu^{\ 0}$ is the solar irradiance in the direction $\mu_0 = cos\ \vartheta_0$, δ the optical depth, ω_ν the single scattering albedo and $P_\nu(\delta, \mu, \phi, \mu', \phi')$ is the scattering phase function which defines the probability that radiation coming from the direction (μ', ϕ') is scattered in the direction (μ, ϕ). The shortwave part of the ECMWF code, developed by Fouquart and Bonnel (1980) solves (71) by integrating the fluxes between 0.2 and 4 μm. Upward and downward fluxes are obtained from the reflectances and transmittances of the layers, and the photon path distribution method is applied to separate the parameterization of the scattering processes from that of molecular absorption.

Solar radiation is attenuated by absorbing gases, mainly water vapour, carbon dioxide, oxygen and ozone, and scattered by molecules (Rayleigh scattering), aerosols, and cloud particles. Since scattering and molecular absorption occur simultaneously, the exact absorber amount along the photon path length is unknown, and band models of the transmission function cannot be used directly as in longwave radiative transfer. The approach of the photon path distribution method is to calculate the probability $P(u)du$ that a photon contributing to the flux F_c in the conservative case (i.e., no absorption: $\omega_c = 1$ and absorption coefficient $k_\nu = 0$) has encountered an absorber amount between u and $u + du$. With this distribution, the radiative flux at wavenumber ν is related to F_c by

$$F_\nu = F_c\int_0^\infty P(u)e^{-(k_\nu u)}du \tag{72}$$

and the flux averaged over the interval $\Delta\nu$ can be calculated with the help of any band model of the transmission function $t_{\Delta\nu}$

$$F = \frac{1}{\Delta_\nu}\int_{\Delta_\nu}F_\nu d\nu = F_c\int_0^\infty P(u)t_{\Delta_\nu}(u)d\nu \tag{73}$$

In order to find the distribution function, the scattering problem is solved first for a first-guess absorbing atmosphere, and an inverse Laplacian transform is then performed to get $P(u)$. The main advantage of the method is that the actual distribution needs not to be calculated explicitly since the spectrally integrated fluxes are

$$F = F_c t_{\Delta_v} \langle u \rangle \quad \text{in the limiting case of weak absorption} \tag{74}$$

$$F = F_c t_{\Delta_v} \langle \sqrt{u} \rangle \quad \text{in the limiting case of strong absorption} \tag{75}$$

where $\langle u \rangle = \int_0^\infty P(u) u \, du$ and $\langle \sqrt{u} \rangle = \int_0^\infty P(u) \sqrt{u} \, du$.

The atmospheric absorption in the water vapour bands is generally strong, and the scheme determines an effective absorber amount u_e between $\langle u \rangle$ and $\langle \sqrt{u} \rangle$ derived from

$$u_e = \ln(F_{k_e}/F_c)/k_e \tag{76}$$

where an absorption coefficient k_e is chosen to approximate the spectrally averaged transmission in the clear-sky atmosphere,

$$k_e = \frac{1}{u_{tot}/\mu_0} \ln[t_{\Delta v}(u_{tot}/\mu_0)] \tag{77}$$

where u_{tot} is the total absorber amount in a vertical column and $\mu_0 = \cos\varphi_0$. Once the effective absorber amounts of water vapour and uniformly mixed gases are found, the transmission functions are computed using Padé approximants

$$t_{\Delta v}(u) = \left(\sum_{i=0}^N a_i u^{i-1} \right) \bigg/ \left(\sum_{j=0}^N b_j u^{j-1} \right) \tag{78}$$

Absorption by ozone is also taken into account, but since ozone is located at low pressure levels for which molecular scattering is small and Mie scattering is negligible, interactions between scattering processes and ozone absorption are neglected. Transmission through ozone is computed using (78), where u_{O_3}, the amount of ozone, is

$$u_{O_3}^d(p) = M \int_p^0 du_{O_3}(p) \quad \text{for the downward transmission of the direct solar beam} \tag{79}$$

$$u_{O_3}^u(p) = r \int_{p_s}^p du_{O_3}p + u_{O_3}^u p_s \quad \text{for the upward transmission of the diffuse radiation} \tag{80}$$

$r = 1.66$ is the diffusivity factor and M is the magnification factor (Rodgers, 1967) used instead of μ_0 to account for the sphericity of the atmosphere at very small solar elevations,

$$M = 35/(\sqrt{1224\mu_0^2 + 1}) \tag{81}$$

For the spectral integration, the scheme considers two intervals, one for the visible (0.2 - 0.68 μm) and one for the near-infrared (0.68 - 4.0 μm) part of the solar spectrum. The cutoff at 0.68 μm makes the scheme computationally efficient, inasmuch as interactions between gaseous absorption and scattering processes are accounted for only in the near-infrared interval.

Assuming an atmosphere divided into N homogeneous layers, the upward and downward fluxes at a layer interface j are given by

$$F^d(j) = F_0 \prod_{k=j}^{N} T_b(k) \tag{82}$$

$$F^u(j) = F^d(j) R_t(j-1) \tag{83}$$

where $R_t(j)$ and $T_b(j)$ are the reflectance at the top and the transmittance at the bottom of the j-th layer, respectively. R_t and T_b account for the presence of clouds in the layer according to

$$R_t = CR_c + (1-C)R_{clr} \tag{84}$$

$$T_b = CT_c + (1-C)T_{clr} \tag{85}$$

where C is fractional cloud cover, and the subcripts c and clr refer to the cloudy and cloud-free portions of the layer, respectively. The reflectance at the top of the cloudy fraction (R_{tc}) and transmittance at the bottom (T_{bc}) are calculated with the Delta-Eddington Approximation. For given optical thicknesses of the cloud (δ_c), the aerosol (δ_a), molecular absorption (δ_g), and respective asymmetry factors (g_c and g_a), R_{tc} and T_{bc} are calculated as functions of the total optical thickness of the layer,

$$\delta = \delta_c + \delta_a + \delta_g \tag{86}$$

of the total single scattering albedo,

$$\omega = (\delta_c + \delta_a)/(\delta_c + \delta_a + \delta_g) \tag{87}$$

of the total asymmetry factor,

$$g = g_c \delta_c / (\delta_c + \delta_a) + g_a \delta_a / (\delta_c + \delta_a) \tag{88}$$

of the reflectance of the underlying medium (surface or cloud layers below the j-th interface, and of an effective solar zenith angle $\mu_e(j)$ accounting for the decrease of the direct solar beam and the corresponding increase of the diffuse part of the downward radiation by the upper scattering layers,

$$\mu_e(j) = [(1 - C^{al}(j))/\mu + rC^{al}j]^{-1} \tag{89}$$

24

$$\text{with} \quad C^{al}(j) = 1 - \prod_{i=j+1}^{N} (1 - C(i)E(i)) \tag{90}$$

$$\text{and} \quad E(i) = 1 - \exp-\left[\frac{(1 - \omega_c(i)g_c(i)^2)\delta_c(i)}{\mu} \right] \tag{91}$$

$\delta_c(i)$, $\omega_c(i)$ and $g_c(i)$ are the optical thickness, single scattering albedo and asymmetry factor, respectively, of the cloud in the i-th layer, and r is the diffusivity factor. The scheme follows the Delta-Eddington approximation (Joseph et al., 1976) which assumes that the radiance L entering (71) can be written in the form

$$L(\delta, \mu) = L_0(\delta) + \mu L_1(\delta) \tag{92}$$

In that case, when the phase function is expanded as a series of associated Legendre functions, all terms of order greater than one vanish when (71) is integrated over μ and ϕ.

In the clear-sky fractions of the layers, the scheme accounts for scattering and absorption by molecules and aerosols. As the optical thickness for both Rayleigh and aerosol scattering is small, the reflectance at the top of the j-th layer, $R_{clr}(j\text{-}1)$, and the transmittance at the bottom, $T_{clr}(j)$, can be calculated using a first and a second order expansion, respectively, of the analytic solutions of the two-stream equations similar to that of Coakley and Chylek (1975).

To deal properly with multiple reflections between the surface and cloud layers, and clear-sky layers as well, it should be necessary to separate the contribution of each individual reflecting surface to the layer reflectances and transmittances inasmuch as each such surface gives rise to a particular distribution of absorber amount. Fouquart and Bonnel (1980) have shown that a very good approximation to this problem is obtained by calculating the reflectance and transmittance of each layer by assuming sucessively a non-reflecting underlying medium (R_ = 0) and then a reflecting one (R_ ≠ 0). While the first step provides the contribution to reflectance and transmittance of those photons interacting only with the layer in consideration, the second one gives the contribution of the photons with interactions outside of the layer itself.

3.7.3 Shortwave cloud optical properties

For the shortwave (solar) part of the spectrum, the single scattering properties are determined on the basis of high-resolution Mie calculations using idealized size distributions for both cloud droplets and spherical ice crystals (Rockel et al., 1991). The results are averaged over the relatively wide ranges of the GCM with appropriate weighting by the Planck function. This procedure is done for different effective radii, and suitable fits are finally employed which allow to express the respective single scattering parameter (Y) in terms of the effective radius (r_e in µm):

Mass extinction coefficient . . . . . . $Y = a_0 r_e^{a_1}$ (93)

Single scattering albedo . . . . $Y = \sum_{n=0}^{3} b_n (\log r_e)^n$ (94)

Asymmetry factor. . . . . $Y = \sum_{n=0}^{4} c_n (\log r_e)^n$ (95)

The coefficients a_n, b_n, and c_n are given in Table 2 for both spectral intervals (visible and near-infrared, respectively) and for both phases as well. Consistent with (93), the optical depth of a cloud layer with in-cloud liquid (ice) water path LWP (IWP) is defined (for the respective spectral region and cloud phase: see coefficients in Table 2) according to

$$\delta_l = a_0 r_{el}^{a_1} \cdot LWP$$ (96)

$$\delta_i = a_0 r_{ei}^{a_1} \cdot IWP$$ (97)

Table 2: Coefficients used in the polynomial fits to Mie calculations of shortwave single scattering proporties as functions of effective radius (cf., eqs. (93) - (95)).

Coeff.	Liquid droplets		Ice spheres	
	0.2 - 0.68 μm	0.68 - 4.0 μm	0.2 - 0.68 μm	0.68 - 4.0 μm
a_0	1.8706058417	1.9655460426	1.9056067246	2.1666771102
a_1	-1.0756364457	-1.0778999732	-1.0318784654	-1.0634702711
b_0	-	0.9854369057	-	0.98475089485
b_1	-	0.013584242533	-	0.0053152066002
b_2	-	-0.024856960461	-	-0.0061150583857
b_3	-	0.0055918314369	-	-0.0032775655896
c_0	0.78756640717	0.79208639802	0.7700034985	0.83631171237
c_1	0.10660598895	-0.044930076174	0.19598466851	-0.19965998649
c_2	-0.031012468401	0.18980672305	-0.11836420885	0.46130320487
c_3	0.	-0.082590933352	0.025209205131	-0.29719270332
c_4	0.	0.	0.	0.062554483594

Since it is well known that Mie theory tends to overestimate the asymmetry factor for ice clouds (e.g., Stephens et al., 1990), a correction factor of 0.91 has been applied which adjusts g_i to a more realistic value of ~0.80 (Francis et al., 1994) for a wide range of effective radii.

In the mixed phase, the shortwave cloud optical depth δ_m, single scattering albedo ω_m, and asymmetry factor g_m are defined as

$$\delta_m = \delta_l + \delta_i \tag{98}$$

$$\omega_m = \frac{\omega_l \delta_l + \omega_i \delta_i}{\delta_l + \delta_i} \tag{99}$$

$$g_m = \frac{\omega_l \delta_l g_l + \omega_i \delta_i g_i}{\omega_l \delta_l + \omega_i \delta_i} \tag{100}$$

where the subscripts m,l,i refer to the mixed, liquid and ice phase, respectively.

3.7.4 Longwave cloud optical properties

In the longwave (terrestrial) part of the spectrum, droplet absorption is computed using an emissivity formulation. Analogous to the shortwave region (Section 3.7.3), the mass absorption coefficient for liquid or ice clouds, $K_{l,i}$ (in m^2/g), has been parameterized as a function of the effective radius r_e (in µm) according to

$$K_{l,i} = d_0 + d_1 e^{-(d_2 \cdot r_e)} \tag{101}$$

with coefficients d_n for both phases according to Table 3, including the diffusivity factor (1.66) in d_0 and d_1. For cirrus clouds, similar to (101), an inverse dependence of K_i on the ice crystal effective radius has been postulated by Stephens et al. (1990) and also inferred from measurements during the International Cirrus Experiment ICE'89 by Francis et al. (1994).

Table 3: Coefficients used in the polynomial fit to Mie calculations of longwave absorption coefficient as function of effective radius (cf., eq. (101)).

Coefficient	Liquid droplets	Ice spheres
d_0	0.025520637	0.020219423
d_1	0.2854650784	0.2058619832
d_2	-0.088968393014	-0.067631070625

The transmissivity $T_{l,i}$ of a liquid cloud layer and that of an ice cloud layer with respective in-cloud LWP and IWP, is given by

$$T_l = e^{-K_l \cdot LWP} \tag{102}$$

$$T_i = e^{-K_i \cdot IWP} \tag{103}$$

The transmissivity of a mixed phase cloud layer is defined as

$$T_m = T_l T_i \tag{104}$$

so that the total cloud emissivity of a layer with fractional cloud cover b, containing liquid and/or ice clouds can finally be written as

$$\varepsilon = b(1 - T_m) \tag{105}$$

3.7.5 Effective radii of cloud droplets and ice crystals

While, according to (96), (97) and (102), (103), the cloud water path determines the shortwave optical depth as well as the longwave transmissivity, respectively, there is ample evidence that the effective radii of both cloud droplets and ice crystals depend on the cloud water content as well (Stephens and Platt, 1987; Minnis et al., 1992; Francis et al., 1994).

For warm clouds, the in-cloud liquid water content q_{cl} (see (58) to (60)) can also be expressed in terms of the mean volume radius r_v and the cloud droplet number concentration N,

$$q_{cl} = \frac{4}{3}\pi\rho_w N r_v^3 \tag{106}$$

where ρ_w is the densitiy of liquid water. According to Johnson (1993), r_v can be related to the droplet effective radius r_{el} by

$$r_v^3 = k r_{el}^3 \tag{107}$$

so that the effective radius is a function of the model calculated in-cloud liquid water content q_{cl}, the droplet number concentration N, and a parameter k which is related to the shape of the size distribution,

$$r_{el} = \left\{ \frac{3 q_{cl}}{4\pi\rho_w k N} \right\}^{1/3} \tag{108}$$

From data sampled in various field experiments (FIRE, FATE, ASTEX), Johnson (1993) found a mean value for the shape parameter of $k = 0.67$ in continental clouds and $k = 0.80$ in maritime clouds. The largest uncertainty in the above parameterization is due to N which may vary by orders of magnitude in time and space. Since N cannot be predicted within the standard version of our model, we have specified values which are typical for low-level continental clouds ($N = 220$ cm^{-3}) and low-level maritime clouds ($N = 100$ cm^{-3}), respectively. Above the atmospheric boundary layer, N is assumed to decrease exponentially with height, approaching a value of 50 cm^{-3} in the upper troposphere.

The parametrization of the ice crystal effective radius r_{ei} is adopted from the Canadian Climate Center model (McFarlane et al., 1992),

$$r_{ei} = \alpha\chi^\beta \tag{109}$$

with $\alpha = 5640$ and $\beta = 0.786$. The mean crystal length χ is an empirical function of the model calculated in-cloud ice water content q_{ci} (Heymsfield,1977)

$$\chi = \gamma \sum_{n=0}^{3} \delta_n (\log q_{ci})^n \tag{110}$$

with $\gamma = 0.001$, $\delta_0 = 0.698$, $\delta_1 = 0.366$, $\delta_2 = 0.122$ and $\delta_3 = 0.0136$.

For both droplets and ice crystals, upper and lower limits of the effective radii are imposed according to $4 \le r_{el} \le 24\mu m$ and $12 \le r_{ei} \le 80\mu m$, respectively.

3.7.6 Surface albedo

The background albedo used in ECHAM-3 has been replaced by a new dataset compiled by Claussen et al. (1994) , see also Appendix A. The albedo of snow and ice surfaces is a function of temperature and, over land, fractional forest area as described in Roeckner et al. (1992), while an albedo of 0.07 is assigned to all water surfaces.

3.7.7 Solar zenith angle

The solar zenith angle is calculated according to Paltridge and Platt (1976). Due to the curvature of the Earth, the zenith angle is not constant along the path of a sun ray, and a correction is applied to the cosine of the zenith angle, μ_0^a, in order to obtain an average μ_0 for the atmosphere,

$$\mu_0 = \frac{H/a}{\sqrt{(\mu_0^a)^2 + \frac{H}{a}\left(2 + \frac{H}{a}\right)} - \mu_0^a} \tag{111}$$

where a is the Earth's radius and H the atmospheric equivalent height. H/a is fixed at 0.001277.

4. MODEL CLIMATOLOGY

4.1. EXPERIMENTS AND OBSERVATIONAL DATA

Two extended AMIP integrations (Atmospheric Model Intercomparison Project, Gates, 1992) have been performed with ECHAM-4 using observed monthly mean sea surface temperatures (SSTs) and sea ice limits (Jan. 1979 - May 1994). These experiments differ only with respect to the initial conditions which are specified for 1 July and 1 October 1978, respectively. The model history is written every 12 hours. The results presented below are averages over both experiments, except for the global budgets which refer to the ten-year AMIP period (1979-1988) of one of these experiments.

Most of the observed climatologies used for model validation are based on ECMWF operational analyses. These climatologies have been computed for about the same period (1980-1992) for which the boundary values of SST and sea ice are available for driving the model. For precipitation, the long-term climatology compiled by Legates and Willmott (1990) is used as a reference.

The observed global means of top-of-atmosphere (TOA) radiation fluxes represent two years of 'Earth Radiation Budget Experiment' (ERBE) scanner observations (Feb. 1985 - Jan. 1987; Hartmann, 1993). For surface radiation, the estimates are based on the 'Global Energy Budget Archive' (GEBA; Ohmura and Gilgen, 1991). Global means of incoming solar radiation have been calculated by Gilgen et al. (1996) from an updated dataset (GEBA 1995) over land and empirical formulae over sea. In addition, the total land-surface radiation budget has been estimated by Garrat and Prata (1996) from GEBA data and budget requirements. The uncertainty in the global ERBE scanner estimates is about ± 5 W/m^2 (Barkstrom et al., 1990), but definitely larger for the surface fluxes (Garrat and Prata, 1996). The uncertainties in the global means are caused by instrumental errors and poor data coverage, especially over the oceans (GEBA), while the influence of interannual variability can be disregarded.

4.2. GLOBAL MEANS

A comparison of simulated and observed TOA radiation fluxes is shown in Table 4, for both 'all sky' (i.e., including the effects of clouds) and clear sky conditions. In comparing the simulated clear sky fluxes with those from ERBE, one has to keep in mind that different methods are used to compute these fluxes. While the ERBE estimates are based on time averaging over clear sky regions, the model calculates clear sky fluxes, at every radiation time step, in a second (diagnostic) loop of the radiative transfer code with cloud cover set to zero but all other parameters unchanged. As discussed by Zhang et al. (1994), the difference obtained with both methods can be large locally (more than 10 W/m^2 in persistently cloudy regions) but should be irrelevant for the global mean.

As apparent from Table 4, the model estimates (ECHAM-3 is shown for comparison as well) are fairly similar to each other, and both of them are within the range of observational uncertainty. However, one has to note that the global mean shortwave and longwave outgoing fluxes (all sky) have been 'tuned' to ERBE data by an appropriate choice of the cloud microphysical parameters (see Section 3.6) which determine cloud lifetime, cloud water content and, hence, cloud optical properties (see Sections 3.7.3 to 3.7.5). Since the simulated clear sky fluxes are very close to the ERBE estimates, the tuning process outlined above does not involve a compensation for clear sky errors but allows for simulating a realistic cloud radiative forcing as well (see Table 8). According to Table 4, the global imbalance (i.e., the total radiation) is smallest in ECHAM-4 ($+1.6$ W/m^2) and largest in ERBE ($+6$ W/m^2). The latter value is consistent with the error bars estimated for the individual components (± 5 W/m^2). For a more detailed comparison, see Chen and Roeckner (1996a).

From GEBA data and budget requirements, Garratt and Prata (1996) compiled a complete land-surface radiation budget which is shown in Table 5 as an observational reference for the model simulation. Different from the TOA budget, the surface fluxes simulated by the two models differ considerably. For example, compared to ECHAM-3, the downwelling shortwave is reduced in ECHAM-4 by about 17 W/m^2, while the downwelling longwave is larger by about 6 W/m^2. These differences are caused mainly by changes in clear sky fluxes where ECHAM-4 shows a reduction of downwelling solar radiation by 13 W/m^2 and an increase in downwelling longwave by 10 W/m^2. In general, ECHAM-4 is more realistic and largely within the range of observations (see the discussion in Wild et al., 1996).

Similar conclusions as for the land surface can be drawn for the globe as a whole (Table 6). For the downwelling shortwave radiation, there is a good agreement between ECHAM-4 and GEBA (Gilgen et al., 1996). This applies for the upwelling shortwave and net shortwave radiation as well. However, one has to keep in mind that these are not independent estimates but calculated from the downwelling shortwave by assuming a global mean surface albedo of 13% which is similar to that used in the simulation.

The global atmospheric radiation budget in Table 7 is calculated as the difference between TOA radiation (Table 4) and surface radiation (Table 6). Compared to ECHAM-3, the net shortwave radiation (i.e., that part of the solar radiation which is absorbed within the atmosphere) has increased in ECHAM-4 by about 19 W/m^2. Nearly 50% of that increase (9 W/m^2) is due to enhanced water vapour absorption (clear sky), while the rest is due to enhanced cloud absorption (see Table 8). Oppositely, the enhanced longwave cooling of the atmosphere in ECHAM-4 (and, consequently, enhanced downwelling longwave radiation at the surface, see Table 6) is nearly identical to the change in the respective clear sky component, i.e., clouds do not contribute to this change. The all- sky atmospheric absorption of solar radiation simulated with ECHAM-4 is consistent with that derived from ERBE and GEBA data.

In Table 8 the cloud radiative forcing is shown for the whole Earth-atmosphere system (TOA), at the surface and within the atmosphere. At TOA, the good agreement between both models and

ERBE is the result of a tuning procedure (see earlier). In ECHAM-4, the cloud absorption of solar radiation is more than twice as large as in ECHAM-3, partly due to the larger cloud amount in ECHAM-4 (~60% compared to ~50% in ECHAM-3), and partly due to the parameterization of cloud optical properties (see Section 3.7.3 to 3.7.5), resulting in a smaller single scattering albedo compared to ECHAM-3. For a more detailed discussion, see Wild et al. (1996). Consistent with the enhanced cloud absorption in ECHAM-4 is the enhanced cloud radiative cooling at the surface. In the longwave components, there is hardly any difference between both models.

The simulated components of the annual mean surface heat budget are shown in Table 9, separately for land, ocean (i.e., open water and sea ice) and for the whole globe. The most apparent differences between the models appear in both components of the radiation budget, as discussed earlier, while the sensible and latent heat fluxes are more similar. Strikingly different are the total heat fluxes over sea which almost vanish in ECHAM-4 but are close to 9 W/m^2 in ECHAM-3. While such an imbalance is not surprising in a model with prescribed SSTs, the large imbalances over land, with 12.9 W/m^2 in ECHAM-3 and 7.6 W/m^2 in ECHAM-4, are more puzzling and are related to inconsistencies between the diagnosis of the individual surface fluxes and the numerical scheme for calculating the land surface temperature. In this scheme, for numerical reasons, the total heat flux is developed into a Taylor series around the actual surface temperature and truncated after the linear term. The heat lost by this linearization has been diagnosed during the experiments and found to be identical to the long-term imbalance. In essence, the surface temperature is calculated from a heat flux which is systematically smaller than that diagnosed from the individual parameterizations. Although it is not possible to attribute the heat flux lost by the linearization to the individual flux components, the solar radiation is probably the dominant term (large and positive).

The annual hydrological cycle is shown in Table 10 for both models and for two estimates based on observations and budget requirements. In the global mean, the water fluxes are slightly larger in ECHAM-4, compared to ECHAM-3, but the imbalance is larger by a factor of 10. According to a water budget analysis of the individual processes, a minor part of this imbalance in ECHAM-4 is due to cumulus convection (similar to ECHAM-3), but the largest part is caused by the semi-Lagrangian advection scheme. In general, the simulated water fluxes are very similar in both models. The most apparent exception (over sea) is the smaller difference Evap - Precip in ECHAM-4, i.e., there is less water vapour transported from ocean to land so that the continental runoff is smaller as well. On the other hand, more water is recycled over land. In the model simulations, the mass budget of glaciers (Greenland and Antarctica) is not closed. While the accumulation of snow is simulated and diagnosed in these areas (see Table 10, last row), ablation and calving have not been taken into account. The observed estimate of annual snowfall on glaciers (Bromwich, 1990) is somewhere in the middle between the model estimates. For consistency with the model simulation, the runoff estimates of Baumgartner and Reichel (1975) and Chahine (1992), which include glacier ablation and calving, have been modified in Table 10 by subtracting the snow accumulation calculated by Bromwich (1990). Taking into account the large uncertainties in the observations, particularly over the oceans, the simulated water cycle in

both models appears to be largely consistent with the observed one.

At least from a global perspective, most of the basic climate variables are similar in both models (Table 11). Surface air temperature is nearly identical and the vertical integrals of water vapour and cloud water are just slightly smaller in ECHAM-4. More significant is the difference in cloud cover which, globally, is about 8% larger in ECHAM-4, in better accordance with ground based estimates (Hahn et al., 1994) as well as with satellite data (ISCCP). For a more detailed comparison, see Chen and Roeckner (1996b) for cloud parameters and Chen et al. (1996) for water vapour.

A compact view on the land surface climate is shown in Table 12. The land surface climate of the models is evaluated here in terms of biome distributions calculated with the model of Prentice et al. (1992) which has been forced with model output, i.e., mean annual cycles of surface air temperature, precipitation and cloudiness (Claussen and Esch, 1994). An estimate ('obs') based on climate observations is shown for comparison. For most of the biomes (12 out of 16), the ECHAM-4 simulation is more realistic. The largest improvements are found for warm climates like tropical rain forest (1), savanna (3), warm grass/ shrub (12), but also for cold climates like taiga (8) and tundra (14). Due to insufficient horizontal resolution, both models have problems in simulating the correct biome (cool desert, for example) in areas with complex terrain such as the slopes of the Andes or Himalayas.

4.3.   TIME MEAN CLIMATE

Temperature

Latitude-height cross sections of zonal mean temperature errors (i.e., deviations of the ECHAM-4 simulation from ECMWF climatology) are shown in Fig. 1. The most apparent model error is the cold bias in the polar upper troposphere and lower stratosphere in both hemispheres. This bias is particularly large over the respective summer pole (up to -15K in DJF over Antarctica). These features are typical for modern GCMs and turned out to be insensitive to model formulation (Boer et al., 1992) and horizontal resolution as well (Déqué et al., 1994). For most of the troposphere, the ECHAM-4 errors are fairly small and generally below 2K. Compared to ECHAM-3/T42 (cf., Roeckner et al., 1992, Figs. 6e,f and 7e,f), the error structure is similar in ECHAM-4 but the warm bias in the tropical upper troposphere is substantially reduced in both extent and amplitude. Different from ECHAM-3, the tropical lower stratosphere is too cold throughout the year while it is slightly too warm in ECHAM-3. Another difference concerns the atmospheric boundary layer in the Arctic which is too warm in summer by more than 2K while it is too cold in ECHAM-3 by about the same amount.

The geographical distributions of the temperature error at 850 hPa are shown in Fig. 2. Over the oceans, where observed SSTs have been prescribed in the experiments, the regions with significant errors (i.e., larger than 2K) are smaller than over land. Here, errors of more than 2K

often occur over high mountain ranges (Himalaya, Antarctica etc.) where interpolation to sub-surface pressure levels could be a source of errors. More relevant are the cold biases over the Sahara throughout the year and over Scandinavia in DJF, and the warm biases over the whole Arctic, the western United States and the Amazon region during JJA, respectively. Some of these features like the warming over the United States and the Amazon region have already been found in the ECHAM-3 simulation, even with a larger amplitude, (see Roeckner et al., 1992, Figs. A1 and A2), while the summer warming over the Arctic is a new aspect of the ECHAM-4 simulation. With a few exceptions, the error patterns of 850 hPa temperature are less coherent than those in ECHAM-3 and the errors are generally smaller as well.

Zonal wind

In Fig. 3, a latitude-height cross section of annually and zonally averaged zonal wind derived from the ECHAM-4 simulation is compared with the respective ECMWF climatology ('analysis'). The most apparent errors in the simulation are the overestimation and upward shift of the jet maxima, especially in the Southern Hemisphere (SH), and the westerly wind bias in the tropics. Throughout the troposphere, the Arctic easterlies are slightly more pronounced in the model simulation than in the observed climatology. A relatively good agreement between simulation and observed climatology is found in the lower troposphere.

In DJF (Fig. 4), the error pattern is similar to that of the annual mean. More evident than in the annual mean, particularly in the SH, is a poleward shift of the mid-latitude westerlies.

In JJA (Fig.5), the separation of the subtropical jet from the polar night jet is not well simulated in the SH. While the polar night jet is slightly too weak and shifted equatorward, the subtropical jet is too strong above 200 hPa and shifted upward. Different from DJF, the SH mid-latitude westerlies in the lower troposphere are shifted equatorward. In the Northern Hemisphere (NH), the error pattern is similar to that found in DJF and in the annual mean as well, i.e., there is little evidence of a seasonal variation of the error pattern.

In the ECHAM-3 simulation (see Roeckner et al., 1992, Figs. 8 and 9), the error structure is similar but the amplitudes are larger in general. For example, the jets are even stronger than in ECHAM-4 and the poleward shift of the mid-latitude westerlies is more pronounced, especially in the SH. In the lower troposphere, most evidently near the surface and in the SH, the westerlies are overestimated in ECHAM-3, while there is little evidence of an error in ECHAM-4, apart from the poleward shift mentioned earlier. However, in the tropical upper troposphere, ECHAM-3 is more realistic and there is only a weak westerly bias. Moreover, the Arctic easterlies are less extensive than in ECHAM-4.

One of the most apparent systematic errors in the ECHAM-4 simulation is the westerly wind bias in the upper troposphere and lower stratosphere which is related to the temperature errors (see Fig. 1) via the thermal wind relation. As an example, Fig. 6 shows the latitudinal and seasonal variation of the zonal mean zonal wind at the 200 hPa level. Throughout all seasons and at most latitudes as well, the simulated zonal wind exceeds ECMWF climatology by typically 5 m/s. On

the other hand, the seasonal shift of the maxima is well captured in general, especially in the NH, as well as the broad maxima (or even double jet structures) during the transitional seasons in the SH. In the tropics, the model tends to overestimate the seasonal swing of the westerly wind minimum between the SH in DJF and the NH in JJA.

The geographical distributions of the simulated and observed zonal wind at 200 hPa, together with the error field, are shown in Fig. 7 for the DJF season. The overall structure is well captured by the model and most of the errors arise from differences in the details. For example, the tropical westerly wind bias (see Figs. 3-5) is predominantly caused by larger than observed excursions of the Pacific and Atlantic jets branching out to the tropical eastern Pacific and Atlantic oceans, respectively. The westerly wind bias over Europe is related to the orientation of the jet axis across the Atlantic which is bending eastward into Central Europe in the simulation while it continues to have a SW/NE orientation across the whole North Atlantic in the ECMWF analysis. In the SH, the error pattern is more zonally symmetric and, at least partly, related to a poleward shift of the simulated jet core (see Figs. 4 and 6).

In the JJA season (Fig. 8), the simulated tropical easterlies are weaker than observed and also less extensive, leading to a westerly wind bias nearly everywhere in the tropical belt. The weaker than observed tropical easterly jet together with the weaker than observed westerlies across Central Asia are indicative of an underestimated Asian summer monsoon. In the SH, the position of the jet core centred over southern Australia is well captured by the model but the westerlies are stronger than observed throughout the subtropical belt. Along the coast of Antarctica, the simulated westerlies are weaker than observed (see Fig. 6).

The geographical distributions of the simulated and observed zonal wind at 850 hPa, together with the error field, are shown in Fig. 9 for the DJF season. Similar to the 200 hPa level, the model is able to capture the 850 hPa wind structure with remarkable skill. In the extratropics, the error pattern is similar to that found at the 200 hPa level (i.e. the structure is barotropic). For example, the westerly wind bias over Europe and the poleward shift of the SH westerlies noted earlier are clearly evident in the lower troposphere as well. On the other hand, at lower latitudes, the zonal wind error changes sign with height (i.e. the structure is baroclinic). As in the ECHAM-3 simulation, the Atlantic and Pacific trades are slightly stronger than observed. Also, the near-equatorial westerlies over Africa and the Indian Ocean are stronger than observed while at 200 hPa easterly wind errors prevail at these locations. In general, circulations in the equatorial plane are more pronounced in ECHAM-4 than in the ECMWF climatology.

In the JJA season (Fig. 10), the error pattern is less systematic than in DJF, particularly in the extratropics. Most notably at low latitudes is a westerly wind bias extending from the eastern Pacific across Central America and the Atlantic Ocean into Central Africa. Another band of westerly wind anomalies stretches from the southern Indian Ocean into the tropical West Pacific while easterly wind anomalies prevail further north, indicative of a too weak and southward displaced Asian monsoon flow in the model. As in DJF, the equatorial easterlies in the Central Pacific are overestimated by the model.

Sea level pressure

In Fig. 11 the simulated zonally and seasonally averaged surface pressure (reduced to mean sea level) is compared to the respective ECMWF climatology. The model errors are generally small, i.e., below 5 hPa, except in the Arctic region in DJF and SON. Furthermore, in all seasons, the tropical trough is deeper than observed (by 1-2 hPa), the subtropical highs tend to be higher than observed and shifted poleward, especially during DJF in the NH. These errors are consistent with the zonal wind errors at 850 hPa discussed earlier. Compared to ECHAM-3 (Roeckner et al., 1992, Fig. 12) error pattern and magnitude are basically the same. A significant improvement in ECHAM-4 is the SH meridional pressure gradient in DJF which is much too strong in ECHAM-3. In JJA, on the other hand, the trough around Antarctica is correctly reproduced with ECHAM-3 while it is weaker than observed by about 5 hPa in ECHAM-4.

A comparison of simulated and observed sea level pressure is shown in Fig. 12 for the DJF season. The major pressure systems are well reproduced by the model, such as position and strength (slightly underestimated) of the Aleutian and Icelandic low, respectively. Moreover, as noted earlier, the tropical trough is systematically deeper than observed while the subtropical anticyclones are stronger than observed and shifted poleward in the SH. In the NH, the Azores high is too strong and extended too far eastward over the Mediterranean Sea. The pressure is also too high over the Arctic, especially in the Siberian sector, while there is a small negative pressure anomaly over Central Europe, consistent with the zonal wind error at 850 hPa (see Fig. 9).

In JJA (Fig. 13) the dominant pressure patterns in the NH, i.e., the anticyclones in the North Pacific and North Atlantic, respectively, are well reproduced in position and strength. A pronounced negative pressure anomaly is simulated over the Carribean Sea and over most parts of the United States. As in DJF, the simulated pressure is too low over large parts of the tropics. The only exception, the positive pressure anomaly in the Indian Ocean extending to the southern and eastern parts of Asia, is indicative of an underestimated Asian summer monsoon. In the SH, the trough around Antarctica is somewhat lower than observed (see also Fig. 11).

Geopotential height

The simulated and observed geopotential height at 500 hPa is shown in Fig. 14 for the NH during DJF and JJA, respectively. In DJF, the simulated stationary wave structure at 500 hPa is less pronounced than in the ECMWF climatology, particularly over North America, but also over Europe where the simulated geostrophic flow is more zonal than in the ECMWF climatology. The error pattern with high pressure anomalies over the Arctic, over the Pacific and over the Atlantic is similar to that found for the sea level pressure (see Fig. 12), i.e., the error structure in the lower troposphere is basically barotropic. In JJA, the Arctic low is displaced to northern Greenland in the simulation and significantly higher than observed, due to a warm bias in the lower troposphere (see Figs. 1 and 2).

In the SH (Fig. 15), the error structures in both seasons, DJF and JJA, are very similar to those which have been identified at the surface (see Figs. 12 and 13). In the SH summer (DJF), the error

pattern has a large zonally symmetric component. The simulated geopotential height is too low over Antarctica and too high over the oceans so that the zonal mean geostropic flow around Antarctica is somewhat stronger than in the ECMWF climatology. In the SH winter (JJA), the error pattern has a large zonally asymmetric component, and the error in the zonal mean geostrophic wind is obviously much smaller than in the summer season. The errors in the meridional components of the geostrophic wind are mainly resulting from displacements of the stationary waves. For example, a weak trough is simulated south of Australia (negative anomaly) which is hardly evident in the ECMWF climatology, while the Central Pacific trough is less pronounced in the simulation (positive anomaly) and shifted eastward towards the South American coast (negative anomaly).

Precipitation

In this report, the simulated precipitation is compared with an observational estimate produced by Legates and Willmott (1990, LW90 hereinafter). While this is probably a good estimate over continental areas, and agrees reasonably well with other climatologies such as that obtained within the Global Precipitation Climatology Project (GPCP: Arkin and Xie, 1994: Rudolf, 1995), the LW90 estimate over the oceans should be viewed with caution. Some of the features discussed below, such as the large precipitation during DJF in the tropical East Pacific and in the southern oceans, or the relatively small extent of the 'oceanic deserts' cannot be identified in the GPCP climatology, for example. In general, the LW90 estimate over the oceans is systematically larger than that found in GPCP and other climatologies. Consequently, some of the differences between ECHAM-4 and LW90 may not be significant due to the large uncertainties in estimated precipation over the oceans.

In Fig. 16 the simulated zonal mean precipitation is compared to the LW90 estimate. Northward of about 10°N the agreement is good, not only in the annual mean but also in the individual seasons. In the tropics, LW90 suggests a double maximum during DJF, with a pronounced peak at about 5°N in the region of the intertropical convergence zone (ITCZ). This zonal mean precipitation peak is not simulated by the model. In JJA, on the other hand, the tropical maximum is similar to LW90 but shifted northward by about 5 degree. As in most other GCMs (e.g., Boer et al., 1992), the most apparent difference between simulation and climatology is found in the SH. While LW90 suggests more precipitation in austral summer (DJF) than in winter (JJA), the model simulates the opposite. In the annual mean, the simulated and observed distributions are fairly similar. However, southward of about 10°N, the simulated precipitation is systematically smaller than observed (see the remarks of caution made earlier).

In Fig. 17, the comparison between simulation and LW90 is confined to continental areas. In general, the agreement is good. The discrepancies are smaller, especially in the SH, than those found in the zonal mean. Accordingly, in the SH, there is a large contribution to the error from ocean areas, where measurements are sparse. Similarly over land, the largest 'errors' are found in data sparse regions like the coast of Antarctica, for example. In the tropics, the simulated precipitation is systematically smaller than LW90 suggests. While the seasonal peaks are similar in magnitude, the simulation indicates a slight poleward shift in the respective summer season,

i.e., the amplitude of the seasonal swing in the tropics is apparently too large (see discussion of Fig. 6). Over the NH continents the differences between ECHAM-4 and LW90 are small.

A comparison of the simulated geographical distribution of annual mean precipitation with LW90 is shown in Fig. 18. For most of the globe, the simulated precipitation is less than in LW90, and the deviations are particularly large over the tropical oceans and over parts of the South Pacific. In the equatorial Indian Ocean the model simulates more precipitation than suggested by LW90. The oceanic 'deserts' (with precipitation of less than 1mm/day) are more extensive in the model simulation, particularly in the SH (see the remarks of caution made earlier). Relatively small deviations from observed climatology (i.e., less than 1 mm/day) are found over most parts of the NH.

In DJF (Fig. 19), the simulated precipitation is smaller than in LW90 over large parts of the SH oceans. By and large, the difference pattern is similar to that of the annual mean but the amplitudes are generally larger. Over the NH oceans the bias is negative as well, but smaller than over the SH oceans, while no systematic differences are found over the NH continents. Less precipitation than observed is simulated over the Mediterranean Sea while more precipitation than observed is simulated over the central and eastern parts of Europe. In ECHAM-3 (Roeckner et al., 1992, Fig. 19A), large positive deviations from climatology are simulated over parts of the SH continents (South Africa, Australia) during austral summer. In these regions, ECHAM-4 overestimates the precipitation as well, but the errors are considerably smaller. Another improvement in ECHAM-4 is the structure of the South Pacific Convergence Zone (SPCZ) which has the correct orientation, while in ECHAM-3 the SPCZ is simulated more parallel to the equator and, moreover, the dry tongue in the equatorial Pacific extends too far to the west.

In JJA (Fig. 20), less precipitation is simulated than suggested by LW90 throughout the tropics, except in the eastern equatorial Indian Ocean. Different from DJF, the simulated precipitation is larger than in LW90 over the SH mid-latitudes (see also Fig. 16). However, as noted earlier, hardly any measurements exist to confirm this bias. Also, the large precipitation rates of more than 5 mm/day observed locally along the coast of Antarctica (in the Indian Ocean sector) are not reproduced by the model. A definite weakness of the model which has been identified through a number of independent estimates (see Figs. 8, 10, 13) is the poor summer monsoon over India and Southeast Asia. This weakness is also evident in the underestimation of precipitation over large parts of the Indian peninsula and China. While the model tends to produce a precipitation maximum along the equatorial Indian Ocean, the observations suggest distinctive maxima further north, along the west coast of India and over the Bay of Bengal along the coast of Burma. A poor monsoon, but less striking, has already been noted in the ECHAM-3 simulation. Over the NH mid-latitude continents, the differences are quite modest. Over North America, the difference pattern is rather patchy. More systematic is the deviation from LW90 over Eurasia where the summer precipitation is generally too small in the simulation.

4.4. INTRASEASONAL AND INTERANNUAL VARIABILITY

The analysis of the intraseasonal transient and stationary variances and covariances follows the standard procedure. The stationary eddies are defined as departures from the respective zonal means, averaged over a season. The variances and covariances of the stationary eddies are calculated for the individual seasonal means and then averaged over the whole seasonal ensemble (i.e., 30 winters simulated with ECHAM-4 and 13 based on ECMWF operational analyses: 1980-1992). Transient eddies are defined as the departure of a 12-hourly value of the respective variable from its seasonal mean. The transient variances and covariances are calculated from the filtered time series in the respective season and then averaged over the whole seasonal ensemble. For time filtering we use the method of Blackmon (1976) for separating high-frequency fluctuations associated with traveling cyclones and anticyclones, and low-frequency fluctuations which characterize processes like decaying cyclones, blocking highs or regime transitions. The frequency response of the filter is the same as used by Blackmon (1976). The so-called bandpass filter emphasizes periods between about 2.5 and 6 days (called the 'bandpass regime' hereinafter), whereas the lowpass filter emphasizes periods between 10 and 90 days (called the 'lowpass regime' hereinafter) with the seasonal cycle removed (Ponater et al., 1990). For both frequency bands, the results are presented in the form of zonally averaged seasonal (DJF) latitude-height cross sections and geographical maps for the NH winter. In addition to the intraseasonal variances and covariances, an estimate of the interannual variability (i.e., standard deviation of geopotential height) during NH winter is shown for each experiment and for the ECMWF analyses as well.

Geopotential height variability

In Fig. 21, latitude-height (pressure) cross sections of intraseasonal variability of geopotential height are shown for both frequency bands (upper and middle panels) and for the stationary eddies (lower panels) as well. Compared to ECMWF analysis (right panels), the bandpass filtered variability is well simulated in general. However, consistent with the positions of the jet cores (see Fig. 4), the model tends to shift the maxima of variability slighty poleward and upward, especially in the SH, and the SH maximum is also somewhat larger than observed. In the lowpass regime (middle panels), the errors are more systematic than for the bandpass regime. For most of the domain, the simulated variability is just about 80% of the observed variability. For the stationary eddies (lower panels) there is hardly any difference between simulation and observed climatology. Exceptions are found in the tropical upper troposphere, where the simulated variability is systematically larger than observed, and in the region of the NH polar night jet, close to the upper boundary of the model domain, where the simulated variability is too small, similar to the deficit in the lowpass regime.

The NH geographical distributions of simulated and observed geopotential height variability at 1000 hPa are shown in Fig. 22 for both frequency bands. The oceanic 'stormtracks' with large bandpass variability in wintertime across the North Pacific and North Atlantic are generally well captured in the simulation. However, the model tends to underestimate bandpass variability in the central parts of both oceans and, particularly, in the Norwegian Sea and in an area between

Scandinavia and the Yenisey river northward of 60°N, approximately. This deficit in bandpass variability could be a lack of cyclonic activity in these regions, also suggested by the positive bias in sea level pressure (see Fig. 12). In the lowpass regime, the shape of the distribution, with maxima centred over the northeastern parts of the North Pacific and North Atlantic, respectively, is reasonably well captured by the model. However, as already discussed in relation to Fig. 21, the simulated values are systematically too small.

The NH geographical distributions of simulated and observed geopotential height variability at 500 hPa are shown in Fig. 23 for both frequency bands. Most of the model weaknesses found at the 1000 hPa level are evident at the 500 hPa level as well. In the middle troposphere, the model underestimates the geopotential height variability in both frequency bands. The underestimation is more systematic in the lowpass regime where the simulated variability, in the centres of activity, is just about 80-85% of the observed. In the bandpass regime, the model reaches about 90% of the observed variability within the centres of activity. Over the North Atlantic, the axis of large bandpass variability has a zonal orientation in the model simulation, while the ECMWF climatology indicates a northeastward bending towards the Norwegian Sea. Consequently, the northerly storm track indicated in the analysis by relatively large bandpass variability along the Siberian coast, extending beyond the Ural, is underrepresented in the simulation. This pattern of reduced variability is consistent with the zonal wind bias at 850 and 200 hPa, with a band of anomalous westerlies over Central Europe and further east, and anomalous easterlies further north stretching from Scandinavia to eastern Siberia (see error maps in Figs. 7 and 9).

The interannual variability of the 1000 hPa (left panels) and 500 hPa (right panels) geopotential height during NH winter is shown in Fig. 24 for both model simulations and for the ECMWF analyses as well. Hence, the standard deviation is calculated from about the same (relatively small) number of samples within the simulated and observed ensembles (i.e., 15 winters in each simulation and 13 winters in the ECMWF analyses, respectively). At both pressure levels, the simulated estimates of interannual variability differ considerably, particularly in the Atlantic centre of variability which is relatively weak in the first experiment (upper panels) but well pronounced in the second one (middle panels). The North Pacific centres, on the other hand, are more similar in the two simulations. According to the simulations, a 15-year period is not sufficient to estimate interannual variability during the NH winter with confidence. Since this will apply, probably, also to observational data, a comparison between the simulated and observed estimates should be made with caution and only a few 'tendencies' are noted here: In both model simulations, the Pacific centre of interannual variability is substantially weaker than in the ECMWF analysis. Less systematic are the differences between simulations and ECMWF analysis in the Atlantic centre. While interannual variability appears to be 'too weak' in the first simulation, it appears to be 'too strong' in the second one.

To some extent, interdecadal variability is likely to affect the estimates of time means and intraseasonal variability as well. This applies less to the model estimates (based on 30 years of data) than to the ECMWF analyses which are available for a much shorter period.

Heat fluxes

In Fig. 25, latitude-height cross sections of zonal mean meridional heat fluxes by transient and stationary eddies are shown for the model simulation (left panels) and ECMWF analysis (right panels), respectively. In the bandpass regime (upper panels) the simulation is fairly realistic. While the pattern is very well captured, the maxima in the lower and upper troposphere are slightly overestimated. In the lowpass regime (middle panels), the hemispheric asymmetry between large heat fluxes in the NH and smaller ones in the SH is well captured by the model. However, in the SH, the heat fluxes are too small and the lower and upper tropospheric maxima are somewhat misplaced. In both hemispheres, the lower tropospheric maximum is simulated too close to the surface (at 950 hPa instead of 850 hPa in the analysis), while the lower stratospheric maximum in the vicinity of the NH polar night jet is underestimated. To some extent, but less distinct, the model deficiencies analysed for the heat fluxes in the lowpass regime can also be identified for the stationary heat fluxes (lower panels). The large fluxes over Antarctica are caused by interpolation to sub-surface pressure levels and should be ignored.

The maps of the meridional heat fluxes by transient eddies at the 850 hPa level (Fig. 26) show a distinct regional separation of the bandpass and lowpass filtered fluxes, respectively. In the bandpass regime (upper panels), large heat fluxes in the western parts of the oceans are caused by developing baroclinic eddies, while in the lowpass regime (lower panels) large heat fluxes over the Bering Sea and the Norwegian Sea are associated with blocking-type flow patterns. This separation is well captured by the model but the maximum over the Norwegian Sea (lower left) is less pronounced than in the ECMWF analysis (lower right). There are a few deviations also in the bandpass regime, such as weaker than observed zonal asymmetry over the North Pacific, i.e., underestimation in the western and central parts and overestimation in the eastern part. Moreover, the maximum off Newfoundland is slightly too weak in the simulation, the fluxes over the Norwegian Sea are too small, as well as the fluxes over the eastern Mediterranean Sea. Most of these differences between simulation and observation are relatively small and may not be significant. However, they are, at least, consistent with the 'error patterns' discussed earlier (see Figs. 12 and 22, for example).

Momentum fluxes

In Fig. 27, latitude-height cross sections of zonal mean meridional momentum fluxes by transient and stationary eddies are shown for the model simulation (left panels) and ECMWF analysis (right panels), respectively. In the bandpass regime (upper panels), there is little disagreement between simulation and analysis. As for most of the other variables, there is a slight upward and poleward displacement of the simulated maxima. Moreover, throughout the troposphere, the SH fluxes are slightly larger than observed. In the lowpass regime (middle panels), there is also good agreement between simulation and analysis but, contrary to the bandpass regime, the simulated fluxes are slightly too weak. In the SH, the stationary eddy momentum fluxes (lower panels) are negligible in both simulation and analysis. In the NH, strong upper tropospheric northward fluxes, centred at 30°N, are flanked by southward fluxes on either side. This pattern is captured in the simulation. However, the model overestimates the

southward fluxes in the near equatorial region while the southward fluxes in high latitudes are substantially smaller than in the analysis. Less significant is the underestimation of the northward fluxes which reach about 85% of the observed ones.

The geographical distributions of the simulated and observed meridional momentum fluxes by transient eddies at the 300 hPa level are compared in Fig. 28. For the bandpass regime (upper panels), there is relatively good agreement between model simulation and ECMWF analysis. The band with northward fluxes between about 30°N and 40°N is well captured in the simulation and also the position of local maxima over the Central Pacific, over the northern part of the United States and over southern Europe. This applies also to the regions with southward fluxes over the northern parts of the oceans. However, there are differences in the details such as a somewhat weak northward flux over the Atlantic (between 30°N and 40°N) and somewhat too small southward fluxes over the Norwegian Sea. The northward fluxes over southern Europe are overemphasized so that the flux convergence further north is too large. The latter feature is consistent with the upper tropospheric westerly wind bias over Central Europe (see Fig. 7). In the lowpass regime (lower panels), the deviations from ECMWF analysis are considerably larger. Regions with large northward fluxes over the United States and North Africa can be identified in both simulation and analysis, but the fluxes are systematically too small in the simulation. Moreover, regions with southward fluxes are much less extensive than in the analysis.

Eddy kinetic energy

In Fig. 29, latitude-height cross sections of zonal mean kinetic energy of transient and stationary eddies are shown for the model simulation (left panels) and ECMWF analysis (right panels), respectively. In the bandpass regime (upper panels), the deviations are quite modest. For example, the kinetic energy is slightly underestimated over the Arctic and somewhat larger than observed in the SH. In the lowpass regime (middle panels) the deviations are more substantial, and the simulated kinetic energy is just 60-70% of the observed. On the other hand, the stationary eddy kinetic energy is fairly well simulated (lower panels), except in the tropical upper troposphere where the model simulates larger values than suggested by the analysis. A comparison of the simulated and observed distributions of transient eddy kinetic energy at the 300 hPa level (Fig. 30) confirms the results obtained for the zonal means. While the simulation is reasonable in the bandpass regime (upper panels), the model substantially underestimates the kinetic energy in the lowpass regime (lower panels). In the bandpass regime, the simulated values are smaller than observed over the continents and over the Arctic, while the simulation is more realistic over the oceans. Here, the largest deviations from the analysis are found in the western Atlantic where the simulated values reach just about 85% of the observed ones. In the lowpass regime, the simulated and analysed patterns are similar in shape, with peak values over the eastern parts of the oceans, but the simulated kinetic energy does not exceed, in general, 60-70% of the observed.

Comparison with ECHAM-3

With a few exceptions, the intraseasonal variability is more successfully simulated with the new model. This applies especially for the lowpass regime, where the ECHAM-4 simulated eddy kinetic energy and the meridional momentum fluxes are substantially higher and more realistic throughout the simulation domain than in the ECHAM-3 simulation (although still not high enough).

In the bandpass regime the improvements are relatively modest. Here, the most significant improvements are found for the NH momentum fluxes which are overestimated in ECHAM-3 by some 30% (in the zonal mean) and underestimated in the lowpass regime by about the same amount. In ECHAM-4, the respective errors are reduced to about 10%. Much of this improvement is due to changes in the Pacific/North America region while the changes in the Atlantic/Europe area less obvious. In the SH, the zonal mean bandpass filtered eddy kinetic energy is slightly too large in ECHAM-4 (by about 15% in the core of the jet stream) while it is close to the analysis in ECHAM-3. In the NH, there is little difference between both models for the zonal mean, but the spatial distribution is substantially improved in ECHAM-4, especially in the Pacific/North America region.

Some improvements can also be noted for the stationary part. For example, compared to ECHAM-3, the geopotential height variability due to stationary eddies in the SH is increased by some 30%, and hardly different from the analysis in the new model. Moreover, the zonal mean kinetic energy of stationary waves is slightly better represented in ECHAM-4.

5.   SUMMARY AND CONCLUSIONS

Two extended AMIP simulations performed with ECHAM-4/T42L19 are analysed and compared with ECMWF operational analyses and Legates and Willmott (1990) precipitation climatology. The model is able to reproduce the observed seasonal mean climate as well as the intraseasonal variability with remarkable skill, and some of the 'errors' noted in Section 4 may well be within the range of observational uncertainty (e.g., precipitation over the oceans). Nevertheless, there are a number of model deviations from observed climatology which probably exceed the observational uncertainty, for example:

•   One of the most apparent deficiencies of general circulation models is a large cold bias in the polar upper troposphere and lower stratosphere. In ECHAM-4, the bias exists throughout the year with the largest values in the respective summer hemisphere (-15K during DJF over Antarctica). The excessive meridional temperature gradient at these heights leads to a strong increase of the zonal wind errors above 200 hPa approximately.

•   Within the troposphere, deviations of temperature and zonal wind from ECMWF analyses are quite modest (i.e., generally less than 2K and 2 m/s, respectively). Exceptions are the upper tropical troposphere which, in all seasons, is 2-3K warmer than

observed and the lower troposphere over the Arctic which has about the same bias during summer.

- In the tropics, the temperatures are very well simulated but the zonal wind, in all seasons, is too westerly above the atmospheric boundary layer. Within the boundary layer, a slight easterly bias is found, i.e. the trades are too strong, particularly in the Pacific Ocean. These errors are indications of overemphasized Walker-type circulations in the equatorial plane. Similar conclusions, based on SSM/I total water vapour, have already been drawn by Chen et al. (1996). During DJF, the tropical westerly wind bias at 200 hPa is predominantly caused by overly strong branches of the subtropical jets in the eastern parts of the Pacific and Atlantic Oceans. In JJA, on the other hand, the upper tropospheric easterlies are underestimated throughout the tropics.

- The somewhat weak tropical easterly jet in ECHAM-4/T42 is related to a poor monsoon simulation which can also be identified on the basis of independent observational data sets. For example, in JJA, the 850 hPa flow over the Arabian Sea is somewhat weak, the surface pressure over large parts of southern and eastern Asia is slightly too high in the simulation and precipitation is underestimated in these regions.

- While the JJA precipitation over these land areas is certainly underestimated in the model simulation, the interpretation of the differences between simulated and observed precipitation over the oceans is more difficult because the observational uncertainty is very large. For example, the excessive DJF precipitation in the tropical East Pacific suggested in the Legates and Willmott analysis is not supported by the GPCP climatology (Arkin and Xie, 1994: Rudolf, 1995). Also, the extent of the 'oceanic deserts' is very different in the climatologies, and the model simulation lies somewhere in between the observational extremes.

- The sea level pressure distribution is generally well simulated. In the Southern Hemisphere, there is some indication of a poleward displacement of both the subtropical high pressure cells and the trough around Antarctica. The latter is slightly deeper than observed in DJF but less pronounced in JJA. In the Northern Hemisphere, the largest errors are found in DJF. The pressure over the Arctic is systematically too high and both the Aleutian and Icelandic lows are slightly weaker than observed. The Azores high on the other hand is too strong and shifted too far eastward over the Mediterranean Sea. This error pattern is consistent with 850 hPa zonal wind error which is westerly at its northern flank over Central Europe and easterly at its southern flank over the Saharan desert. Consistent with these error patterns in sea level pressure and 850 hPa zonal wind is a lack of simulated precipitation in the Mediterranean area and an overestimation further north. During summer, on the other hand, precipitation is underestimated over most parts of Europe.

- The extratropical error patterns in wind and pressure reveal a barotropic structure. All of the errors in the mass and wind distribution noted earlier can be found, even more pronounced, in the middle und upper troposphere as well.

- The simulated intraseasonal variability in the bandpass regime (i.e., in the frequency band between about 2 and 6 days) is slightly smaller than in the ECMWF analyses in the

Northern Hemisphere but slightly larger in the Southern Hemisphere. In the model simulation, the North Atlantic storm track, defined by the area with large geopotential height variability in the bandpass regime, is somewhat deformed. While the analysis indicates a northeastward bending towards the Norwegian Sea, the simulated storm track has a more zonal orientation towards Central Europe.

- More significant are the errors in the lowpass regime (i.e., in the frequency band between about 10 and 90 days). In this frequency band, the model is able to capture just about 80% of the observed geopotential height variability. On the other hand, only small deviations from ECMWF analyses are found for the stationary eddy variances and covariances.

Compared to the previous model version, ECHAM-3/T42L19, which has also been used in a series of AMIP simulations (Bengtsson et al., 1996), the following changes in simulated climatology are noteworthy:

- The tropospheric temperature errors are generally smaller in ECHAM-4. The tropical upper tropospheric warm bias (about 4-5K in ECHAM-3) is reduced by a factor of 2 in ECHAM-4. In the lower troposphere, in all seasons, there is an overall reduction of the regional temperature errors in ECHAM-4. For example, the ECHAM-3 warm bias in boreal summer over large parts of the Northern Hemisphere continents is substantially reduced. The sign of the temperature bias is generally unchanged. One exception is the lower troposphere over the Arctic which is too cold in ECHAM-3, for all seasons, while it is too warm in ECHAM-4 during JJA.

- The extratropical wind systems are somewhat better simulated in ECHAM-4 while the wind errors in the tropics, such as the westerly bias above the boundary layer and the overestimation of the Pacific trades, are larger in ECHAM-4.

- Due to the use of the semi-Lagrangian advection scheme, the distributions of water vapour and cloud water in polar region are much more reliable than in ECHAM-3, and negative concentrations do not occur any more.

- The distribution of precipitation over land is generally more realistic in ECHAM-4. Some of the most substantial errors in ECHAM-3, such as the excessive precipitation over South Africa and Australia during austral summer and the lack of summer precipitation over the northern hemisphere continents are considerably smaller or even negligibly small in ECHAM-4. One exception is the Asian summer monsoon season when the precipitation over India becomes too small and less realistic than in ECHAM-3. The changes of precipitation over the oceans are difficult to judge, due to the uncertainties in the observations. One exception is the pattern of precipitation in the tropical Pacific. In ECHAM-3, the SPCZ lies parallel to equator, in almost all seasons, and the dry equatorial tongue extends too far to the west. In ECHAM-4, the SPCZ has the correct spatial orientation and the extension of the equatorial dry tongue is more realistic as well.

- The intraseasonal variability is generally higher and more realistic than in ECHAM-3.

The improvements in the bandpass regime are relatively modest, with the exception of the momentum fluxes which are substantially more realistic in ECHAM-4 and in very good agreement with ECMWF analyses. Although ECHAM-4 still exhibits a lack of low frequency variability, as discussed earlier, the changes compared to ECHAM-3 are more systematic than in the bandpass regime, and the increased variability in ECHAM-4 can be identified for all variables throughout the whole simulation domain.

- One of the most apparent differences between ECHAM-3 and ECHAM-4 is due to changes in the radiation code. While the amount of solar energy reflected to space is almost identical in both models, ECHAM-4 absorbs considerably more solar radiation in both clear skies (due to water vapour) and in clouds. The resulting reduction in solar radiation available for heating the surface is partly compensated by enhanced downwelling longwave radiation so that the change in net radiation is smaller than that in the individual components. According to surface observations (GEBA), there are strong indications that the surface radiation fluxes in ECHAM-4 are more realistic than in ECHAM-3 (see also Wild et al., 1996). The improved representation of the surface fluxes might be responsible for the improved simulation of temperature and precipitation in ECHAM-4. A general improvement of the land surface climate is also evident through a comparison of the simulated and observed biome distributions.

6.   APPENDIX A

Land surface data

- **Orography** is obtained from the U.S. Navy dataset with resolution of 10 minutes arc on a latitude/longitude grid. The mean terrain heights are then calculated for a T42 Gaussian grid. These data are smoothed using a Gaussian filter with a 50 km radius of influence, and the resulting heights are then spectrally fitted and truncated at the T42 resolution of the model.

- **Background albedo** over snow-free land surfaces is calculated on the basis of three datasets, (i) satellite data of the Earth Radiation Budget Experiment (ERBE), (ii) albedo values for vegetated areas allocated to a high-resolution distribution of major ecosystem complexes of Olson et al. (1983), and (iii) albedo values deduced by Dormann and Sellers (1989) from a radiative transfer model on the basis of vegetation data such as leaf area index and leaf optical properties. The primary data source for deriving the surface albedo over non-vegetated terrain is clear-sky albedo according to ERBE with an atmospheric correction estimated by ECHAM-3. In areas with persistent cloudiness or snowcover, the background albedo is specified according to the prevalent vegetation types. The final product is an annual mean blended albedo with the fractional vegetation cover used as weighting factor.

- **Roughness length** over land consists of three parts (Tibaldi and Geleyn, 1981), resulting (i) from the subgrid-scale variance of orography, (ii) from tall buildings etc. in urban areas, and (iii) from vegetation. As in the previous model versions, the contributions due to orography and urban areas are adopted from the ECMWF model on the basis of the U.S. Navy high-resolution dataset (see orography). However, the vegetation part has been recalculated by specifying individual roughness lengths for a subset of 13 ecosystem complexes derived from the original dataset of Olson et al. (1983), and by employing, finally, the so-called concept of blending height in order to obtain grid averages.

- **Forest ratio** (i.e., the fraction of a grid box covered with forest) is one of the parameters used in the parameterization of snow albedo (cf., Section 3.7.6). Again, as for the compution of surface roughness, the forest fraction is defined consistently with the Olsen et al. dataset and also with the vegetation index described below.

- **Leaf area index and vegetation ratio** (i.e. the fraction of a grid box covered with vegetation) should ideally be inferred from observed or simulated data of net primary production of vegetation. Since suitable global data are not available, we use a provisional approach with values of vegetation ratio and leaf area index assigned to different vegetation types by Lieth and Esser (pers. comm.) for both the growing season and the season of dormancy. In the model, annual mean values are employed which are defined as arithmetic averages of the seasonal extremes. For internal consistency, the Olson et al. ecosystems have been allocated to the vegetation types used by Lieth and Esser.

- **Soil parameters** such as soil moisture capacity, heat capacity and thermal conductivity are redefined from global land surface data sets. In previous ECHAM versions, the boundary conditions for the land surface scheme do not vary horizontally. As a first step towards increased horizontal variability of soil types, the soil water capacity and the soil thermal characteristics such as heat capacity and thermal conductivity are allowed to vary from grid box to grid box. Soil water capacity for each grid box area is computed from a 0.5 degree resolution global dataset of total water-holding capacities (Patterson, 1990). The values are averaged to produce boundary conditions for the various model resolutions. Total water-holding capacity is defined as the field capacity integrated over the rooting depth in the soil. Here, rooting depth is variable and is based on a 1 degree dataset by Willmott and Klink (1986). With regard to soil thermal characteristics, the 0.5 degree global dataset on soil types and textures (Zobler, 1986) has been averaged to the appropriate model resolutions. The information on soil textures is used to define five classes of textures to which thermal conductivity and heat capacity are associated.

References

Arkin, P.A. and P. Xie, 1994: The Global Precipitation Climatology Project: First Algorithm Intercomparison Project. Bull. American Meteorol. Soc., 75, 401-419.

Arpe, K., L. Bengtsson, E. Roeckner and U. Schlese, 1996: Impacts of horizontal resolution on simulated climate in the ECHAM4 model. In preparation.

Bacher, A., J.M. Oberhuber and E. Roeckner, 1996: ENSO dynamics and seasonal cycle in the tropical Pacific as simulated by the ECHAM3 / OPYC3 coupled general circulation model. Max-Planck-Institut für Meteorologie, Report No. 199, Hamburg, 29 pp.

Barkstrom, B., E. Harrison and R. Lee III, 1990: Earth Radiation Budget Experiment. EOS, 71, 297-305.

Baumgartner, A. and E. Reichel, 1975: The World Water Balance. Elsevier, Amsterdam, 179 pp.

Bengtsson, L., K. Arpe, E. Roeckner and U. Schulzweida, 1996: Climate predictability experiments with a general circulation model. Clim. Dyn., 12, 261-278.

Blackadar, A.K. 1962. The vertical distribution of wind and turbulent exchange in a neutral atmosphere. J. Geophys. Res. 67, 3095-3102.

Blackmon, M.L., 1976: A climatological spectral study of the 500 mb geopotential height of the Northern Hemisphere. J. Atm. Sci., 33, 1607-1623.

Boer, G.J., K. Arpe, M. Blackmon, M. Deque, W.L. Gates, T.L. Hart, H. Le Treut, E. Roeckner, D.A. Sheinin, I. Simmonds, R.N.B. Smith, T. Tokioka, R.T. Wetherald, and D. Williamson, 1992: Some results from an intercomparison of the climates simulated by 14 atmospheric general circulation models. J. Geophys. Res., 97, D12, 12771-12786.

Brinkop, S. and E. Roeckner, 1995: Sensitivity of a general circulation model to parameterizations of cloud-turbulence interactions in the atmospheric boundary layer. Tellus, 47A, 197-220.

Bromwich, D.H., 1990: Estimates of Antarctic precipitation. Nature, 343, 627-629.

Chahine, M.T., 1992: The hydrological cycle and its influence on climate. Nature, 359, 373-379.

Charnock, M., 1955: Wind stress on a water surface. Quart. J. Roy. Meteorol. Soc., 81, 639-640.

Chen, C.-T. and E. Roeckner, 1996a: Validation of the Earth radiation budget as simulated by the Max Planck Institute for Meteorology general circulation model ECHAM4 using satellite observations of the Earth Radiation Budget Experiment (ERBE). J. Geophys. Res., 101, D2, 4269-4287.

Chen, C.-T. and E. Roeckner, 1996b: Cloud simulations with the Max Planck Institute for Meteorology general circulation model ECHAM4 and comparison with observations. Max-Planck-Institut für Meteorology, Report No. 193, Hamburg, 49 pp.

Chen, C.-T., E. Roeckner and B.J. Soden, 1996: A comparison of satellite observations and model simulations of column integrated moisture and upper tropospheric humidities. J.

Climate (in press).

Claussen, M. and M. Esch, 1994: Biomes computed from simulated climatologies. Clim. Dyn., 9, 235-243.

Claussen, M., U. Lohmann, E. Roeckner, U. Schulzweida, 1994: A global data set of land-surface parameters. Max-Planck-Institut für Meteorologie, Report No. 135, Hamburg, 34 pp.

Coakley, J.A., Jr. and P. Chylek, 1975: The two-stream approximation in radiation transfer: Including the angle of the incident radiation. J. Atm. Sci., 32, 409-418.

Déqué, M., C. Dreverton, A. Braun and D. Cariolle, 1994: The ARPEGE/IFS atmosphere model: A contribution to the French community climate modelling. Clim. Dyn., 10, 249-266.

Deutsches Klimarechenzentrum (DKRZ), 1992: The ECHAM3 general circulation model. DKRZ Technical Report, No. 6, edited by Modellbetreuungsgruppe, Hamburg.

Dormann, J.L. and P.J. Sellers, 1989: A global climatology of albedo, roughness length and stomatal resistance for atmospheric general circulation models as represented by the Simple Biosphere Model (SiB). J. Appl. Meteorol., 28, 833-855.

Dümenil, L. and Todini, E. 1992. A rainfall-runoff scheme for use in the Hamburg climate model. In: Advances in Theoretical Hydrology, A Tribute to James Dooge (Ed. J.P. O' Kane). European Geophysical Society Series on Hydrological Sciences, 1, Elsevier Press, Amsterdam, 129-157.

ECMWF Research Department, 1991: ECMWF Forecast Model, Physical Parameterization. Research Manual 3, 3rd Edition, Meteorological Bulletin, European Centre for Medium-Range Weather Forecasts, Reading, England.

Elsasser, W.M., 1942: Heat transfer by infrared radiation in the atmosphere. Harvard Meteorological Studies No. 6, Harvard University Press, Cambridge, Mass., 43 pp.

Feichter, J., U. Lohmann and I. Schult, 1996: The atmospheric sulfur cycle in ECHAM4 and its impact on the shortwave radiation. Climate Dynamics (submitted).

Fouquart, Y. and B. Bonnel, 1980: Computations of solar heating of the Earth's atmosphere: A new parameterization. Beitr.Phys.Atmos., 53, 35-62.

Francis, P.N., A. Jones, R.W. Saunders, K.P. Shine, A. Slingo and Z. Sun, 1994: An observational study of the radiative properties of cirrus: Some results from ICE'89. Quart. J. Roy. Meteor. Soc., 120, 809-848.

Fritsch, J.M. and C.G. Chapell, 1980: Numerical prediction of convectively driven mesoscale pressure systems. Part I: Convective parameterization. J. Atm. Sci., 37, 1722-1733.

Garratt, J.R., 1992: The atmospheric boundary layer. Cambridge Atmospheric and Space Science Series, eds. J.T.Houghton, M.J. Rycroft, A.J. Dessler, Cambridge University Press, Cambridge, 316 pp.

Garratt, J.R. and A. Prata, 1996: Downwelling longwave fluxes at continental surfaces - A comparison of observations with GCM simulations and implications for the global land-surface radiation budget. J. Climate, 9, 646-655.

Gates, W.L., 1992: AMIP: The atmospheric model intercomparison project. Bull. Am. Meteorol. Soc., 73, 35-62.

Gilgen, H., M. Wild, T. Konzelmann and A. Ohmura, 1996: Global climatology of shortwave incoming radiation at the surface using the Global Energy Balance Archive (GEBA). J. Climate (submitted).

Giorgetta, M. and M. Wild, 1995: The water vapour continuum and its representation in ECHAM4. Max-Planck-Institut für Meteorologie, Report No. 162, Hamburg, 38 pp.

Hack, J.J., B.A. Boville, B.P. Briegleb, J.T. Kiehl, P.J. Rasch and D.L. Williamson, 1993: Description of the NCAR community climate model (CCM2). National Center for Atmospheric Research, NCAR TN-382+STR, Boulder, Colorado, 108 pp.

Hahn, C.J., S.G. Warren and J. London, 1994: Climatological data for clouds over the globe from surface observations, 1982-1991: The total cloud edition, ORNL/CDIAC-72, NDP-026A, Oak Ridge National Laboratory, Oak Ridge, Tennessee, USA.

Hartmann, D., 1993: Radiative effects of clouds on Earth's climate. In Aerosol-Cloud-Climate Interactions, ed. P.V. Hobbs, 151-173, Academic Press.

Heymsfield, A.J., 1977: Precipitation development in stratiform ice clouds. A microphysical and dynamical study. J.Atmos.Sci., 34, 367-381.

Holtslag, A.A.M. and B.A. Boville, 1993: Local versus nonlocal boundary-layer diffusion in a global climate model. J. Climate, 6, 1825-1842.

Johnson, D.W., 1993: Parameterisation of the cloud topped boundary layer: Aircraft Measurements. ECMWF Workshop Proceedings 'Parameterization of the cloud topped boundary layer', 77-117, Reading.

Joseph, J.H., W.J. Wiscombe and J.A. Weinman, 1976: The Delta-Eddington approximation for radiative transfer. J. Atm. Sci., 33, 2452-2459.

Koepke, P., M. Hess, I. Schult and E. Shettle, 1996: Global aerosol data set. Theor. Appl. Clim. (in press).

Large, W.G. and S. Pond, 1982: Sensible and latent heat flux measurements over the ocean. J. Phys. Oceanogr., 12, 464-482.

Legates, D.R. and C.J. Willmott, 1990: Mean seasonal and spatial variability in gauge corrected global precipitation. J. Climatol., 10, 111-127.

Lohmann, U., E. Roeckner, W.D. Collins, A.J. Heymsfield, G. McFarquhar and T.P. Barnett, 1995: The role of water vapor and convection during the Central Equatorial Pacific Experiment from observations and model simulations. J. Geophys. Res., 100, D12, 26229-26245.

Louis, J.F., 1979: A parametric model of vertical eddy fluxes in the atmosphere. Bound. Layer Meteor., 17, 187-202.

Ma, Q. and R.H. Tipping, 1992: A far wing line shape theory and its application to the foreign-broadened water continuum absorption (III). J. Chem. Phys., 97, 818-828.

Mailhot, J. and Benoit, R. 1982. A finite-element model of the atmospheric boundary layer suitable for use with numerical weather prediction models. J. Atmos. Sci. 39, 2249-2266.

Manzini, E., N.A. McFarlane and C. McLandress, 1996: Impact of the Doppler spread parameterization on the simulation of the middle atmosphere circulation using the ECHAM4 general circulation model. Max-Planck-Institut für Meteorology, Report No. 214, Hamburg, 29 pp.

Matveev, L.T., 1984: Cloud dynamics. Atmospheric Sciences Library. D. Reidel Publishing Company, Dordrecht, 340 pp.

McFarlane, N.A., 1987: The effect of orographically excited gravity-wave drag on the general circulation of the lower stratosphere and troposphere. J. Atm. Sci., 44, 1775-1800.

McFarlane, N.A., G.J. Boer, J.-P. Blanchet and M. Lazare, 1992: The Canadian Climate Centre second-generation general circulation model and its equilibrium climate. J.Climate, 5, 1013-1044.

Mellor, G.L. and T. Yamada, 1982: Development of a turbulence closure model for geophysical fluid problems. Rev. Geophys. Space Phys., 20, 851-875.

Miller, M.J., T.N. Palmer and R. Swinbank, 1989: Parameterization and influence of sub-grid scale orography in general circulation and numerical weather prediction models. Met. Atm. Phys., 40, 84-109.

Miller, M.J., A.C.M. Beljaars and T.N. Palmer, 1992: The sensitivity of the ECMWF model to the parameterization of evaporation from tropical oceans. J. Climate, 5, 418-434.

Minnis, P., P.W. Heck, D. Young, C.W Fairall and J.B. Snider, 1992: Stratocumulus cloud properties derived from simultaneous satellite and island-based instrumentation during FIRE. J. Appl. Meteor., 31, 317-339.

Morcrette, J.-J., 1984: Sur la paraméterisation du rayonnement dans les modèles de la circulation générale atmosphérique. PhD dissertation No. 630, University of Lille.

Morcrette, J.-J. and Y. Fouquart, 1985: On systematic errors in parametrized calculations of longwave radiation transfer. Quart. J. Roy. Meteor. Soc., 111, 691-708.

Morcrette, J.-J., L. Smith and Y. Fouquart, 1986: Pressure and temperature dependence of the absorption in longwave radiation parameterizations. Beitr. Phys. Atmosph., 59, 455-469.

Nordeng, T.E., 1996: Extended versions of the convective parameterization scheme at ECMWF and their impact on the mean and transient activity of the model in the tropics. Quart. J. Roy. Meteorol. Soc. (submitted).

Oberhuber, J.M., 1993: Simulation of the Atlantic circulation with a coupled sea ice - mixed layer - isopycnal general circulation model. Part I: Model description. J. Phys. Oceanogr., 22, 808-829.

Ohmura, A. and H. Gilgen, 1991: Global Energy Balance Archive (GEBA). World Climate Program - Water Project A7, Rep. 2: The GEBA Database, Interactive Application, Retrieving Data. Verlag der Fachvereine, Zürich, 60 pp.

Olson, J.S., J.A. Watts, L.J. Allison, 1983: Carbon in live vegetation of major world ecosystems. ORNL-5862, Oak Ridge Laboratory, Oak, Ridge, Tennessee, USA.

Palmer, T.N., G.J. Shutts and R. Swinbank, 1986: Alleviation of a systematic westerly bias in general circulation and numerical weather prediction models through an orographic gravity wave drag parameterization. Quart. J. Roy. Meteor. Soc., 112, 1001-1031.

Paltridge, G.W. and C.M.R. Platt, 1976: Radiative Processes in Meteorology and Climatology. Elsevier, Amsterdam, 318 pp.

Patterson, K.A., 1990: Global distributions of total and total-avaiable soil water-holding capacities. M.S. thesis, Dept. of Geography, University of Delaware, 119 pp.

Ponater, M., E. Kirk and U. Schlese, 1990: GCM-simulated transient variability in the Northern Hemisphere extratropics and its sensitivity to sea surface temperature variation. Beitr. Phys. Atmosph., 63, 189-204.

Prentice, I.C., W. Cramer, S.P. Harrison, R. Leemans, R.A. Monserud and A.M Solomon, 1992: A global biome model based on plant physiology and dominance, soil properties and climate. J. Biogeogr., 19, 117-134.

Rasch, P.J. and D.L. Williamson, 1990: Computational aspects of moisture transport in global models of the atmosphere. Quart. J. R. Met. Soc., 116, 1071-1090.

Roberts, R.E., J.E.A., Selby and L.M. Biberman, 1976: Infrared continuum absorption by atmospheric water vapor in the 8-12 mm window. Appl. Opt., 15, 2085-2090.

Rockel, B., E. Raschke and B. Weyres, 1991: A parameterization of broad band radiative transfer properties of water, ice and mixed clouds. Beitr. Physik Atmos., 64, 1-12.

Rodgers, C.D., 1967: The radiative heat budget of the troposphere and lower stratosphere. Planetary Circulation Project, Rep. No. A2, Dept. of Meteorology, Mass. Inst. of Technology, Cambridge, Mass., 99 pp.

Roeckner, E., K. Arpe, L. Bengtsson, S. Brinkop, L. Dümenil, M. Esch, E. Kirk, F. Lunkeit, M. Ponater, B. Rockel, R. Sausen, U. Schlese, S. Schubert and M. Windelband, 1992: Simulation of the present-day climate with the ECHAM model: Impact of model physics and resolution. Max-Planck-Institut für Meteorologie, Report No. 93, Hamburg, 171 pp.

Roeckner, E., 1995: Parameterization of cloud radiative properties in the ECHAM4 model. In: Proceedings of the WCRP Workshop on "Cloud Microphysics Parameterizations in Global Atmospheric Circulation Models", May 23-25, 1995, Kananaskis, Alberta, Canada, WCRP-Report No. 90, 105-116, WMO/TD-No. 713.

Roeckner, E. and K. Arpe, 1995: AMIP experiments with the new Max Planck Institute for Meteorology Model ECHAM4. In: Proceedings of the "AMIP Scientific Conference", May 15-19, 1995, Monterey, USA, WCRP-Report No. 92, 307-312, WMO/TD-No. 732.

Roeckner, E., J.M. Oberhuber, A. Bacher, M. Christoph and I. Kirchner, 1996: ENSO variability and atmospheric response in a global coupled atmosphere-ocean GCM. Max-Planck-Institut für Meteorologie, Clim. Dyn. (in press).

Rudolf, B., 1995: Die Bestimmung der zeitlich-räumlichen Struktur des globalen Niederschlags. Berichte des Deutschen Wetterdienstes, 196, Offenbach am Main, 153 pp.

Simmons, A.J. and R. Strüfing, 1981: An energy and angular momentum conserving finite-difference scheme, hybrid coordinates and medium-range weather prediction. ECMWF Technical Report No. 28, Reading, 68 pp.

Simmons, A.J., D.M. Burridge, M. Jarraud, C. Girard and W. Wergen, 1989: The ECMWF medium-range prediction models: Development of the numerical formulations and the impact of increased resolution. Meteorol. Atmos. Phys., 40, 28-60.

Simpson, J. and V. Wiggert, 1969: Models of precipitating cumulus towers. Mon. Wea. Rev., 97, 471-489.

Smith, R.N.B. 1990. A scheme for predicting layer clouds and their water content in a general circulation model. Quart. J. R. Met. Soc. 116, 435-460.

Stendel, M. and L. Bengtsson, 1996: Monitoring the temperature of the troposphere by means of a general circulation model. Max-Planck-Institut für Meteorologie, Report No. 186, Hamburg, 26 pp.

Stephens, G.L. and C.M.R. Platt, 1987: Aircraft observations of the radiative and microphysical properties of stratocumulus and cumulus cloud fields. J. Clim. Appl. Meteor., 26, 1243-1269.

Stephens, G.L., S.-C. Tsay, P.W., Stackhouse, Jr. and P.J. Flateau, 1990: The relevance of the microphysical and radiative properties of cirrus clouds to climate and climate feedback. J. Atm. Sci., 47, 1742-1753.

Sundqvist, H., 1978: A parameterization scheme for non-convective condensation including prediction of cloud water content. Quart. J. R. Met. Soc., 104, 677-690.

Sundqvist, H., E. Berge and J.E. Kristjansson, 1989: Condensation and cloud parameterization studies with a mesoscale numerical weather prediction model. Mon.Wea.Rev., 117, 1641-1657.

Tibaldi, S. and J.-F. Geleyn, 1981: The production of a new orography, land-sea mask and associated climatological surface fields for operational purposes. ECMWF Techn. Memo., 40, Reading.

Tiedtke, M., 1989: A comprehensive mass flux scheme for cumulus parameterization in large-scale models. Mon. Wea. Rev., 117, 1779-1800.

Turner, J.S., 1963: The motion of buoyant elements in turbulent surroundings. J. Fluid Mech., 16, 1-16.

Washington, W.M. and D.L. Williamson, 1977: A description of the NCAR GCM's. In: General Circulation Models of the Atmosphere, J. Chang, ed., Methods in Computational Physics, 17, 111-172, Academic Press.

Wild, M., A. Ohmura, H. Gilgen and E. Roeckner, 1995: Validation of general circulation model simulated radiative fluxes using surface observations. J. Climate, 8, 1309-1324.

Wild, M., A. Ohmura, H. Gilgen, E. Roeckner and M. Giorgetta, 1996: Improved representation

of surface and atmospheric radiation budgets iin the ECHAM4 general circulation model. Max-Planck-Institut für Meteorologie, Report No. 200, Hamburg, 32 pp.

Williamson, D. L. and P.J. Rasch, 1994: Water vapor transport in the NCAR CCM2. Tellus 46A, 34-51.

Willmott, C. and K. Klink, 1986: A representation of the terrestrial biosphere for use in global climate studies. In: Proceedings of the ISLSCP Conference, Rome, 2-6 December, 1985, European Space Agency, ESA SP-248.

Xu, K.M. and S.K. Kruger, 1991: Evaluation of cloudiness parameterizations using a cumulus ensemble model. Mon. Wea. Rev., 119, 342-367.

Zhang, M.H., R.D. Cess, T.Y. Kwon and M.H. Chen, 1994: Approaches of c omparison for clear-sky radiative fluxes from general circulation models with Earth Radiation Budget Experiment data. J. Geophys. Res., 99, 5515-5523.

Zobler, L., 1986: A world soil file for global climate modeling. National Aeronautics and Space Administration Technical Memorandum 87802.

Radiative flux Units: W/m^2	ECH-3 all sky	ECH-4 all sky	ERBE* all sky	ECH-3 clear sky	ECH-4 clear sky	ERBE* clear sky
Incoming shortwave	341.3	341.3	341.3	341.3	341.3	341.3
Outgoing shortwave	103.9	104.4	101	56.8	55.1	53
Net shortwave	237.4	236.9	240	284.5	286.2	288
Albedo (%)	30.4	30.6	29.8	16.6	16.3	15.6
Outgoing longwave	233.4	235.3	234	262.3	264.0	264
Total	4.0	1.6	6	22.2	22.2	24

Table 4 : Global annual mean TOP-OF-ATMOSPHERE radiation budget
* Observations (ERBE) according to Hartmann (1993)

Radiative flux Units: W/m^2	ECH-3 all sky	ECH-4 all sky	GEBA* all sky	ECH-3 clear sky	ECH-4 clear sky
Shortwave down	193.6	176.3	176 ±12	248.0	235.0
Shortwave up	48.1	44.9	42	61.5	59.9
Shortwave net	145.5	131.4	134	186.5	175.1
Albedo (%)	24.8	25.5	24	24.8	25.5
Longwave down	300.1	306.4	305 ±8	280.7	290.6
Longwave up	370.9	369.8	374 ±5	370.9	369.8
Longwave net	- 70.8	- 63.4	- 69	- 90.2	- 79.2
Total	74.7	68.0	65 ±5	96.3	95.9

Table 5: Annual mean LAND-SURFACE radiation budget
* Observations (GEBA) according to Garratt and Prata (1996)

Radiative flux Units: W/m^2	ECH-3 all sky	ECH-4 all sky	GEBA* all sky	ECH-3 clear sky	ECH-4 clear sky
Shortwave down	191.4	171.2	172*	253.8	247.8
Shortwave up	24.4	23.4	22**	32.2	33.7
Shortwave net	167.0	147.8	150**	221.6	214.1
Albedo (%)	12.7	13.6	13**	12.7	13.6
Longwave down	333.4	344.1	-	311.5	323.4
Longwave up	397.0	396.7	-	397.0	396.7
Longwave net	- 63.6	- 52.6	-	- 85.5	- 73.3
Total	103.4	95.2	-	136.1	140.8

Table 6: Global annual mean SURFACE radiation budget
* Observations (GEBA 1995) after Gilgen et al. (1996, Table 1)
** Calculated from GEBA 'shortwave down" assuming a surface albedo of 13%

Radiative flux Units: W/m^2	ECH-3 all sky	ECH-4 all sky	GEBA/ ERBE	ECH-3 clear sky	ECH-4 clear sky
Shortwave net	70.4	89.1	90	62.9	72.1
Longwave net	- 169.8	- 182.7	-	- 176.8	- 190.7
Total	- 99.4	- 93.6	-	- 113.9	- 118.6

Table 7: Global annual mean ATMOSPHERIC radiation budget

Cloud rad. forcing Units: W/m^2	ECH-3 TOA	ECH-4 TOA	ERBE TOA	ECH-3 SFC	ECH-4 SFC	ECH-3 ATM	ECH-4 ATM
Shortwave	- 47.1	- 49.3	- 48	- 54.6	- 66.3	7.5	17.0
Longwave	28.9	28.7	30	21.9	20.7	7.0	8.0
Total	- 18.2	- 20.6	- 18	- 32.7	- 45.6	14.5	25.0

Table 8: Global annual mean cloud radiative forcing for
top-of-atmosphere (TOA), surface (SFC) and atmosphere (ATM)

Flux in W/m^2	ECH-3			ECH-4		
	land	sea+ice	globe	land	sea+ice	globe
Shortwave radiation	145.5	175.4	167.0	131.4	154.3	147.8
Longwave radiation	- 70.7	- 60.8	- 63.6	- 63.4	- 48.4	- 52.6
Sensible heat	- 23.1	- 9.3	- 13.2	- 19.1	- 9.1	- 11.9
Latent heat	- 38.0	- 96.5	- 80.0	- 40.6	- 97.6	- 81.6
Snow melt	- 0.7	-	- 0.2	- 0.7	-	- 0.2
Total heat	12.9	8.8	10.0	7.6	- 0.8	1.5
Linearization of total heat flux	- 12.9	-	- 3.6	- 7.6	-	- 2.2
Heat conduction through sea ice (positive upward)	-	1.2	0.9	-	1.2	0.9

Table 9: Annual mean surface heat budget

*snowfall on glaciers (Bromwich, 1990) subtracted from runoff	ECH-3	ECH-4	Baumgartner and Reichel (1975)	Chahine (1992, Fig.1)
GLOBE Units: mm/d				
Precipitation	2.760	2.804	2.6	2.7
Evaporation	2.762	2.816	2.6	2.7
Evap - Precip	0.002	0.012	0.	0.
SEA Units: $10^{12}m^3$/yr				
Precipitation	401.2	414.1	385	398
Evaporation	445.6	451.0	425	434
Evap - Precip	44.4	36.9	40	36
LAND Units: $10^{12}m^3$/yr				
Precipitation	112.4	108.0	111	107
Evaporation	68.4	73.2	71	71
Runoff (ice-free land)	40.6	32.7	37*	33*
Snowfall on glaciers	3.41	2.31	3*	3*

Table 10: Annual mean hydrological cycle

	ECH-3			ECH-4		
Variable	land	sea+ice	globe	land	sea+ice	globe
Surface air temperature (°C)	8.49	17.2	14.7	8.39	17.2	14.7
Column water vapour (kg/m^2)	18.9	27.8	25.3	18.3	26.8	24.4
Column cloud water (g/m^2)	65.7	88.5	82.1	57.9	87.0	78.8
Total cloud cover (%)	48.6	53.6	52.2	53.3	62.4	59.9

Table 11: Annual mean climate variables

No	Biome (area in 10^6 km^2)	ECH-3 (T42)	ECH-4 (T42)	OBS (0.5°)	ECH-3 Error	ECH-4 Error
1	Tropical rain forest	5.5	9.6	8.2	-2.7	+1.4
2	Tropical seasonal forest	7.0	7.0	7.3	-0.3	-0.3
3	Savanna	22.5	17.9	17.2	+5.3	+0.7
4	Warm mixed forest	5.2	5.7	6.2	-1.0	-0.5
5	Temperate deciduous forest	4.9	6.4	5.8	-0.9	+0.6
6	Cool mixed forest	4.1	6.7	4.9	-0.8	+1.8
7	Cool conifer forest	2.8	2.5	3.0	-0.2	-0.5
8	Taiga	11.6	12.6	12.5	-0.9	+0.1
9	Cold mixed forest	0.6	0.7	0.7	-0.1	-0.0
10	Cold deciduous forest	1.8	3.1	3.8	-2.0	-0.7
11	Xerophytic woods / shrub	8.6	9.1	11.3	-2.7	-2.2
12	Warm grass / shrub	13.3	11.9	10.0	+3.3	+1.9
13	Cool grass / shrub	2.5	2.6	5.7	-3.2	-3.1
14	Tundra	12.0	11.4	9.7	+2.3	+1.7
15	Hot desert	22.9	19.5	21.0	+1.9	-1.5
16	Cool desert	1.9	0.9	4.9	-3.0	-4.0
	Total area (10^6 km^2) without Antarctica	127.2	127.6	132.2	30.6* (23%)	21.0* (16%)

Table 12: Biome areas derived from simulations and observations (Prenctice et al., 1992).
* Defined as Σ |b_i(model) - b_i(obs)| where the summation is over all biome types b_i
(i = 1,2,....,16)
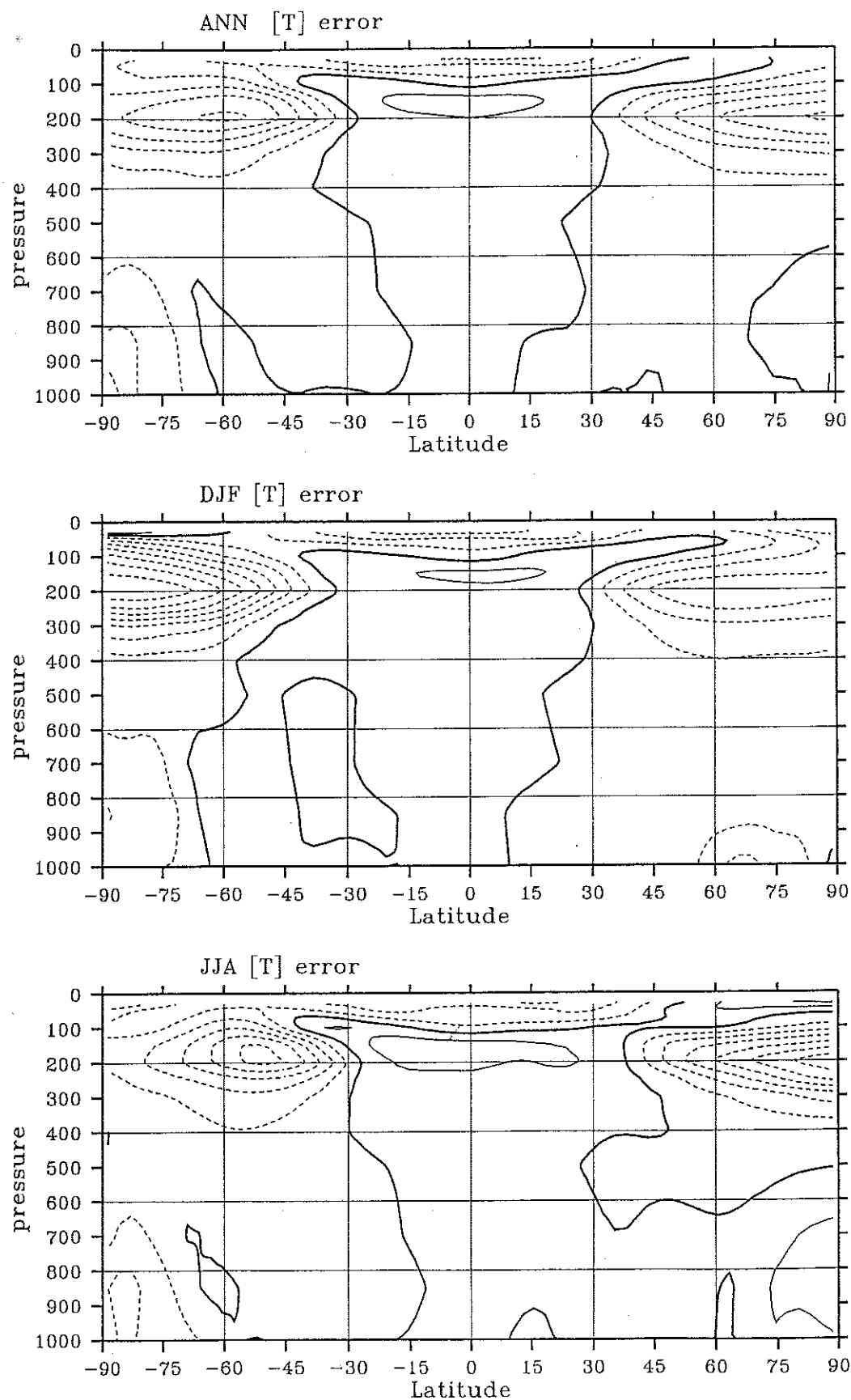
Figure 1   Latitude-height (pressure in hPa) cross sections of zonal mean temperature error (ECHAM-4 simulation - ECMWF analysis). Contour spacing is 2°C. Negative (zero) errors are indicated by dashed (bold) contours.
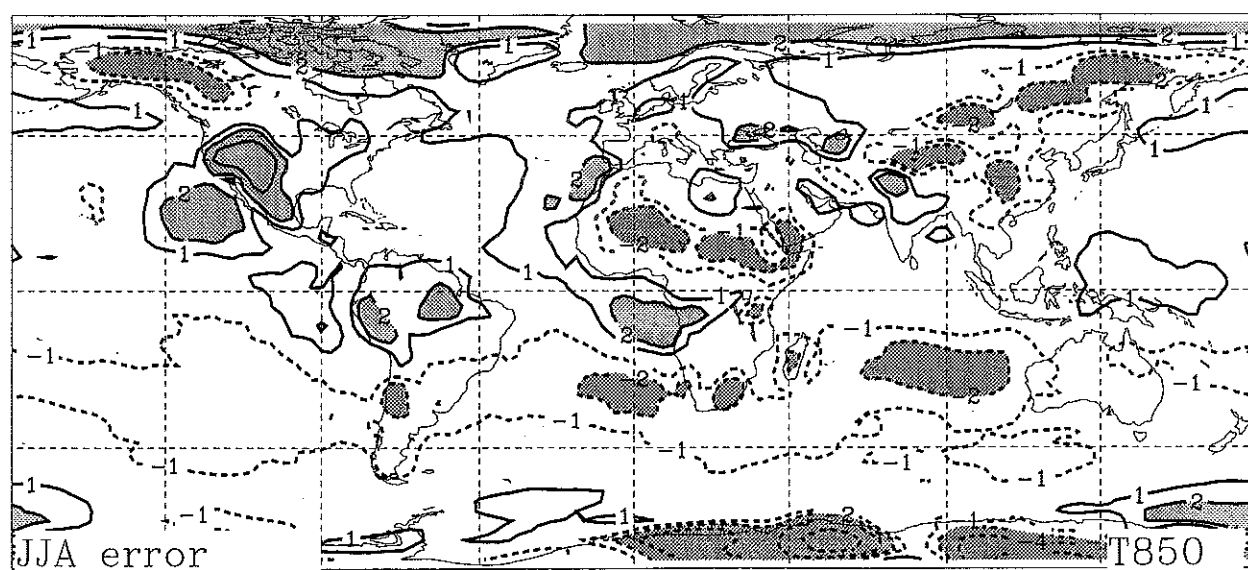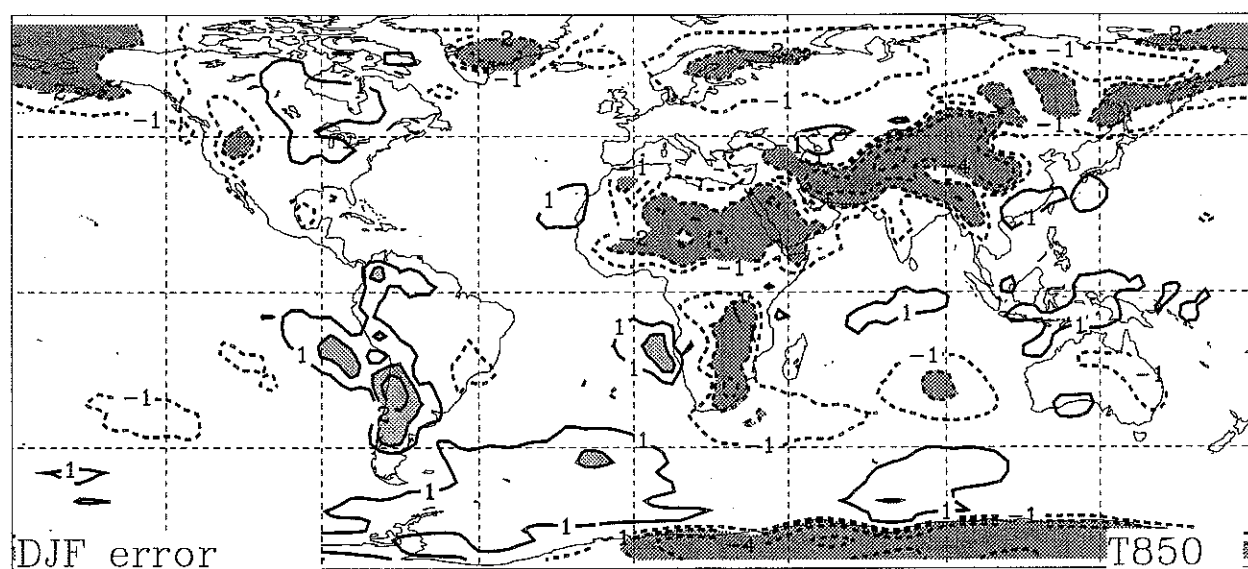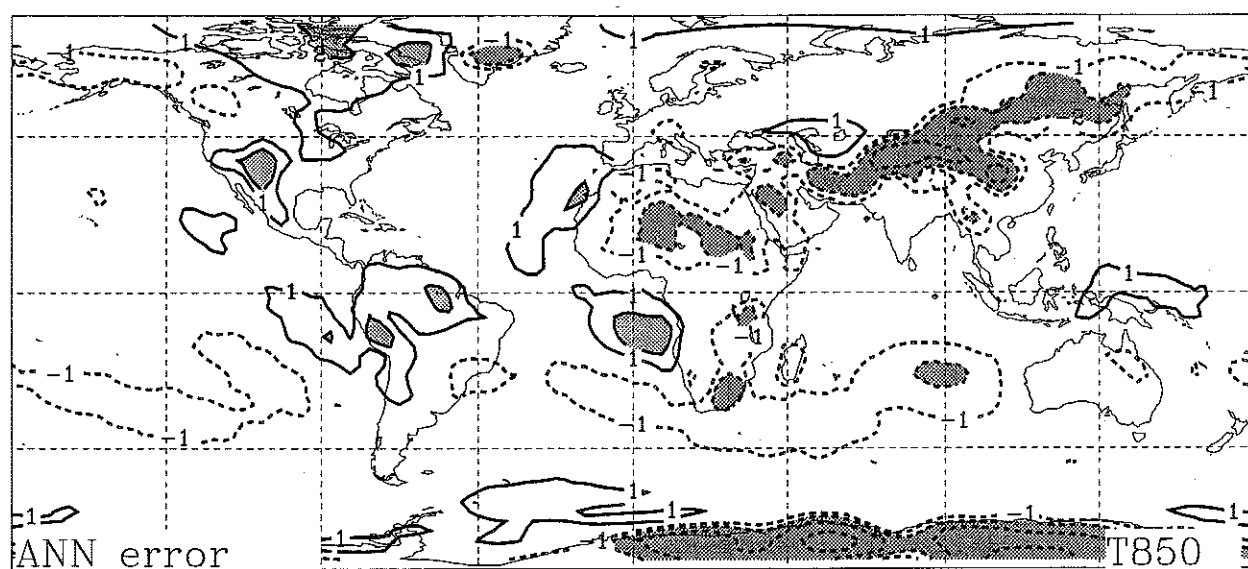
Figure 2   Maps of 850 hPa temperature error (ECHAM-4 simulation - ECMWF analysis).
Contours: ± 1, 2, 4, 6, 8 °C. Negative contours stippled. In shaded areas the errors
exceed ±2 °C (dark: cold bias, light: warm bias).
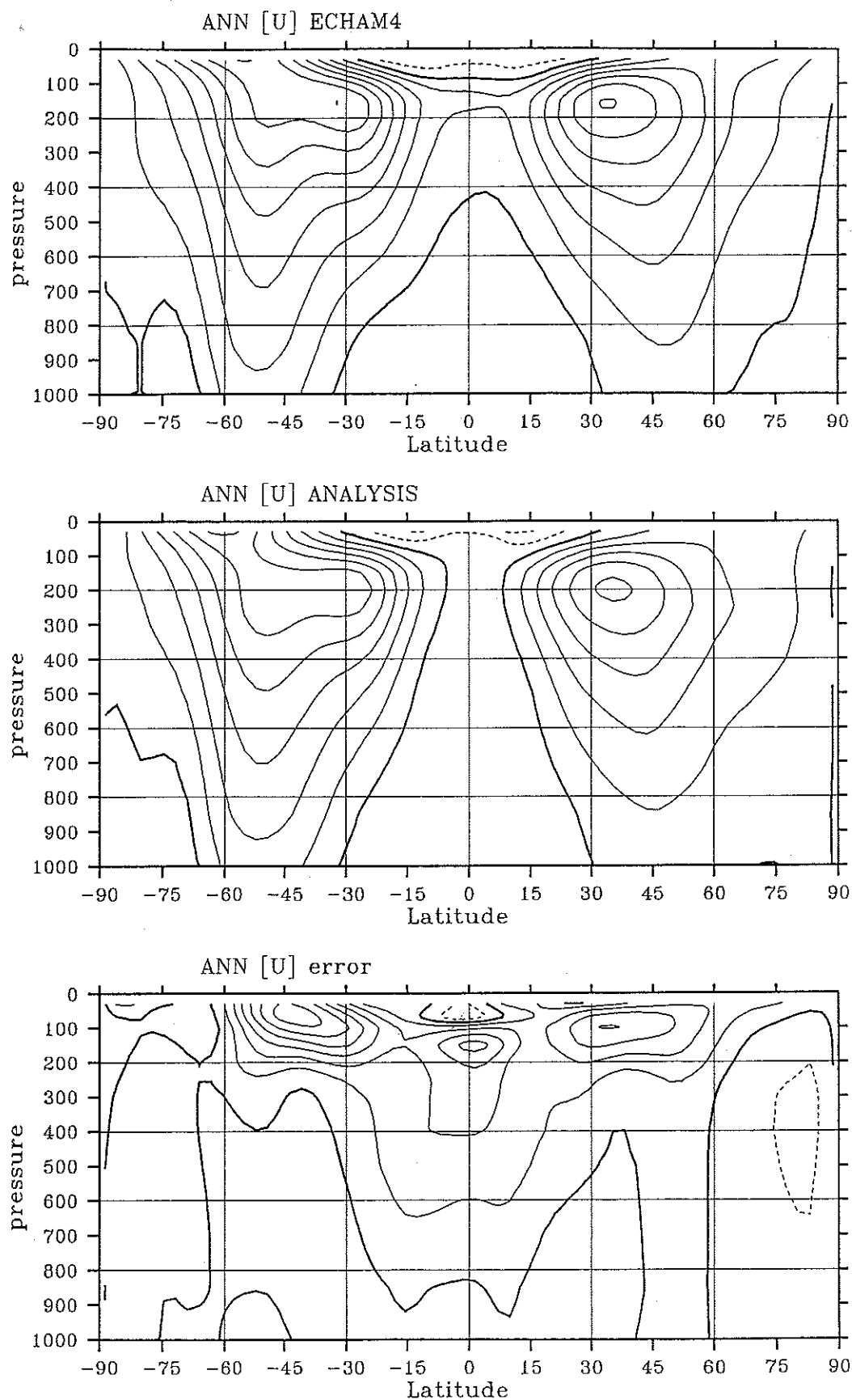
Figure 3   Latitude-height (pressure in hPa) cross sections of zonal and annual mean zonal wind in ECHAM-4 simulation (top), ECMWF analysis (middle) and for the difference (bottom). Contour spacing is 5 m/s for simulation and analysis, and 2 m/s for the difference ('error'). Negative (zero) values are indicated by dashed (bold) contours.

63

DJF [U] ECHAM4

DJF [U] ANALYSIS

DJF [U] error
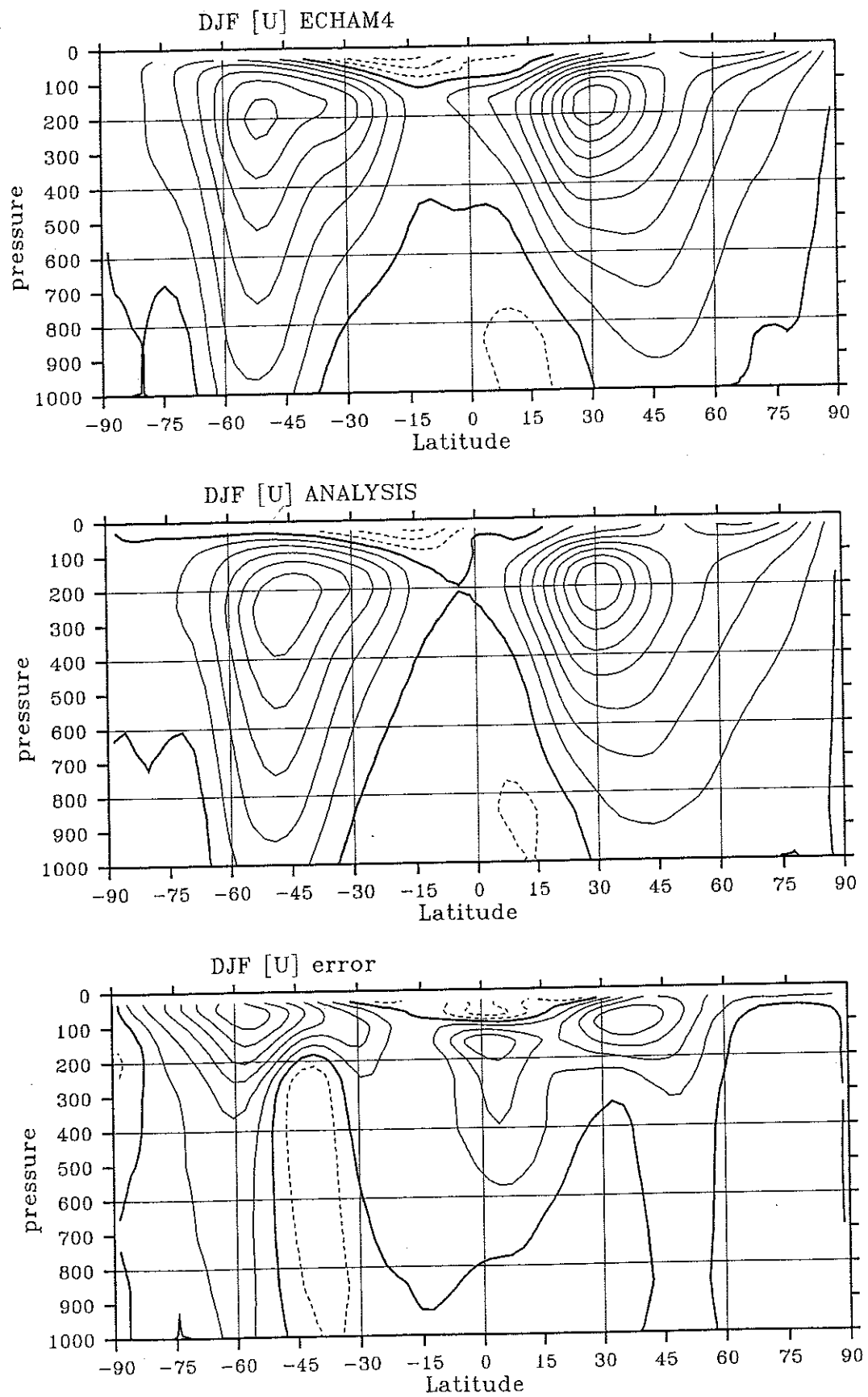
Figure 4   As in Fig. 3 except for the DJF season.

64
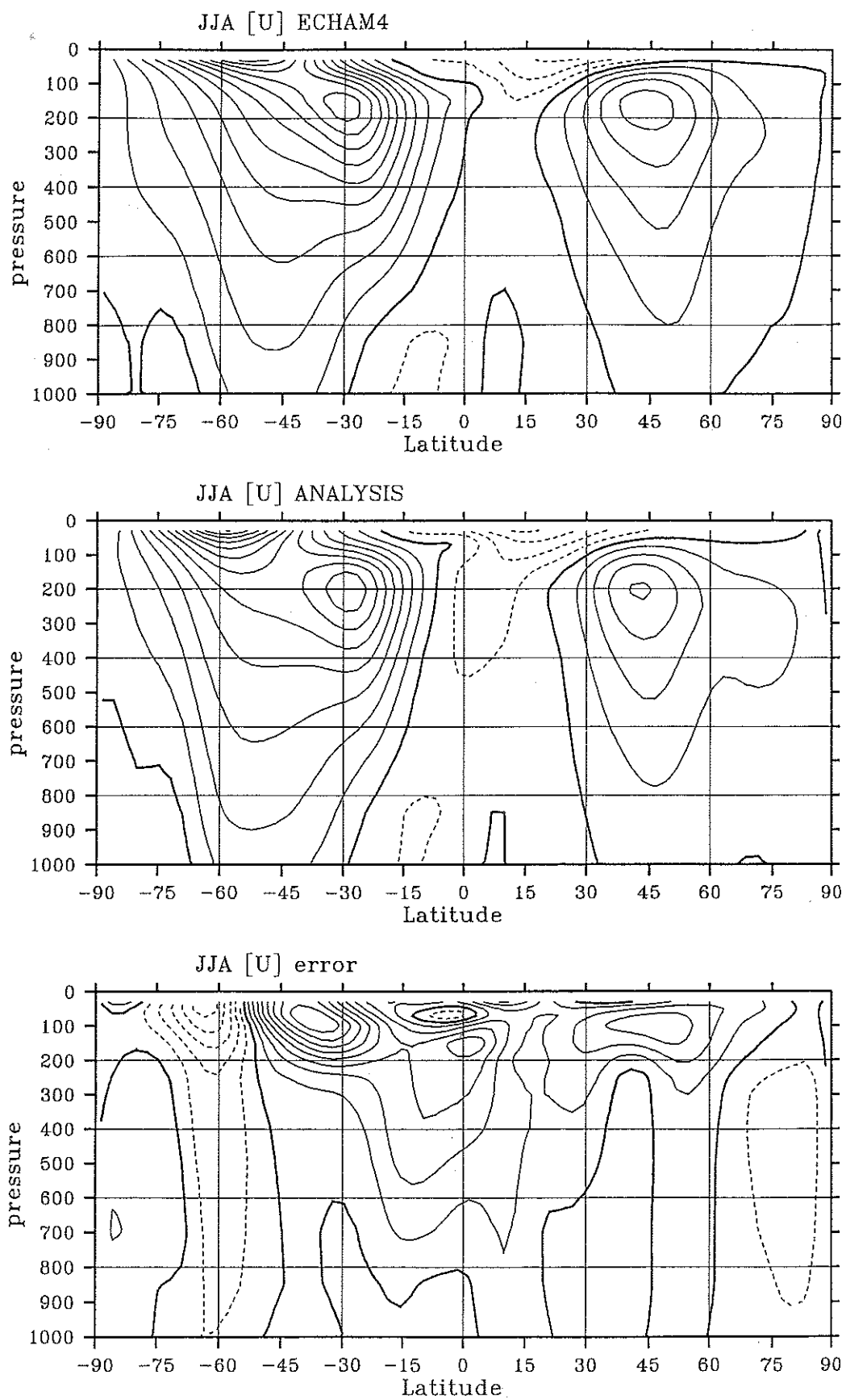
Figure 5   As in Fig. 3 except for the JJA season.
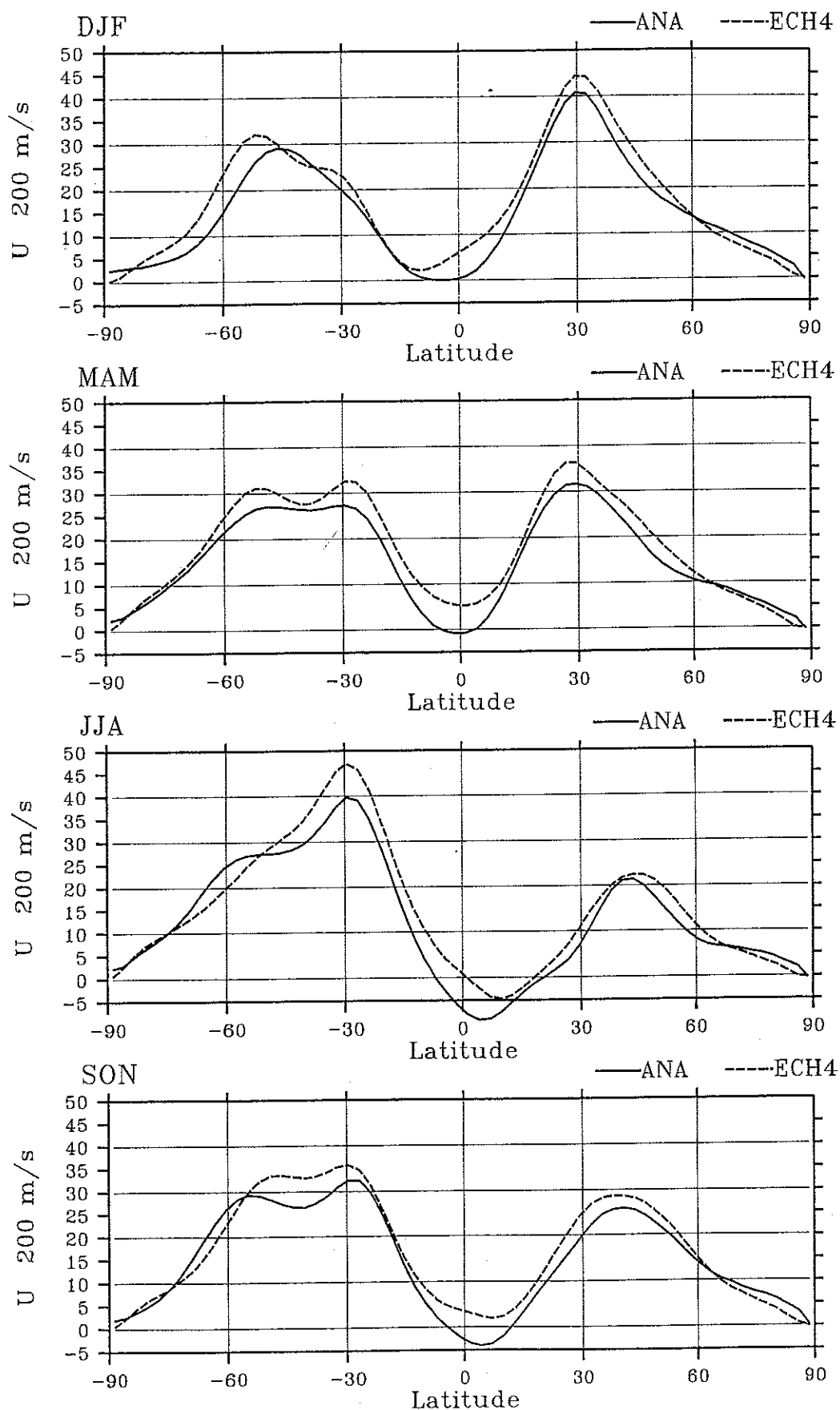
Figure 6   Meridional distribution of zonally and seasonally averaged zonal wind (m/s) at 200 hPa for the ECHAM-4 simulation (dashed curves) and ECMWF analysis (solid curves).
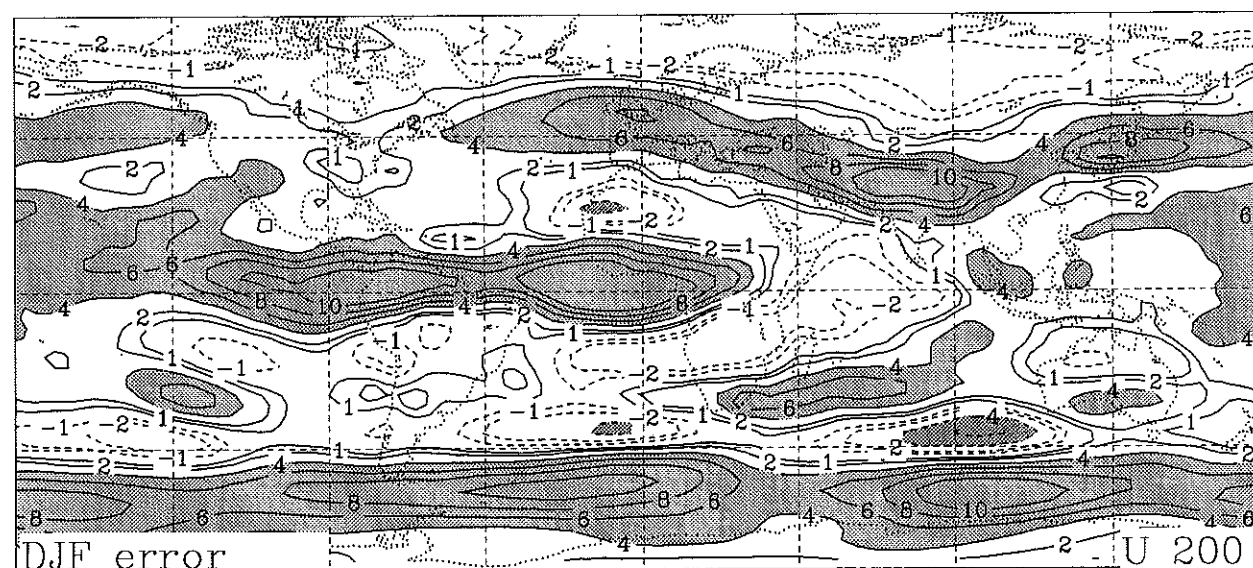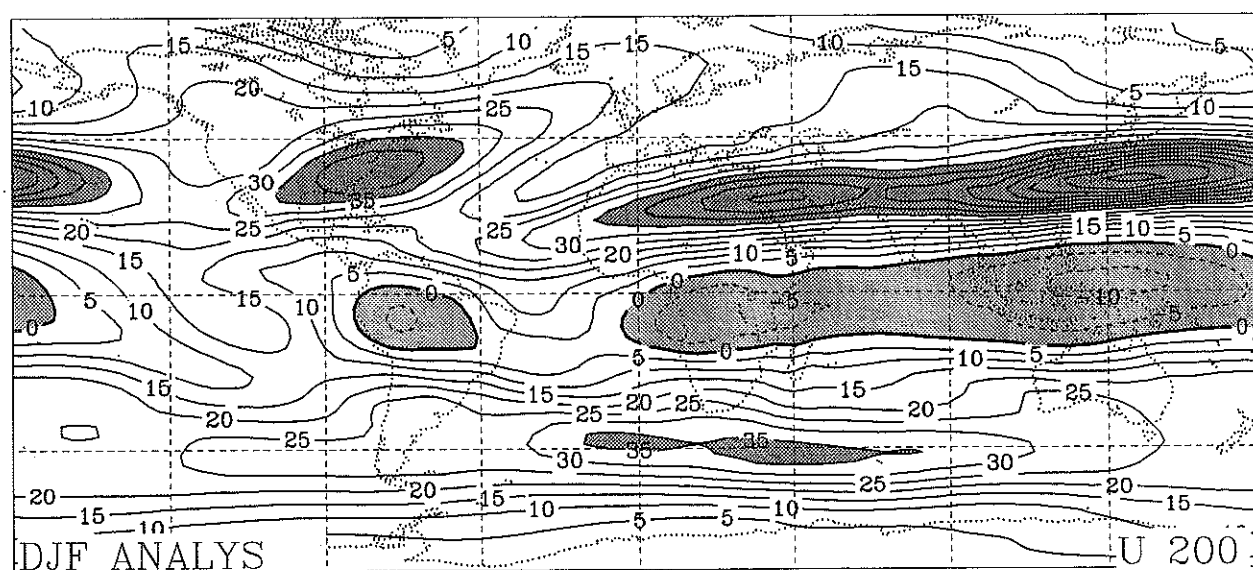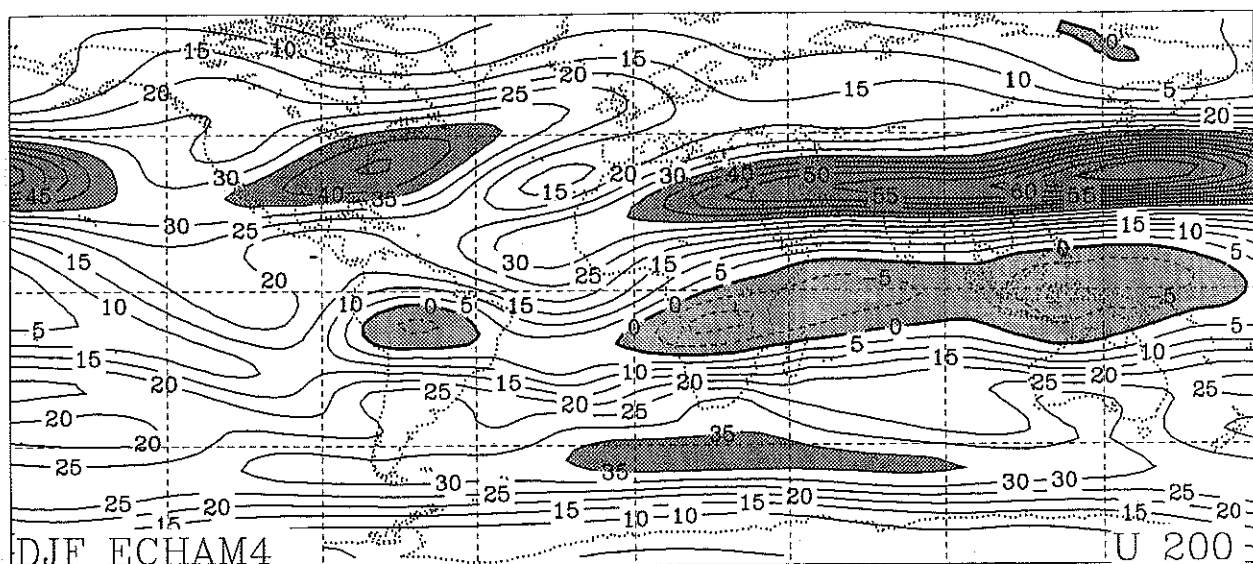
Figure 7   Maps of ECHAM-4 simulated (top) and ECMWF analysed (middle) zonal wind at 200 hPa for the DJF season. Contour spacing is 5 m/s. Areas with large westerlies (> 35 m/s) and easterlies (< 0 m/s) are shaded. In the error field (bottom) the spacing is ± 1, 2, 4, 6, 8, 10 m/s. In shaded areas the zonal wind errors exceed 4 m/s (light: westerly bias; dark: easterly bias).

67
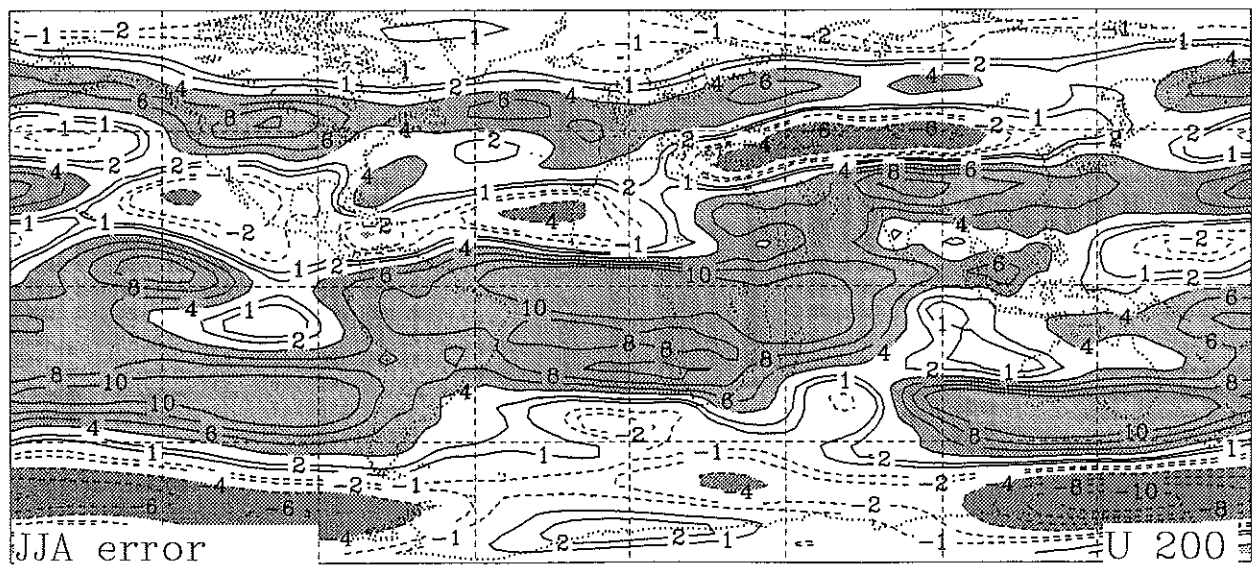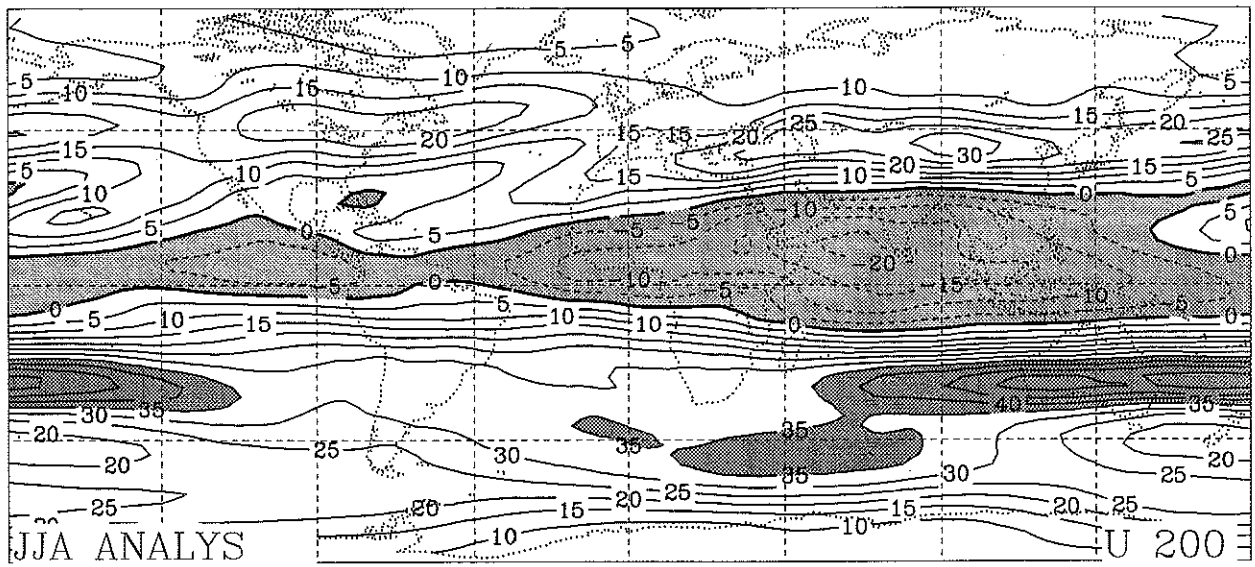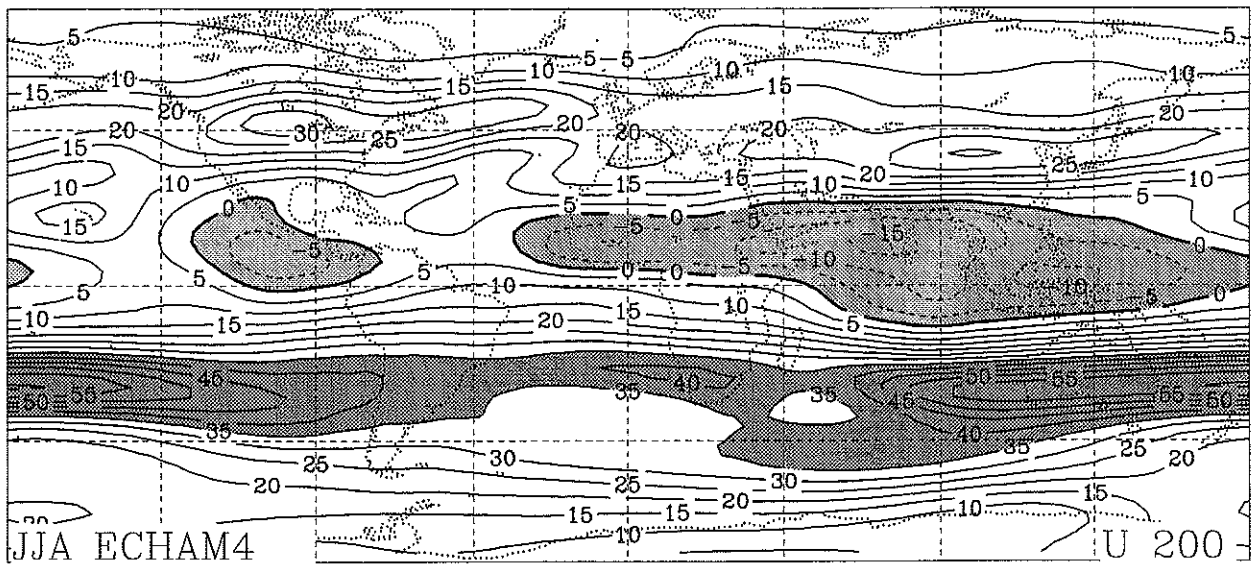
Figure 8   As in Fig. 7 except for the JJA season.
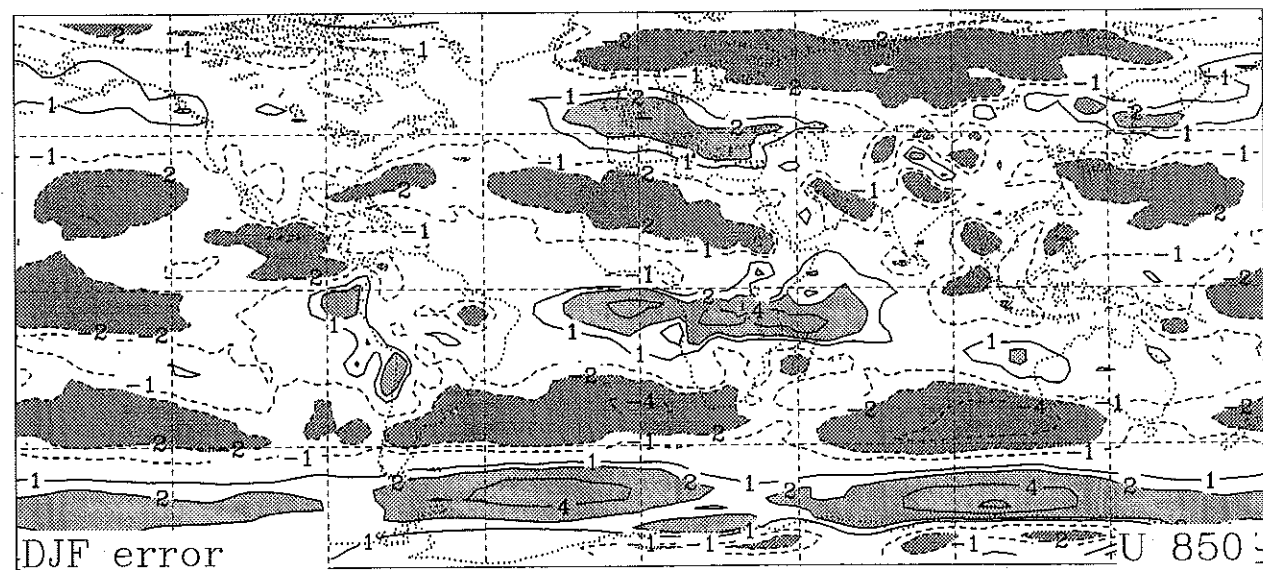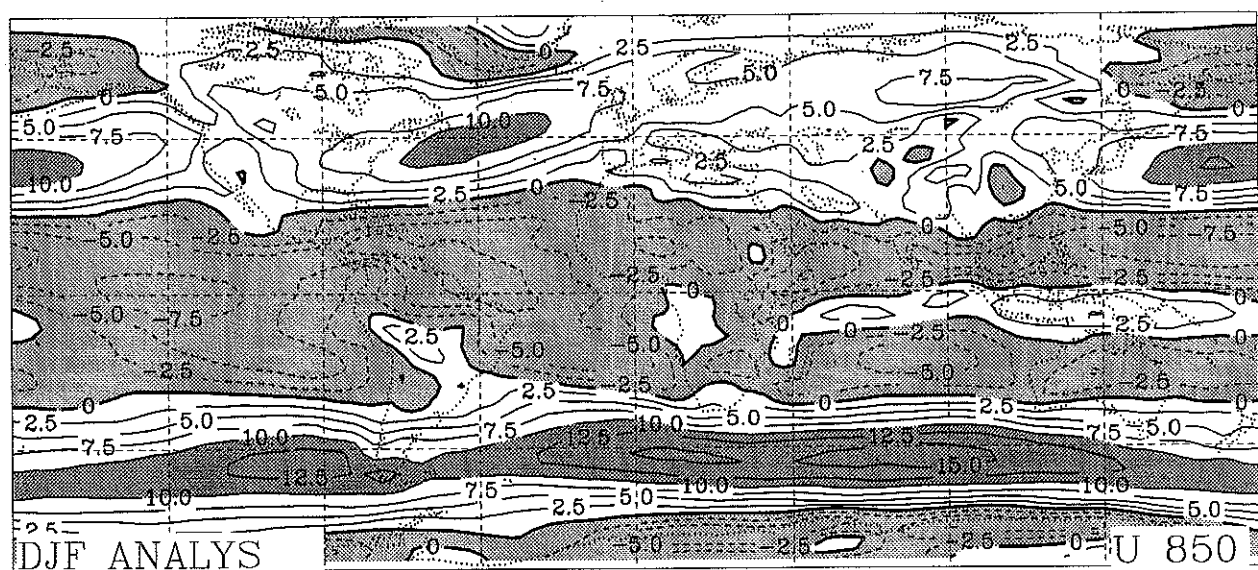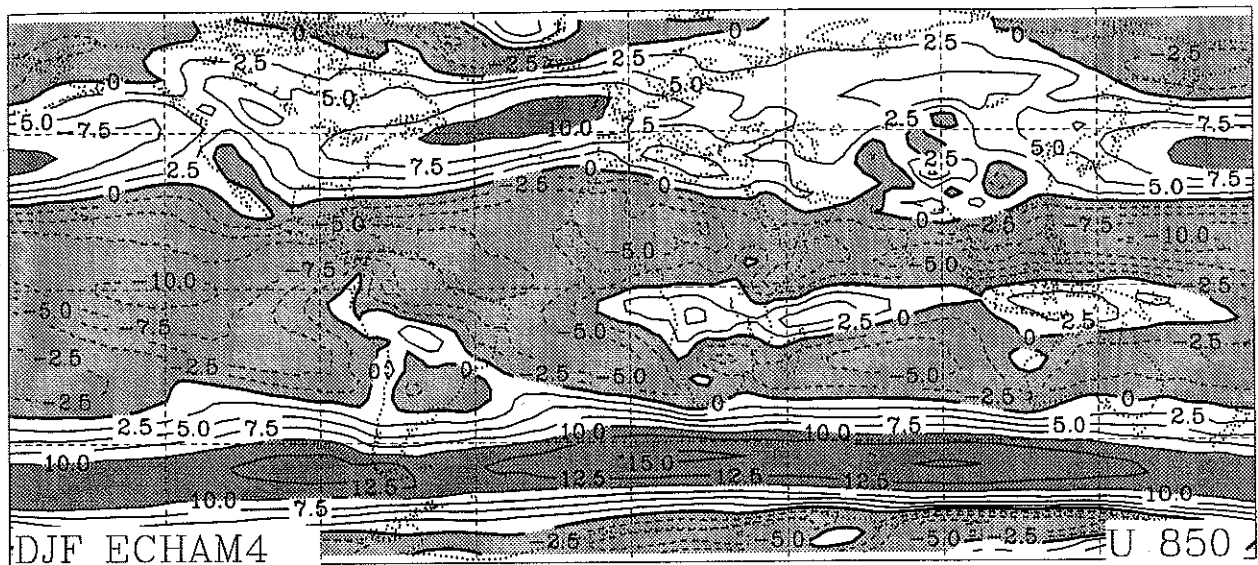
Figure 9   Maps of ECHAM-4 simulated (top) and ECMWF analysed (middle) zonal wind at 850
hPa for the DJF season. Contour spacing is 2.5 m/s. Areas with large westerlies (> 10
m/s) and large easterlies (≤ -5 m/s) are shaded. In the error field (bottom) the spacing
is ± 1, 2, 4, 6 m/s. In shaded areas the zonal wind errors exceed 2 m/s (light: westerly
bias; dark: easterly bias).

69
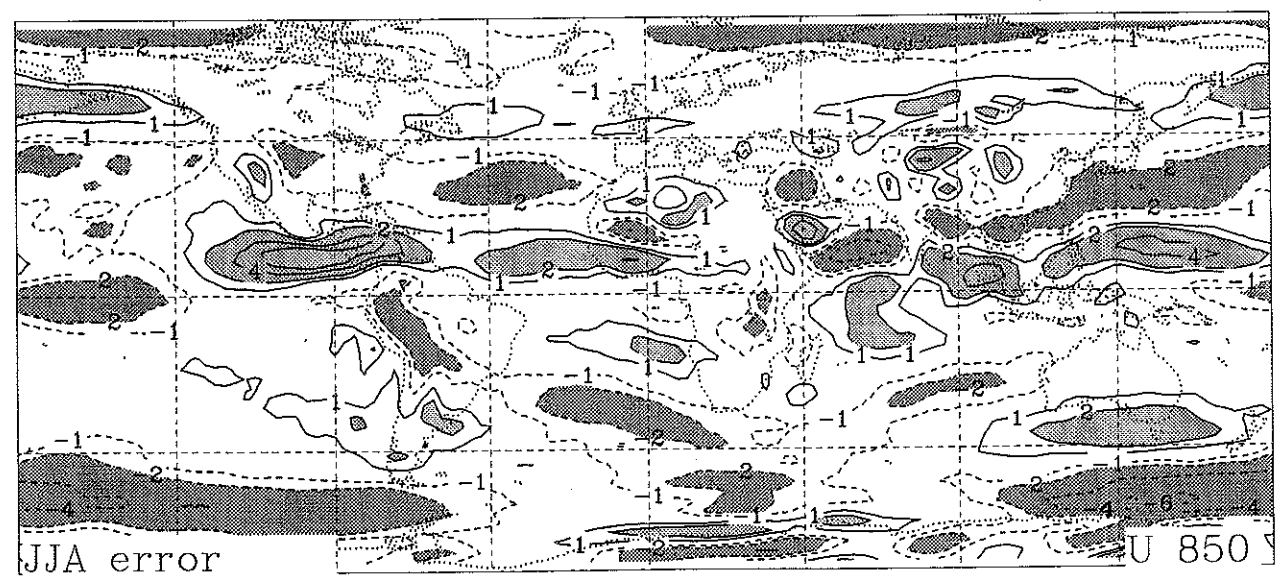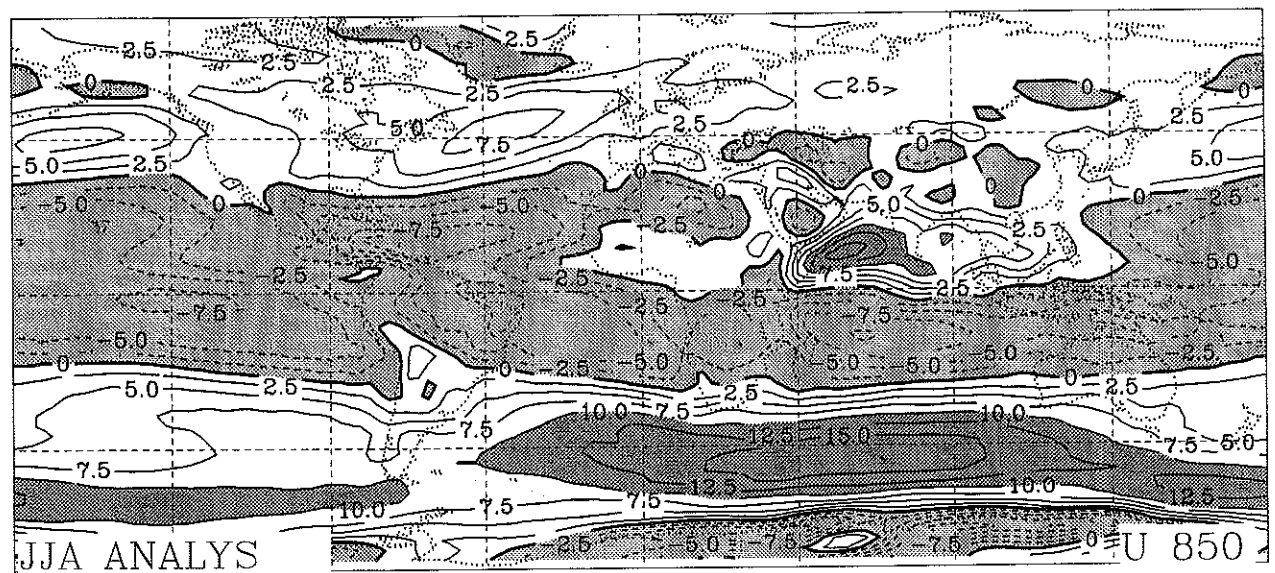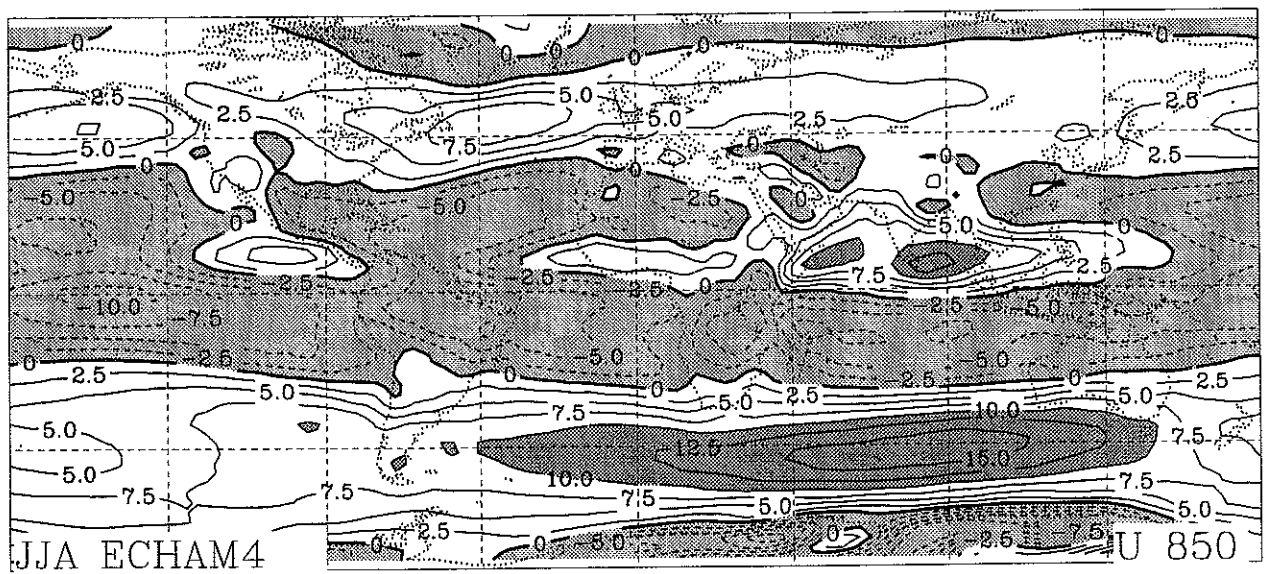
Figure 10   As in Fig. 9 except for the JJA season.
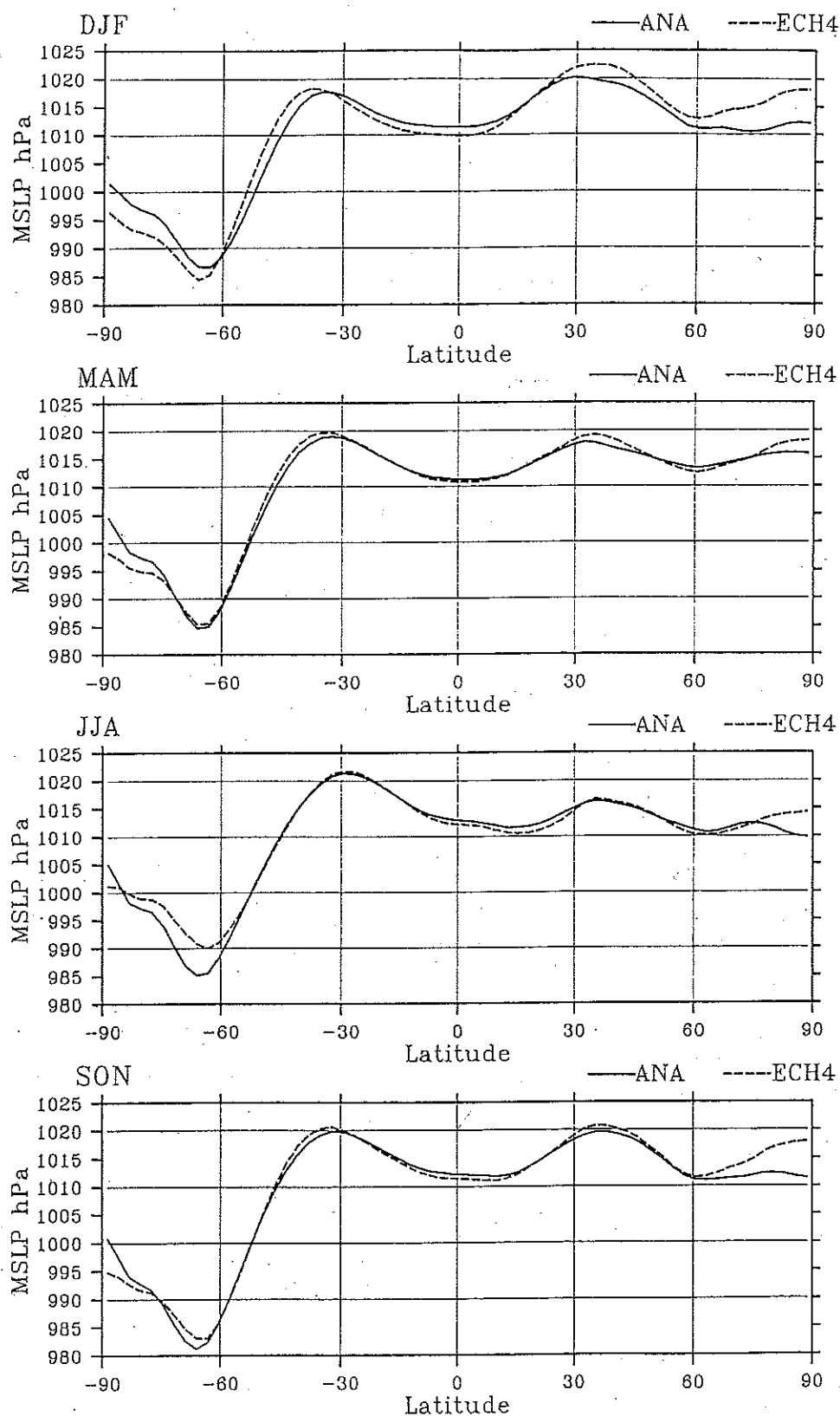
Figure 11   Meridional distribution of zonally and seasonally averaged mean sea level pressure (hPa) in the ECHAM-4 simulation (dashed curves) and ECMWF analysis (solid curves).

71
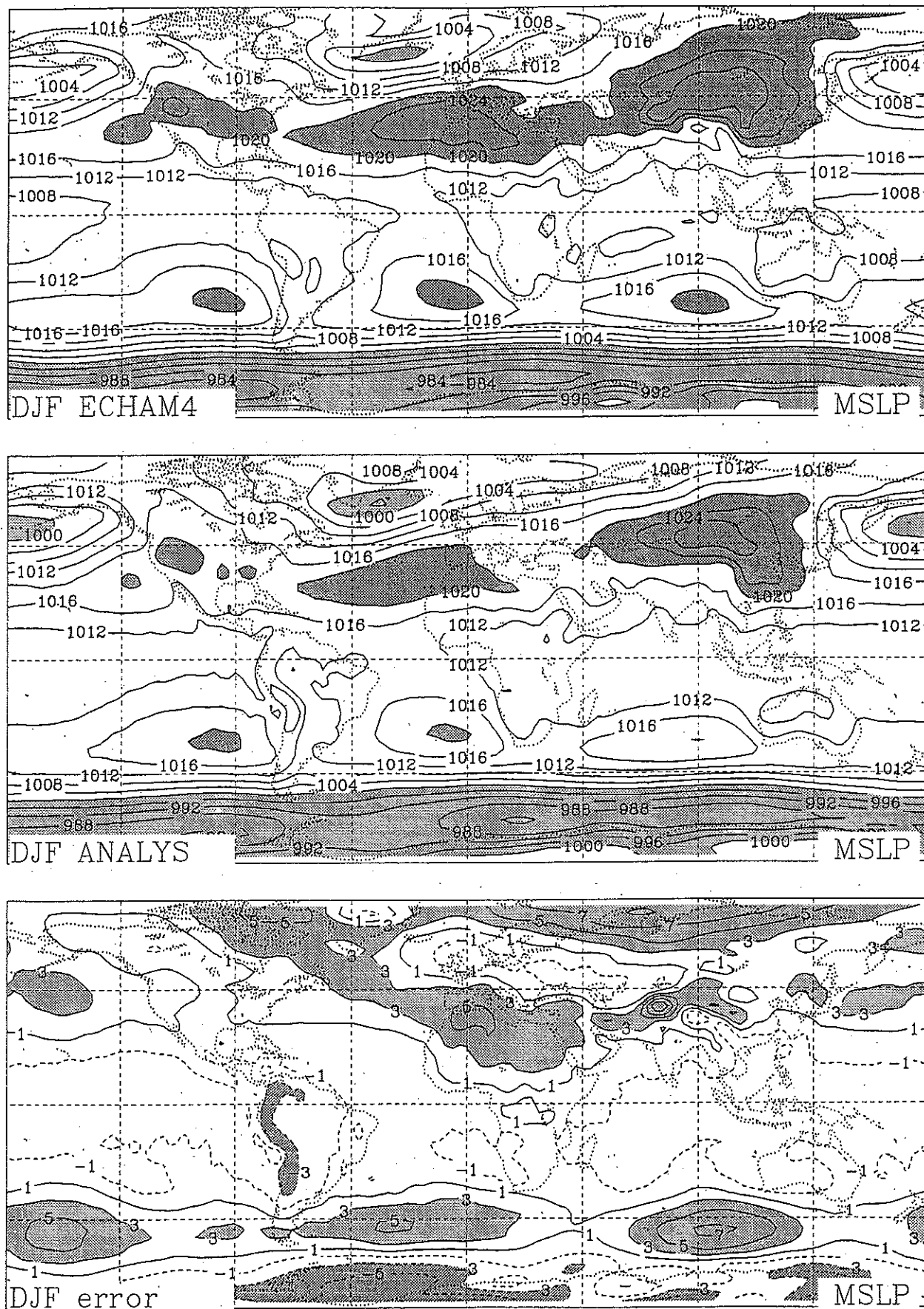
Figure 12   Maps of ECHAM-4 simulated (top) and ECMWF analysed (middle) sea level pressure
for the DJF season. Contour spacing is 4 hPa. High-pressure areas (> 1020 hPa) and
low-pressure areas (< 1000 hPa) are shaded. In the error field (bottom) the spacing is
± 1, 3, 5, 7, 9 hPa. In shaded areas the errors exceed ± 3 hPa (light: positive bias; dark:
negative bias).

72
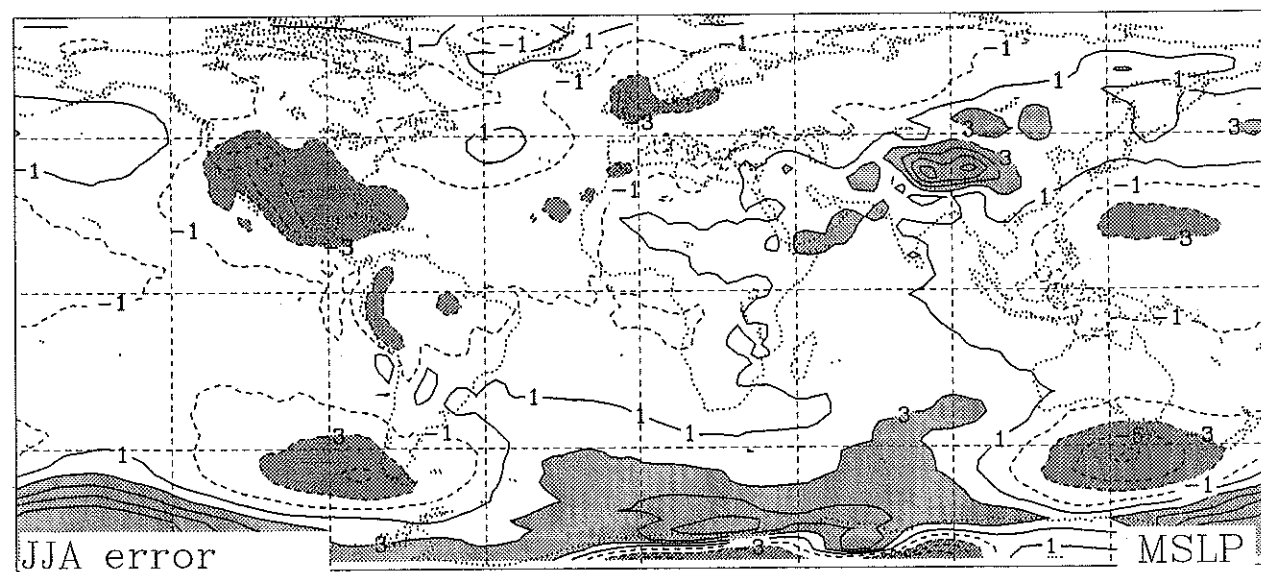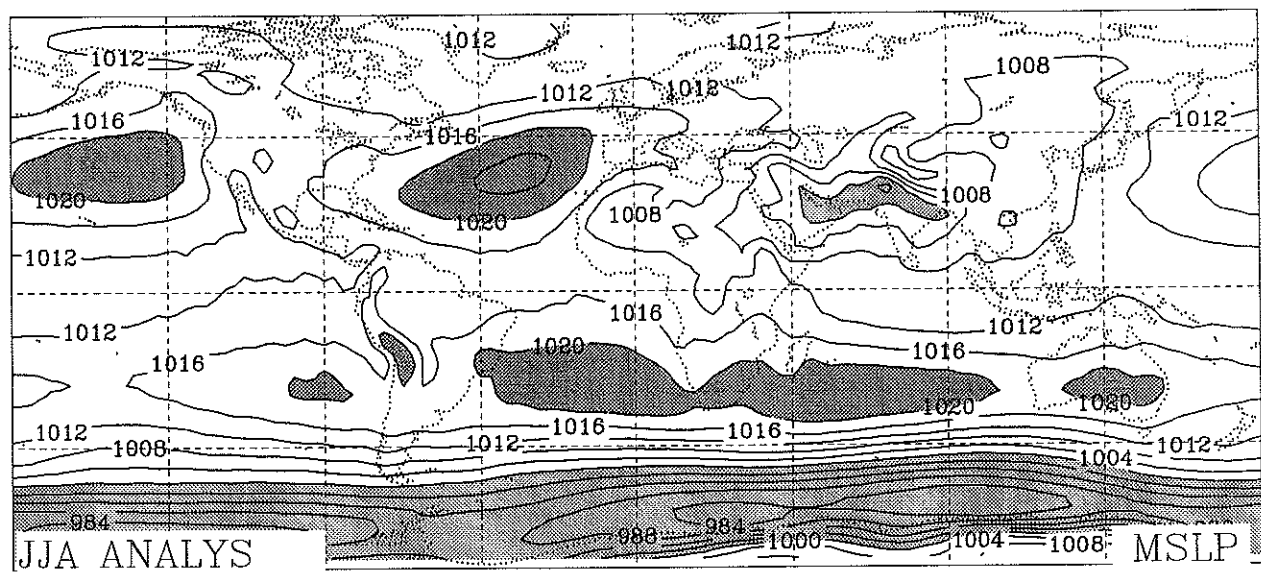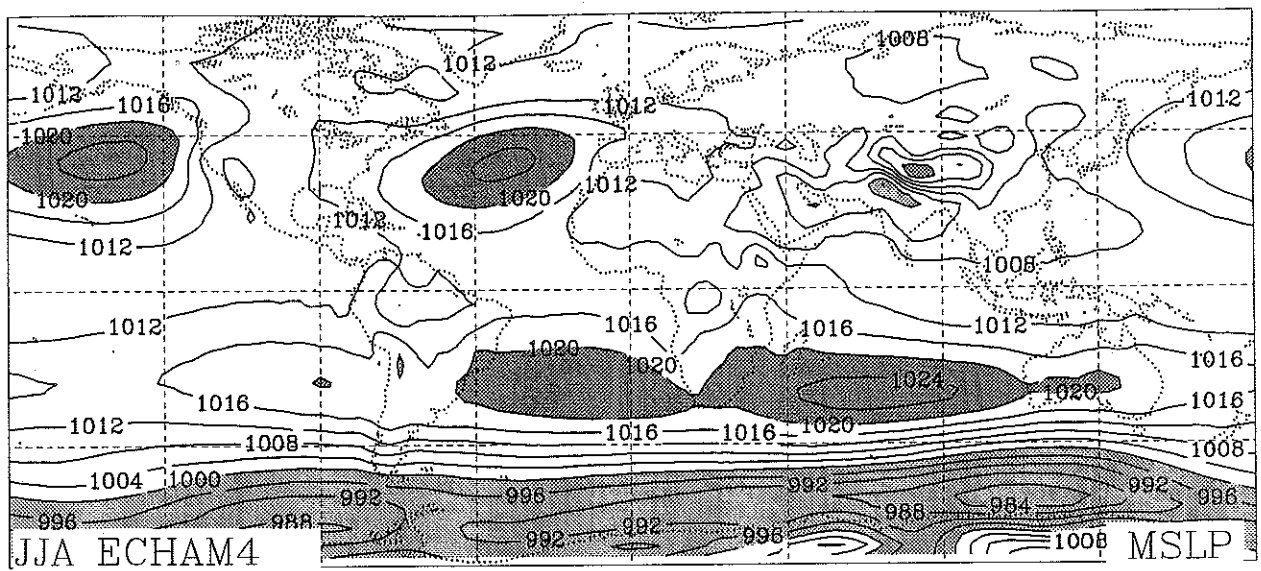
Figure 13　As in Fig. 12 except for the JJA season.
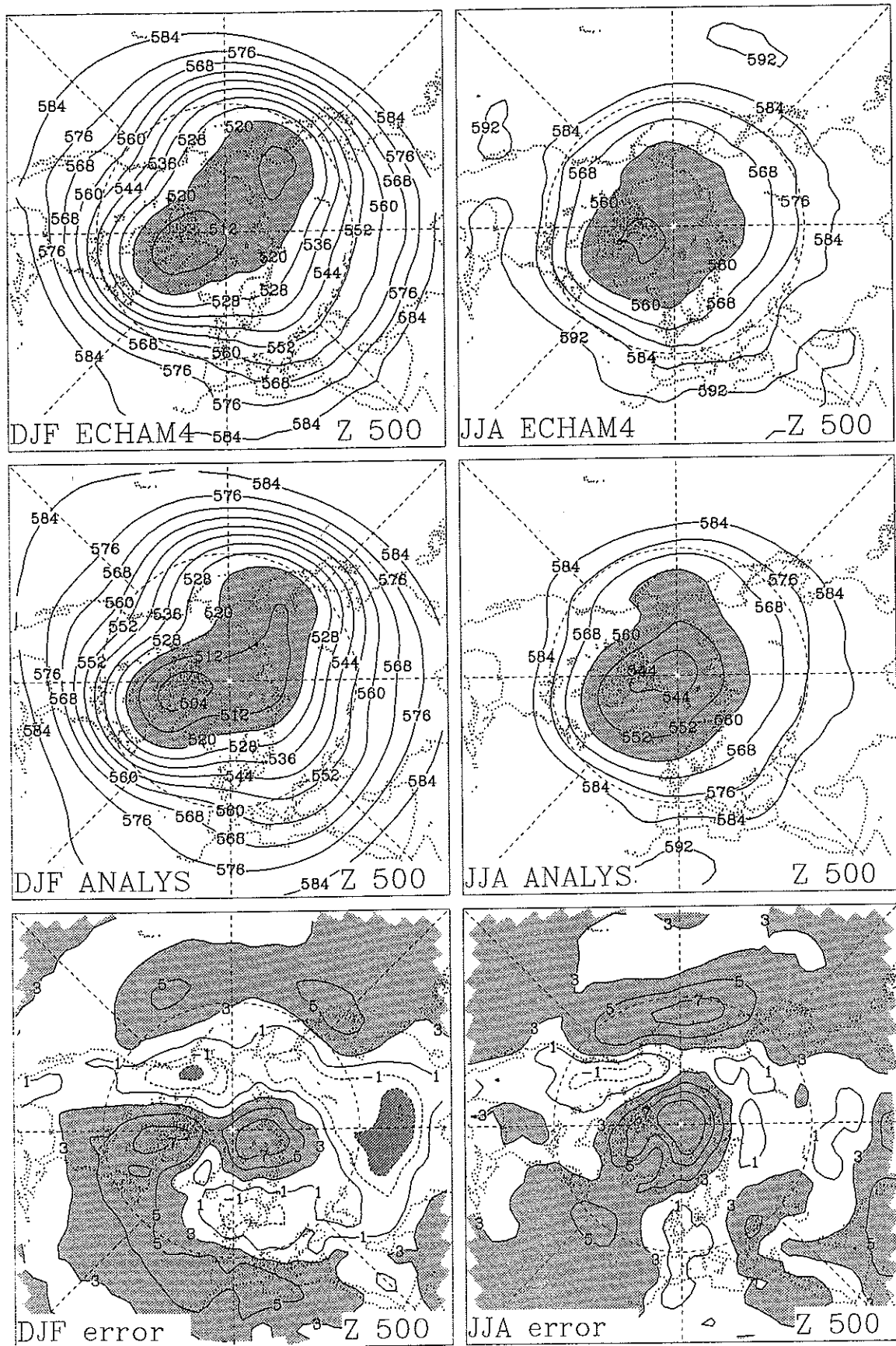
Figure 14   Maps of ECHAM-4 simulated (top) and ECMWF analysed (middle) 500 hPa geopotential height in the Northern Hemisphere for DJF (left) and JJA (right), respectively. Contour spacing is 8 dm. Bottom: Error maps with ± 1, 3, 5, 7, 9 dm spacing. In shaded areas the errors exceed ± 3 dm (light: positive bias; dark: negative bias).

74
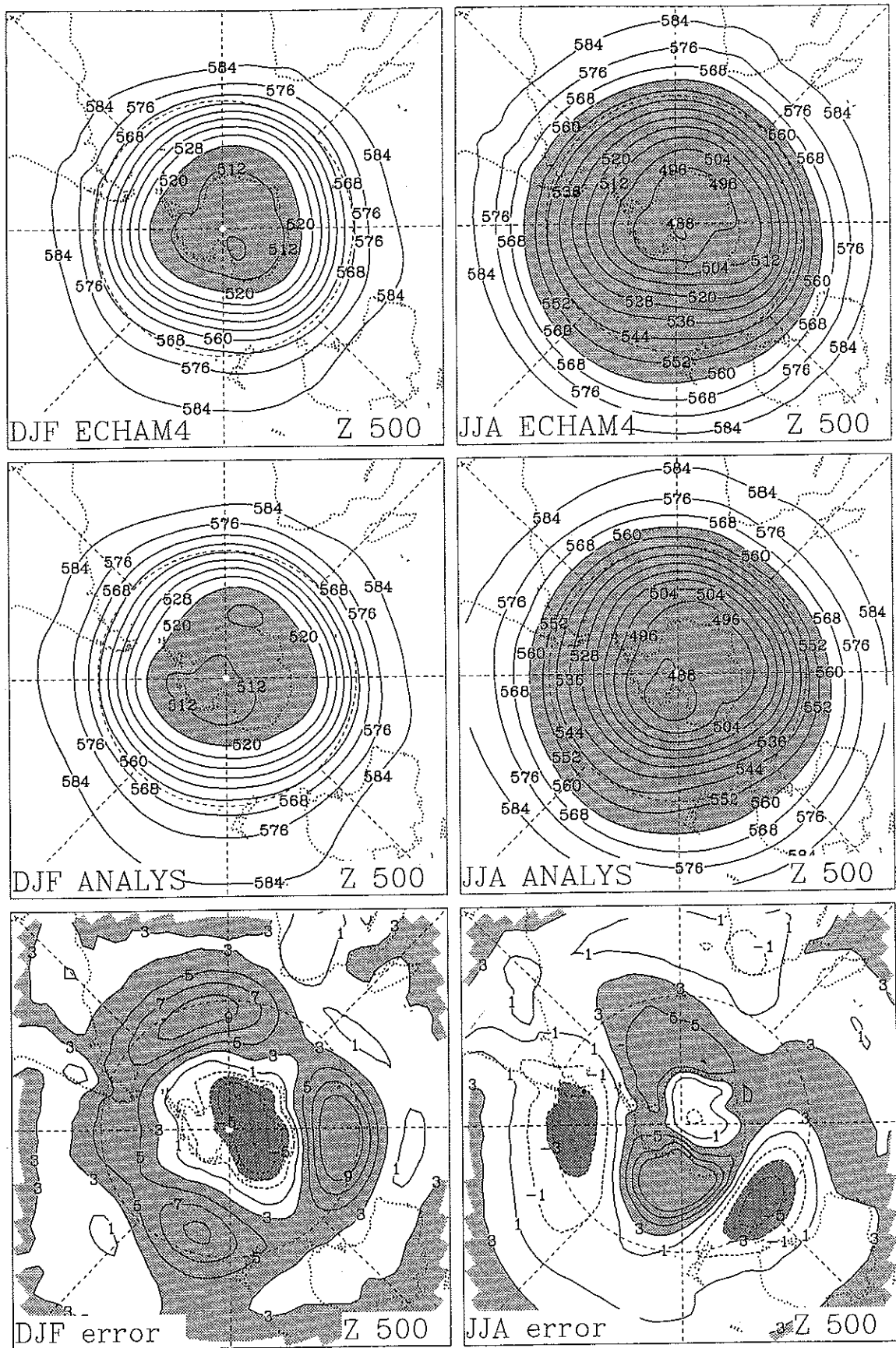
Figure 15   As in Fig. 14 except for the Southern Hemisphere.
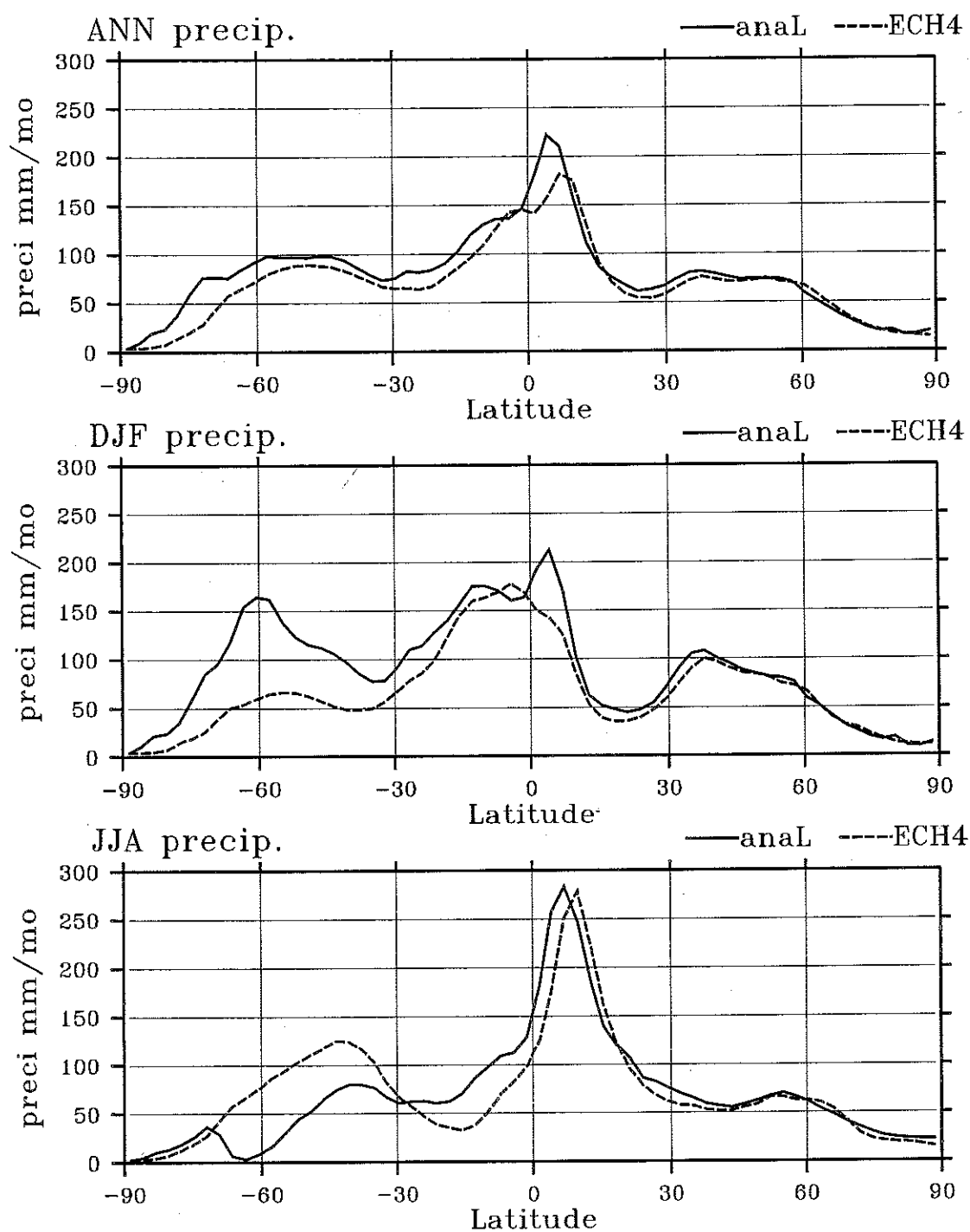
Figure 16   Meridional distribution of zonal means of ECHAM-4 simulated precipitation (dashed
curves) and analysed precipitation (solid curves; Legates and Willmott, 1990). Units
are mm/month.

ANN precip. land
anaL ----ECH4

DJF precip. land
anaL ----ECH4

JJA precip. land
anaL ----ECH4
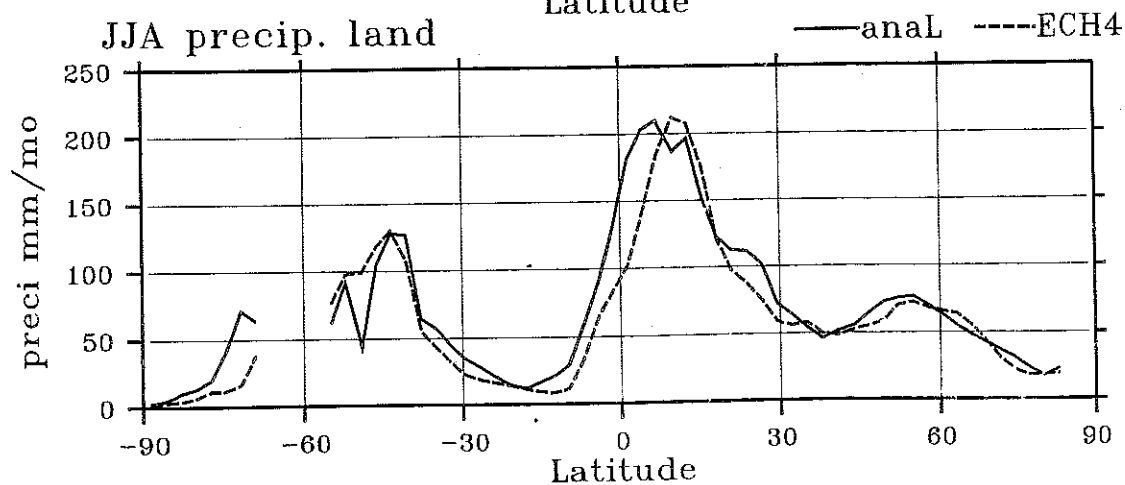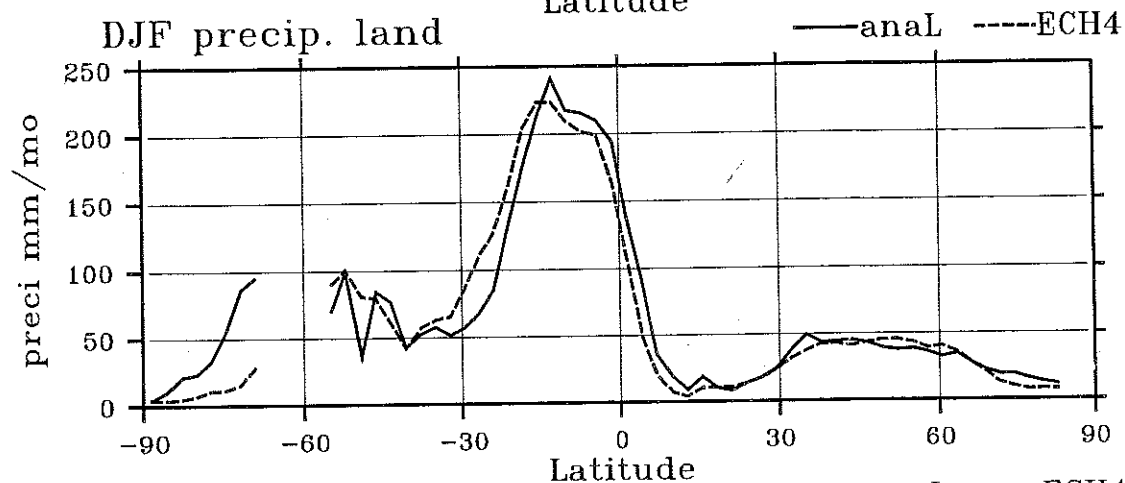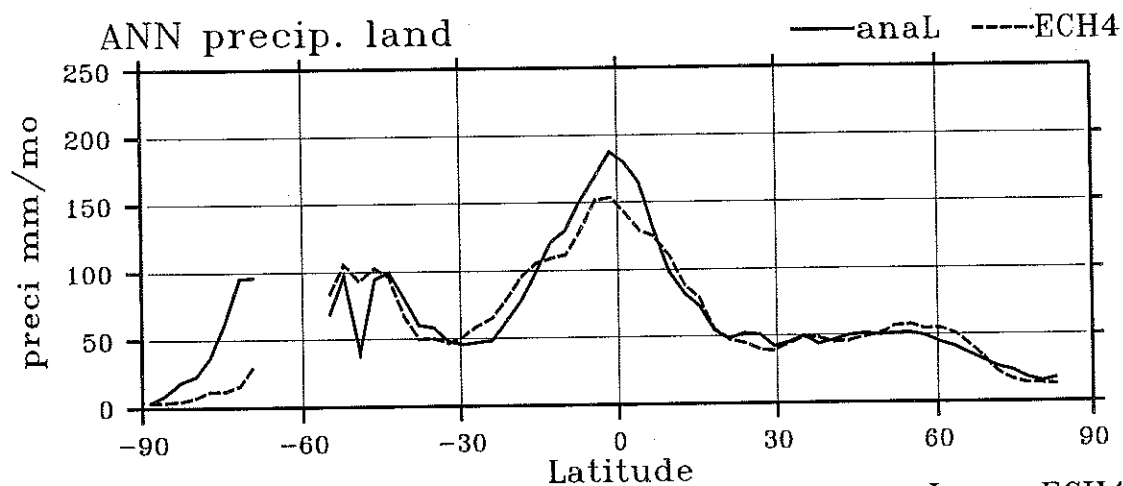
Figure 17   As in Fig. 16 except for land areas.
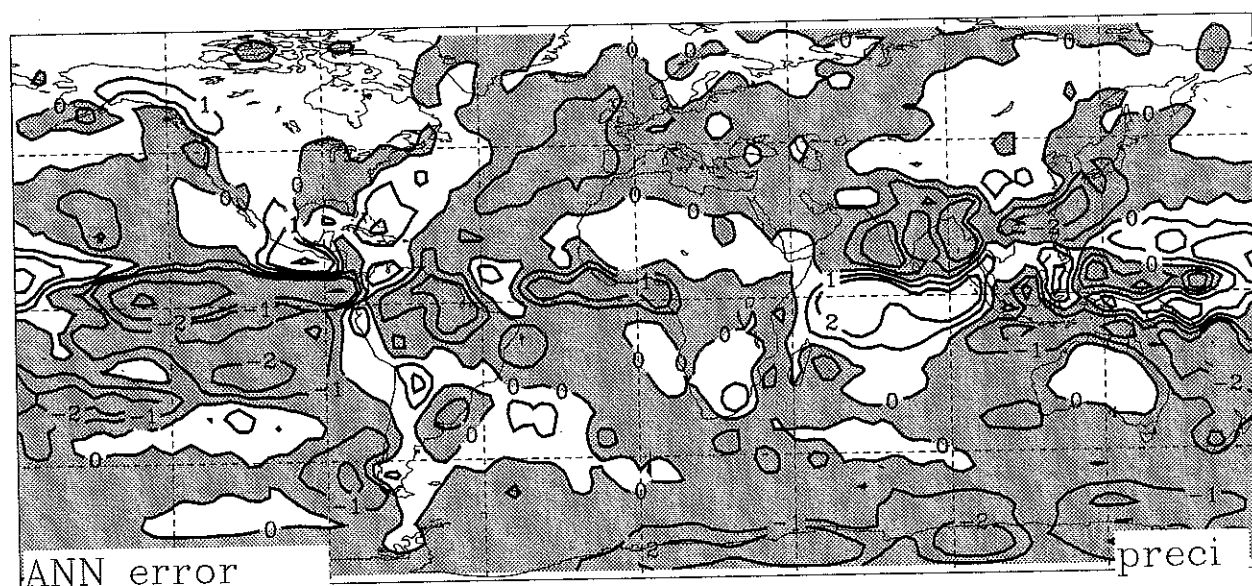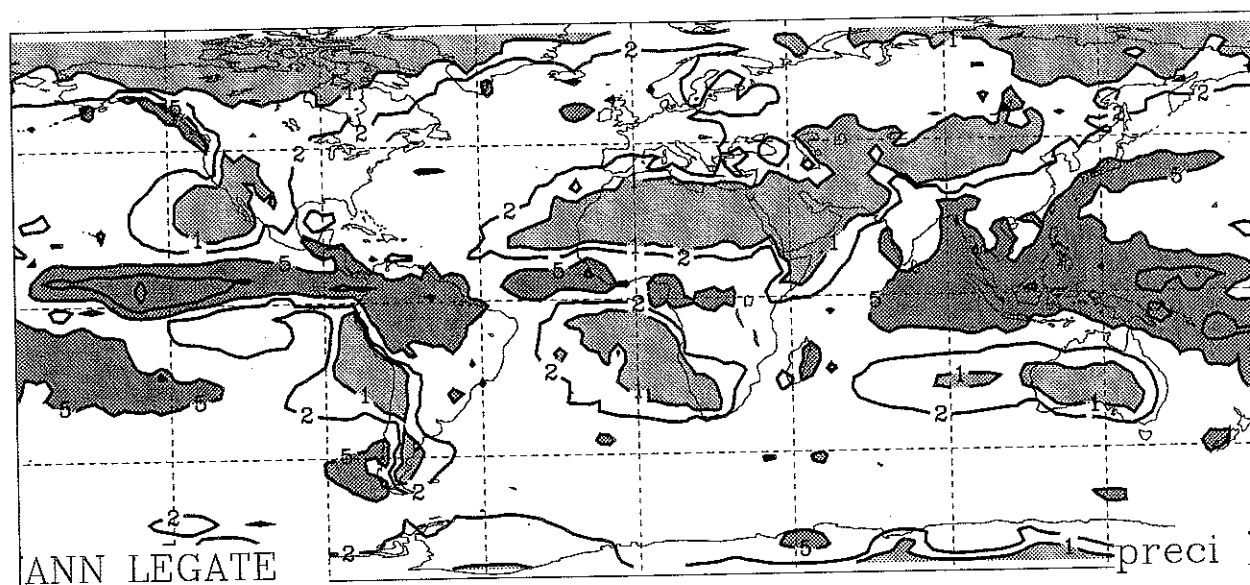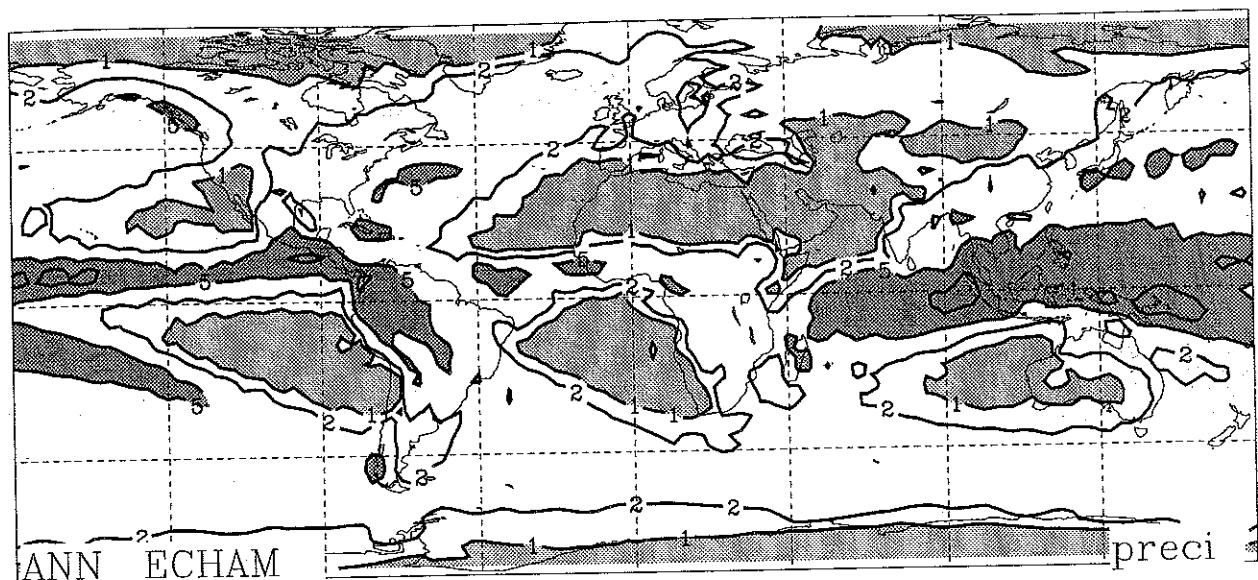
Figure 18   Annual mean precipitation according to ECHAM-4 simulation (top) and analysed
climatology (middle panel; Legates and Willmott, 1990). Contour spacing is 1, 2, 5,
10, 15, 20 mm/d. Light (dark) shading indicates areas with P<1 (P>5) mm/d,
respectively. The contour spacing in the error map (bottom) is ± 1, 2, 5, 10 mm/d.
In shaded areas the simulated precipitation is less than observed.

78

DJF ECHAM4   preci

DJF LEGATE   preci

DJF error   preci
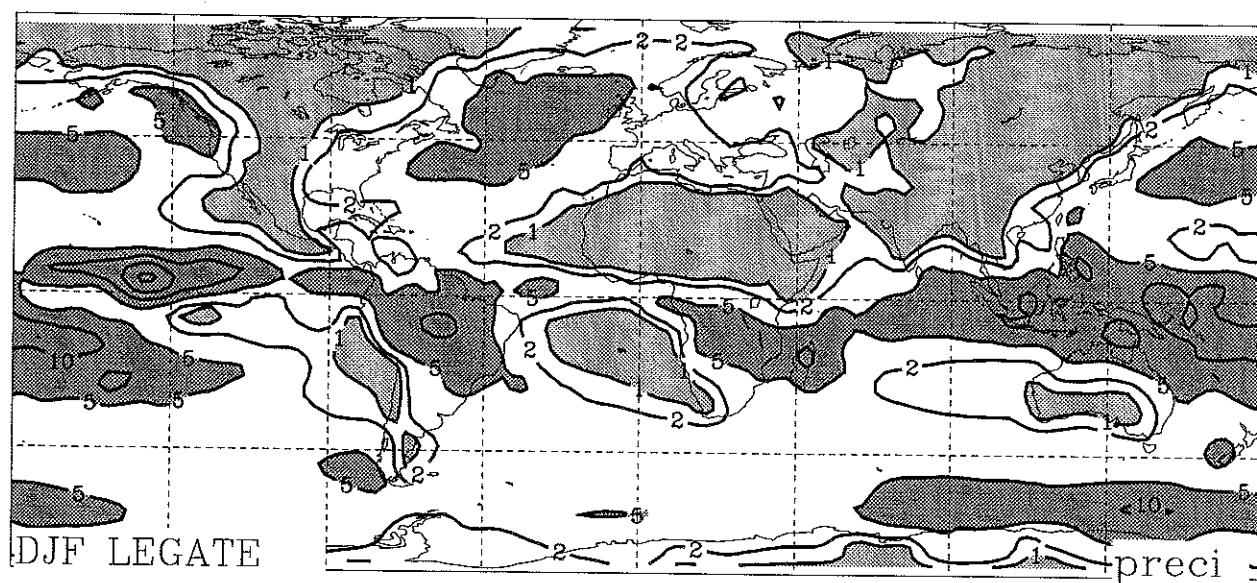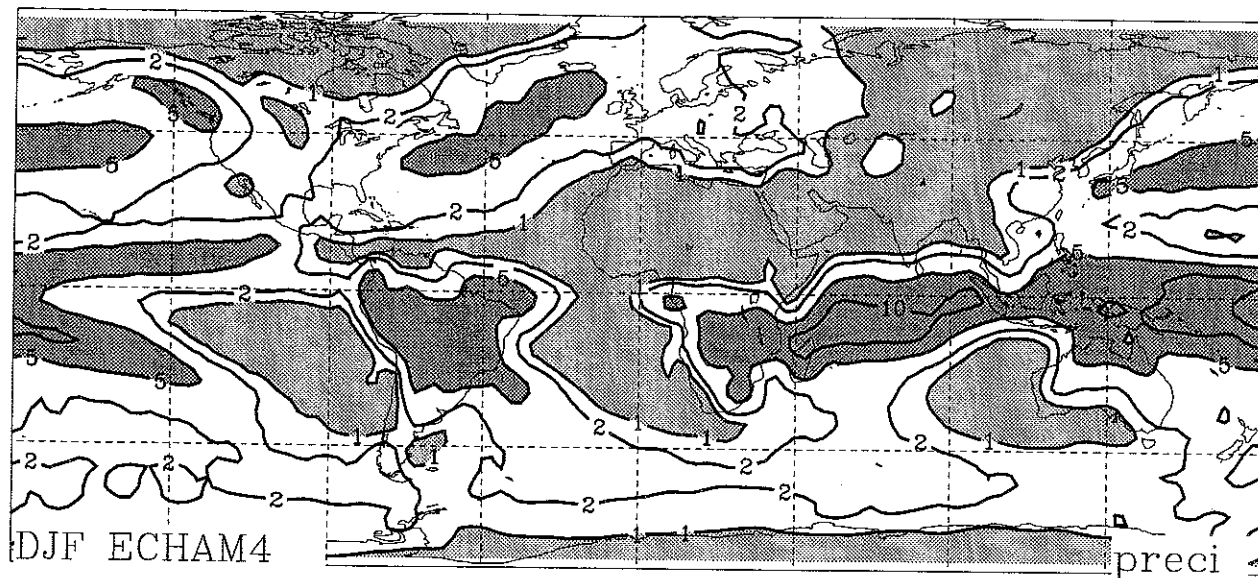
Figure 19   As in Fig. 18 except for DJF precipitation.

79
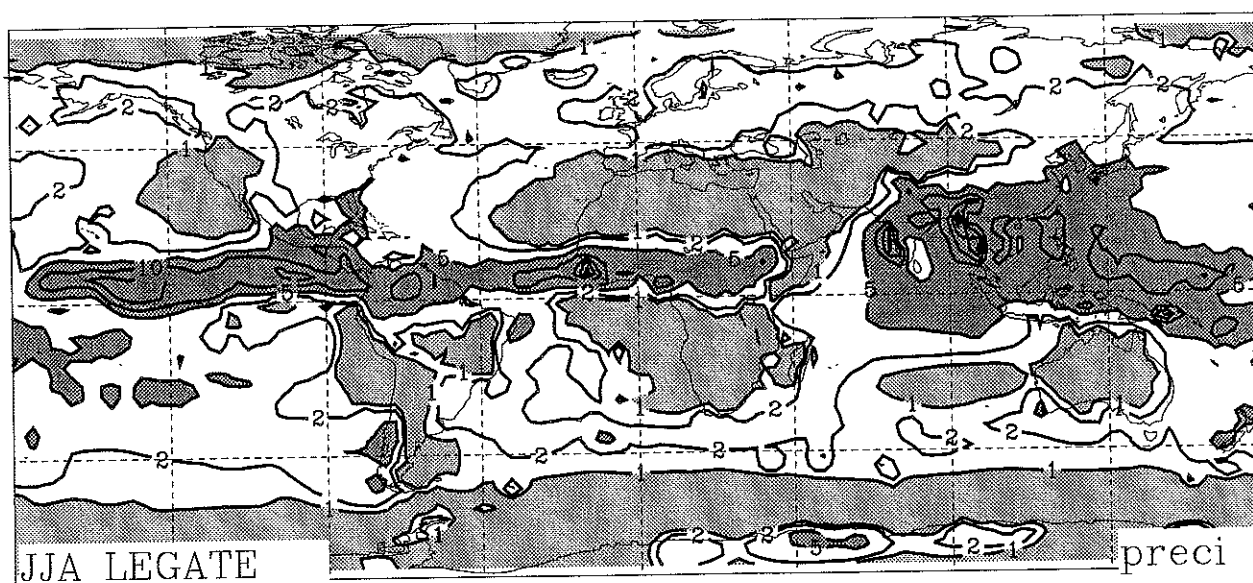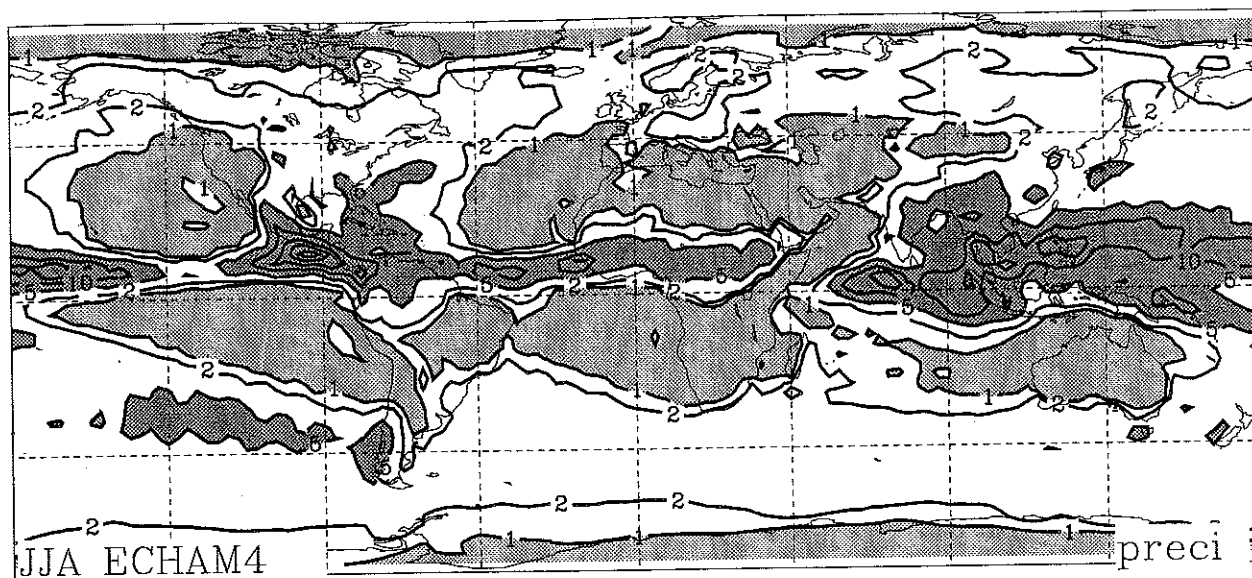
Figure 20   As in Fig. 18 except for JJA precipitation.
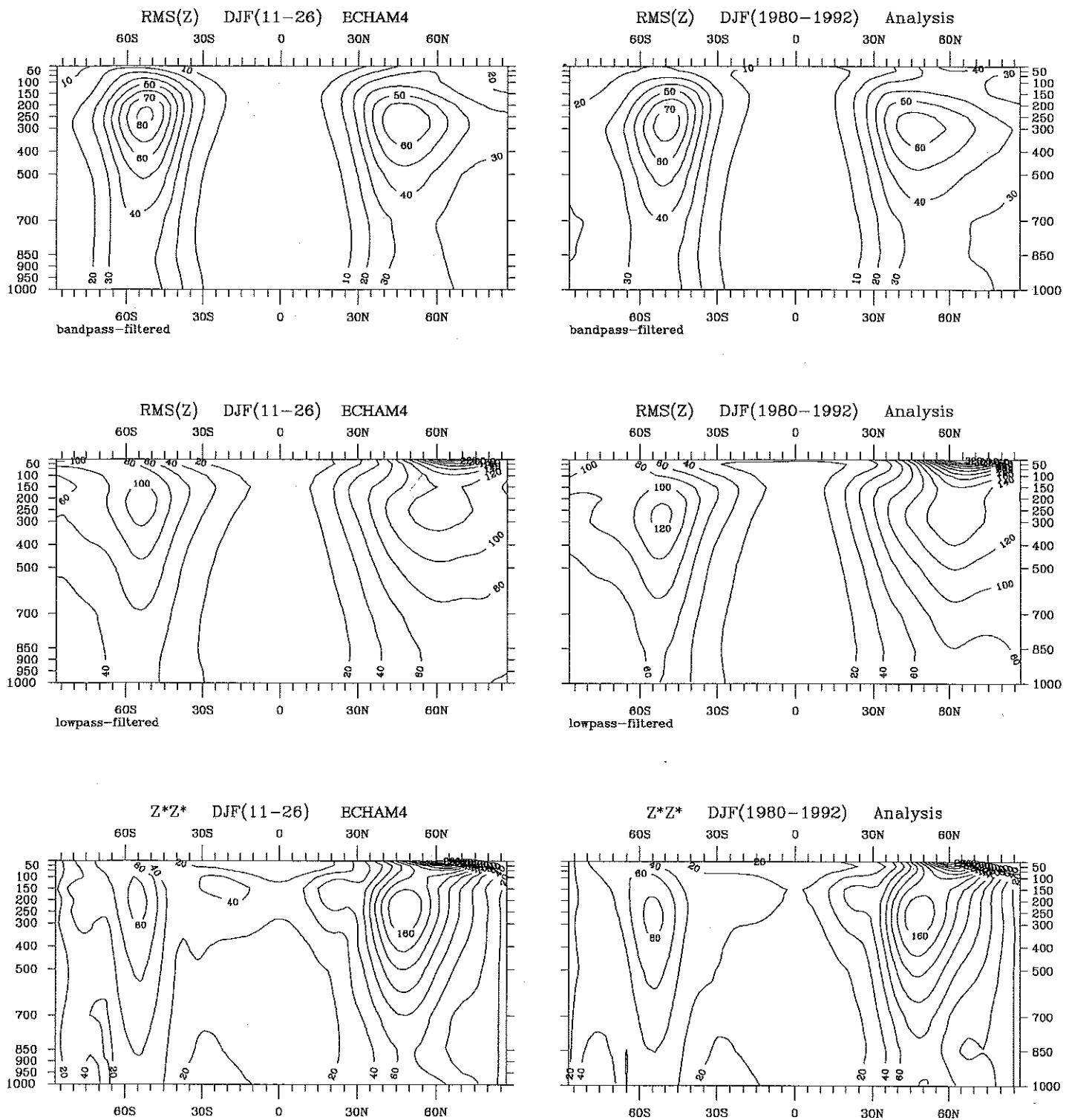
Figure 21 Latitude-height (pressure in hPa) distributions of zonal mean standard deviation of geopotential height (m) due to transient eddies (top: bandpass regime; middle: lowpass regime) and stationary eddies (bottom), respectively.
Left: ECHAM-4 (mean of two realizations). Right: ECMWF analysis (1980-1992).

RMS(Z) (1000 hPa) DJF(11-26) ECHAM4
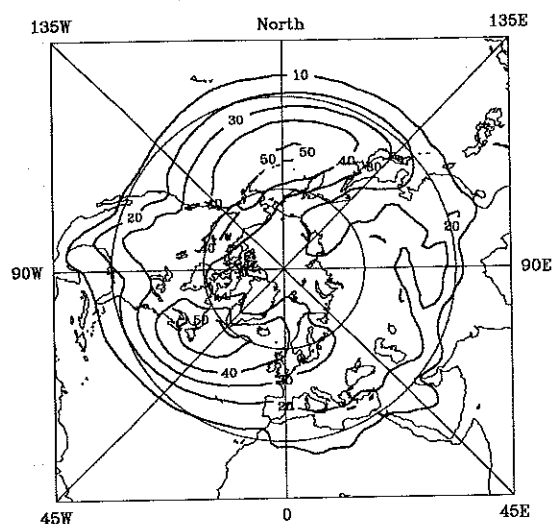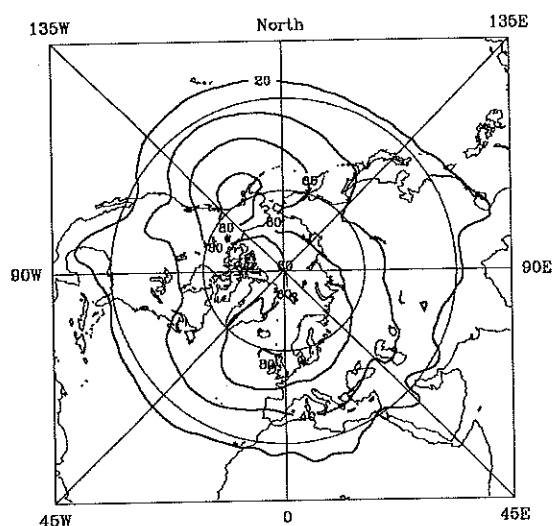
bandpass—filtered

RMS(Z) (1000 hPa) DJF(1980-1992) Analysis

bandpass—filtered

RMS(Z) (1000 hPa) DJF(11-26) ECHAM4
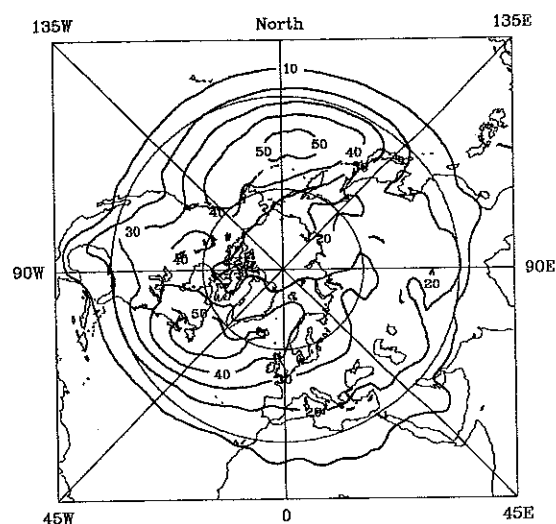
lowpass—filtered

RMS(Z) (1000 hPa) DJF(1980-1992) Analysis
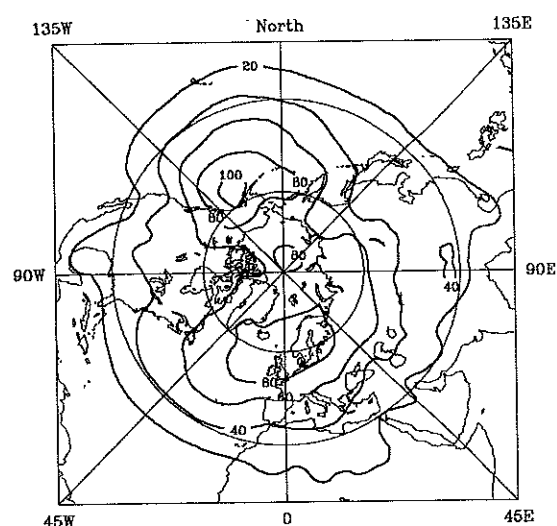
lowpass—filtered

Figure 22   Standard deviation of 1000 hPa geopotential height (m) due to transient eddies in the
bandpass regime (top) and lowpass regime (bottom), respectively.
Left: ECHAM-4 (mean of two realizations). Right: ECMWF analysis (1980-1992).

RMS(Z) (500 hPa)   DJF(11−26) ECHAM4
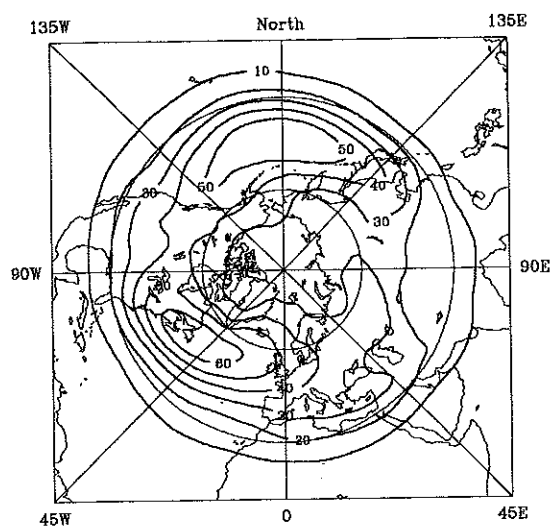
bandpass−filtered

RMS(Z) (500 hPa)   DJF(1980−1992) Analysis
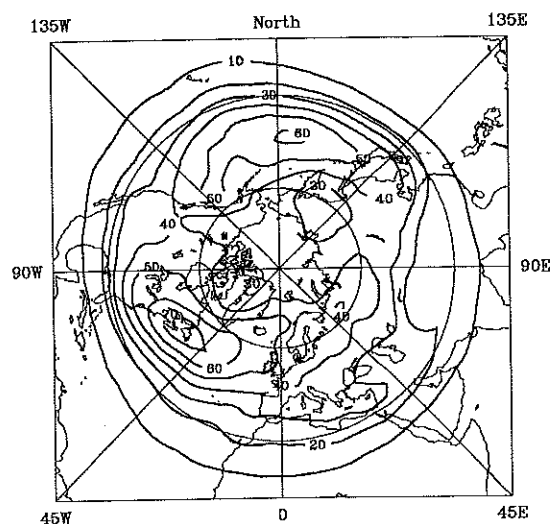
bandpass−filtered

RMS(Z) (500 hPa)   DJF(11−26) ECHÁM4
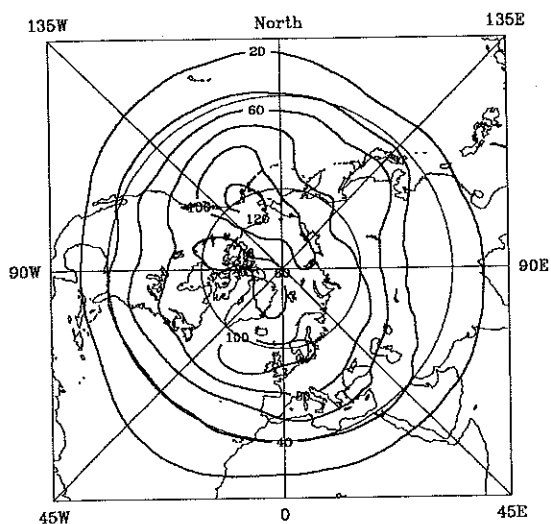
lowpass−filtered

RMS(Z) (500 hPa)   DJF(1980−1992) Analysis
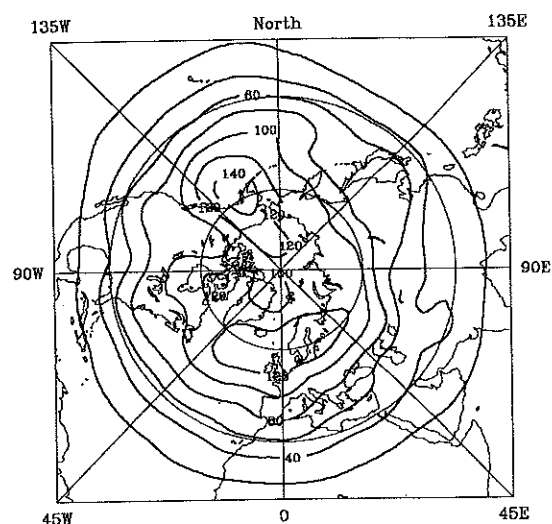
lowpass−filtered

Figure 23   As in Fig. 22 except for 500 hPa.

83

σ(Z) (1000 hPa) DJF (11-26) ECHAM4 (a)

σ(Z) (500 hPa) DJF (11-26) ECHAM4 (a)

σ(Z) (1000 hPa) DJF (11-26) ECHAM4 (b)

σ(Z) (500 hPa) DJF (11-26) ECHAM4 (b)

σ(Z) (1000 hPa) DJF (1980-1992) Analysis

σ(Z) (500 hPa) DJF (1980-1992) Analysis
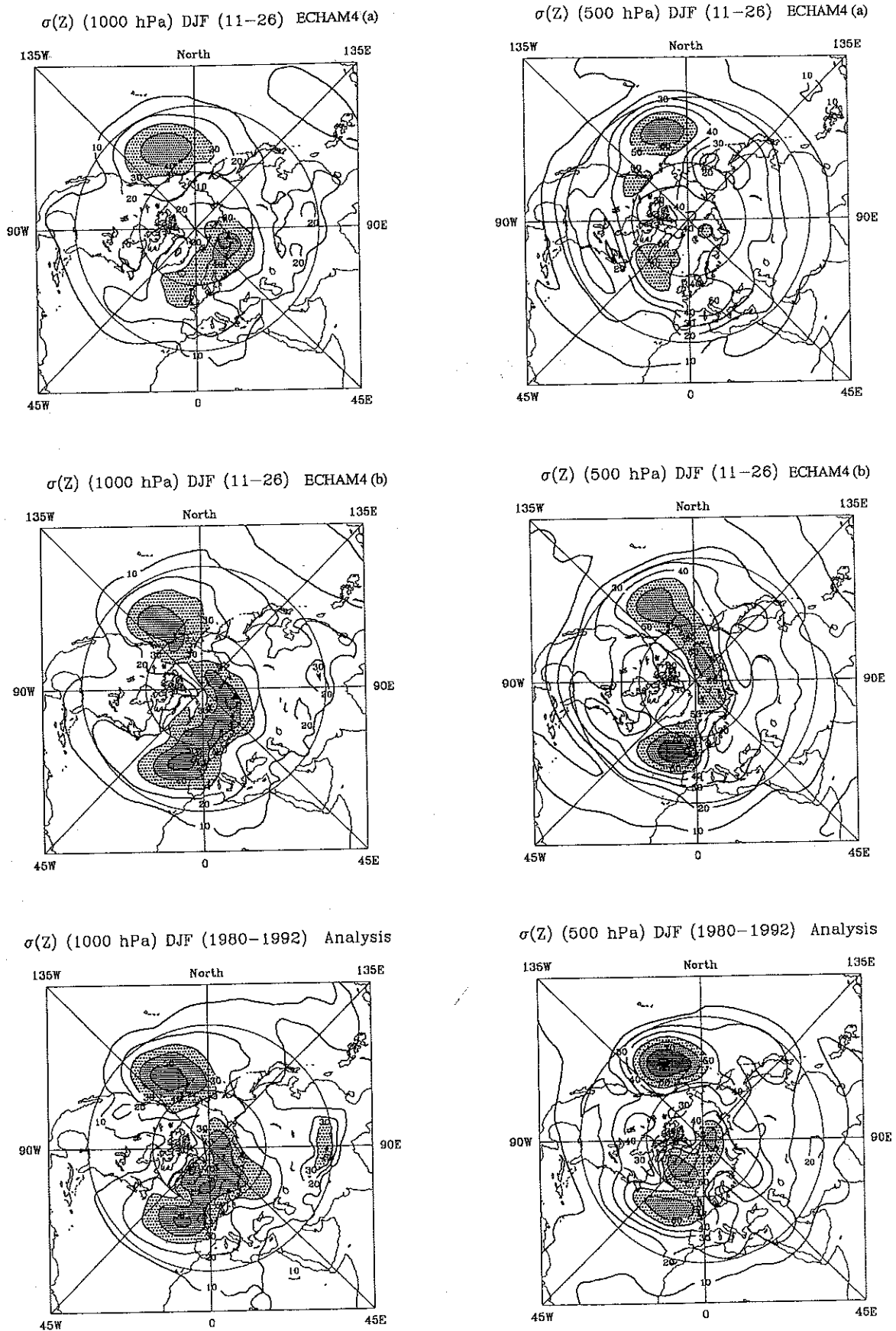
Figure 24   'Interannual' standard deviation of seasonal mean geopotential height (m) at 1000 hPa (left) and 500 hPa (right), respectively, for two model realizations (top and middle) and ECMWF analysis (bottom).
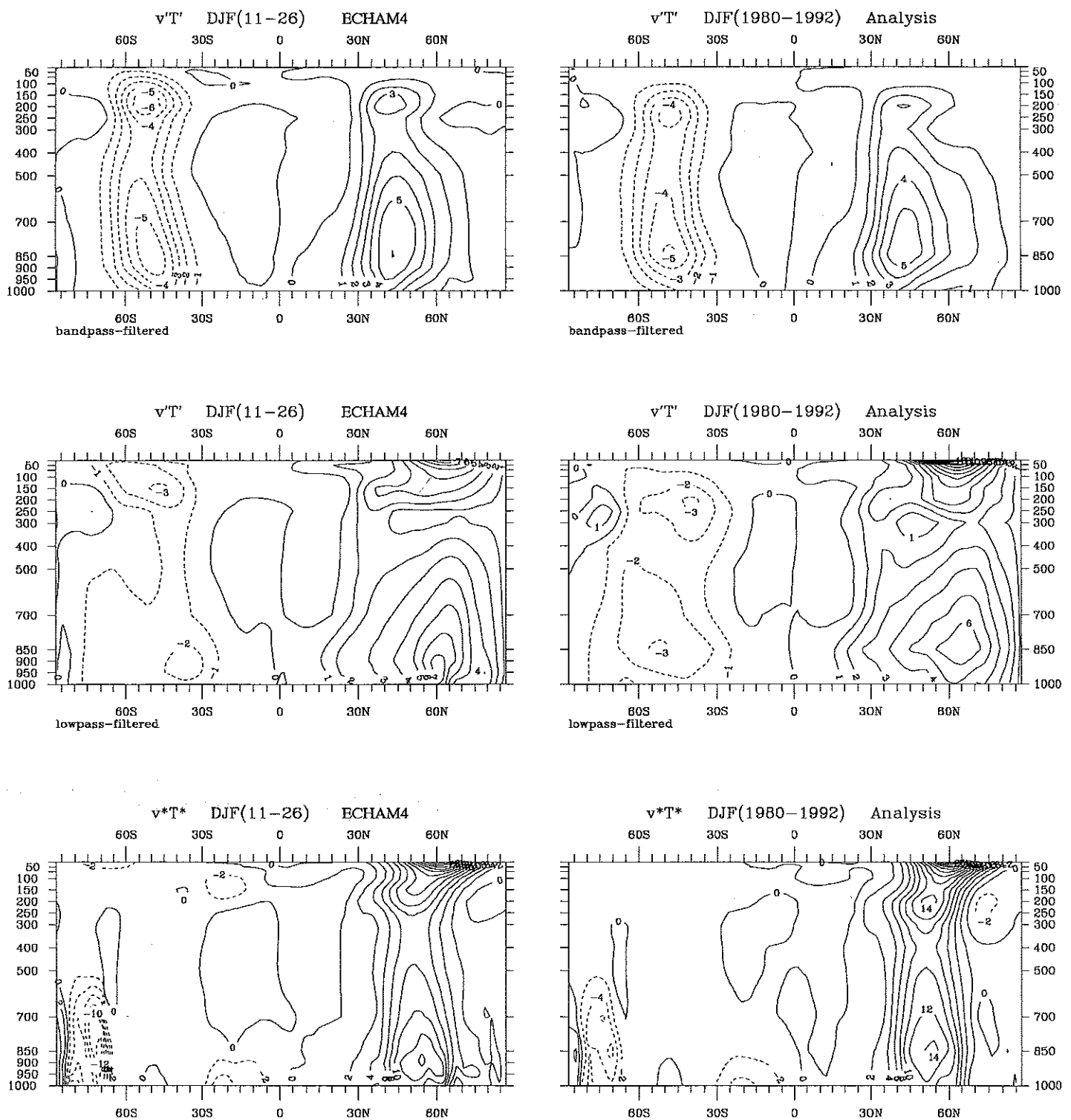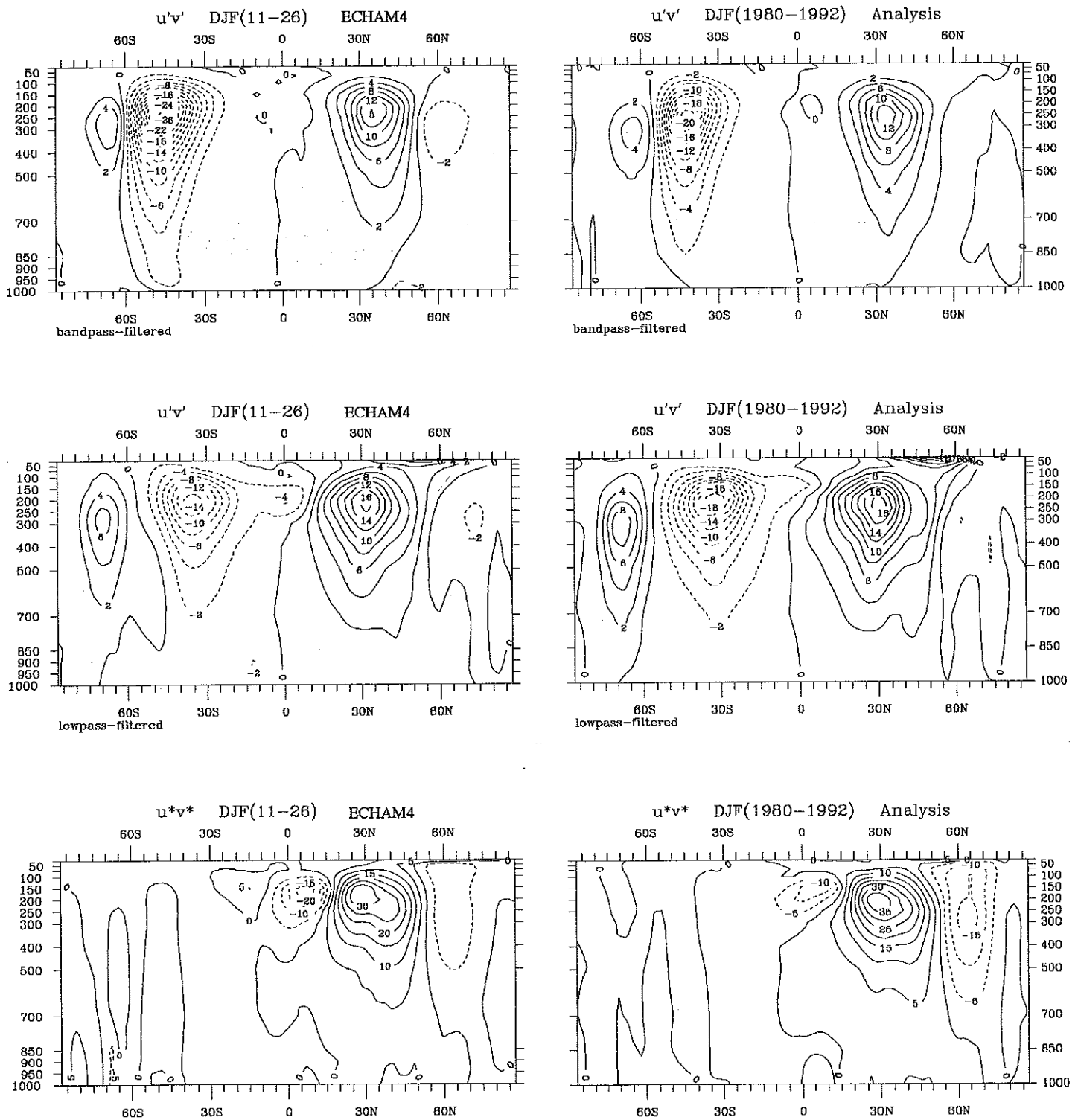
Figure 25   Latitude-height (pressure in hPa) distributions of zonal mean northward transport of
           sensible heat (Km/s) by transient eddies (top: bandpass regime; middle: lowpass
           regime) and stationary eddies (bottom), respectively.
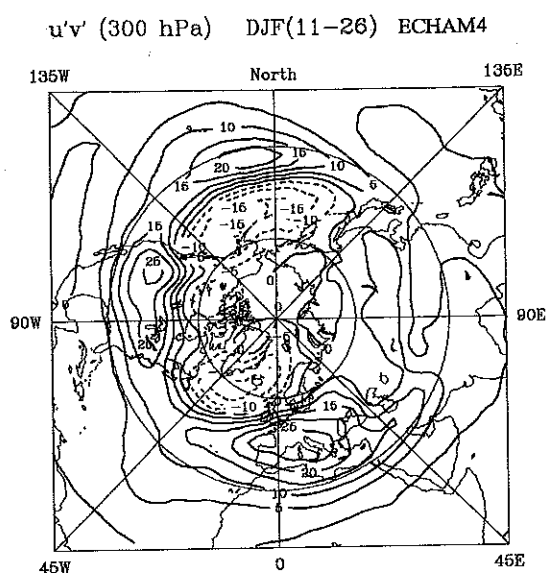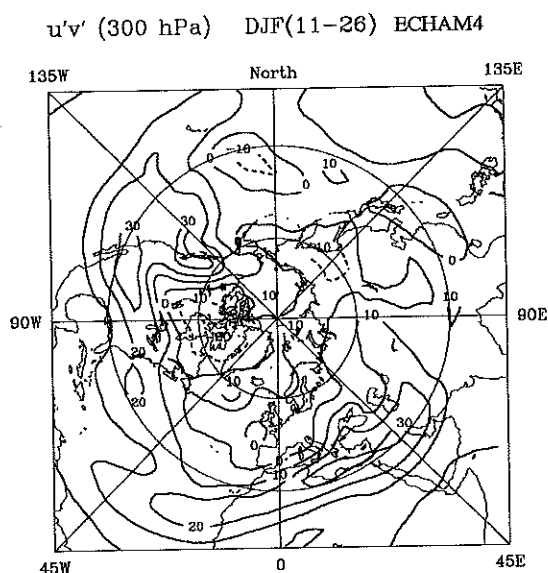   Left: ECHAM-4 (mean of two realizations). Right: ECMWF analysis (1980-1992).
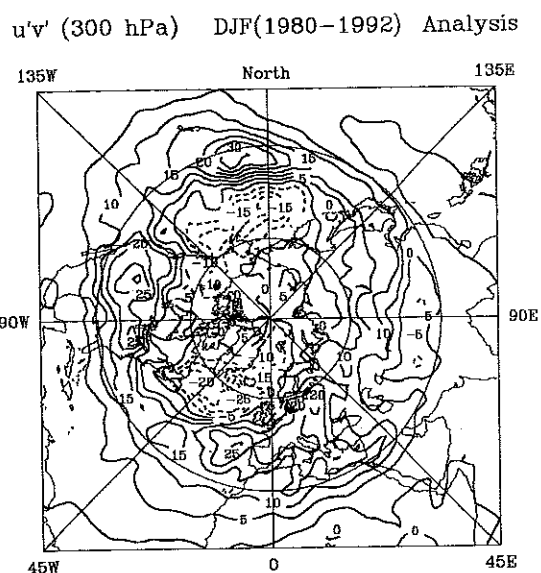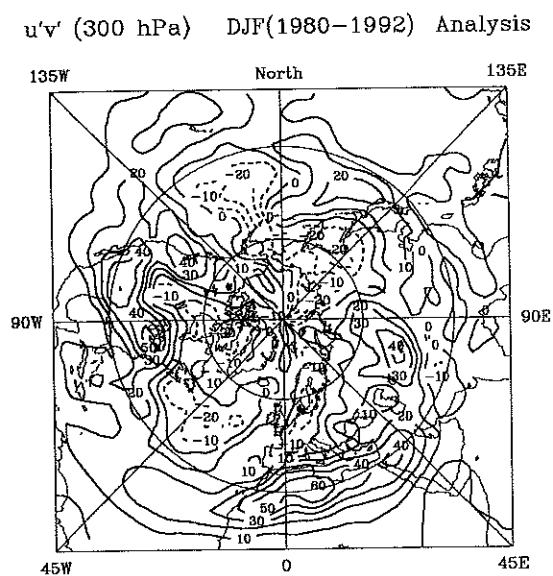
85

v'T' (850 hPa)   DJF(11−26) ECHAM4

bandpass−filtered

v'T' (850 hPa)   DJF(1980−1992) Analysis

bandpass−filtered

v'T' (850 hPa)   DJF(11−26) ECHAM4

lowpass−filtered

v'T' (850 hPa)   DJF(1980−1992) Analysis

lowpass−filtered
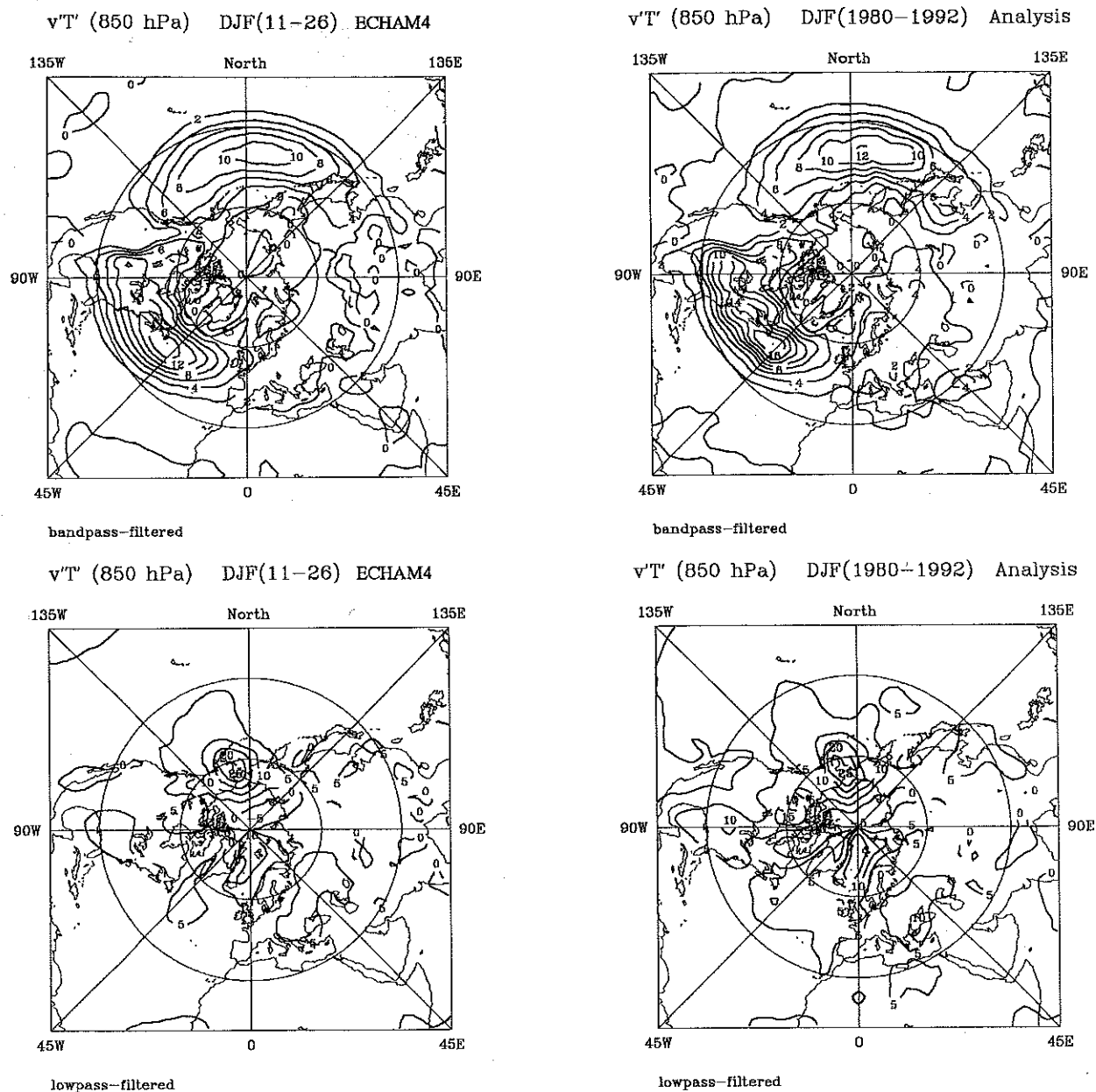
Figure 26   Northward transport of sensible heat (Km/s) by transient eddies at 850 hPa in the
bandpass regime (top) and lowpass regime (bottom), respectively.
Left: ECHAM-4 (mean of two realizations). Right: ECMWF analysis (1980-1992).
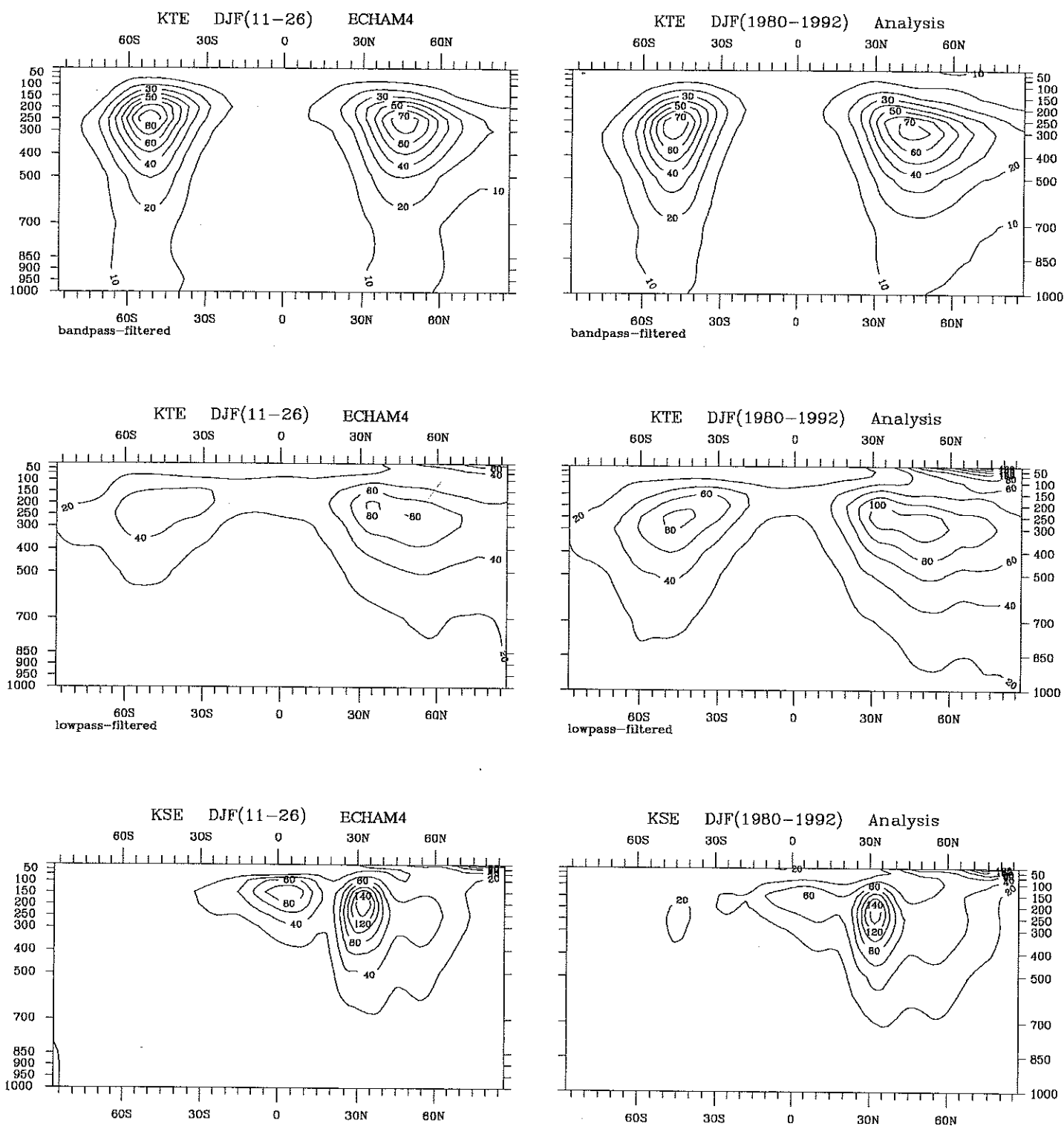
Figure 27 Latitude-height (pressure in hPa) distributions of zonal mean northward transport of westerly momentum (m²/s²) by transient eddies (top: bandpass regime; middle: lowpass regime) and stationary eddies (bottom), respectively.
Left: ECHAM-4 (mean of two realizations). Right: ECMWF analysis (1980-1992).

u'v' (300 hPa)   DJF(11—26) ECHAM4

bandpass—filtered

u'v' (300 hPa)   DJF(1980—1992) Analysis

bandpass—filtered

u'v' (300 hPa)   DJF(11—26) ECHAM4

lowpass—filtered

u'v' (300 hPa)   DJF(1980—1992) Analysis

lowpass—filtered

Figure 28   Northward transport of westerly momentum (m^2/s^2) by transient eddies at 300 hPa in the bandpass regime (top) and lowpass regime (bottom), respectively.
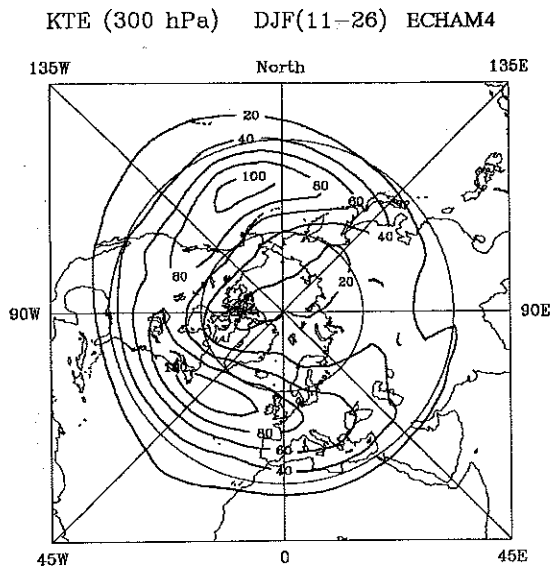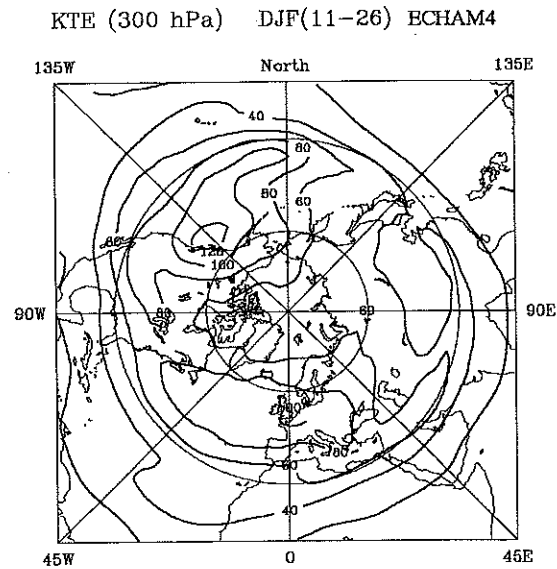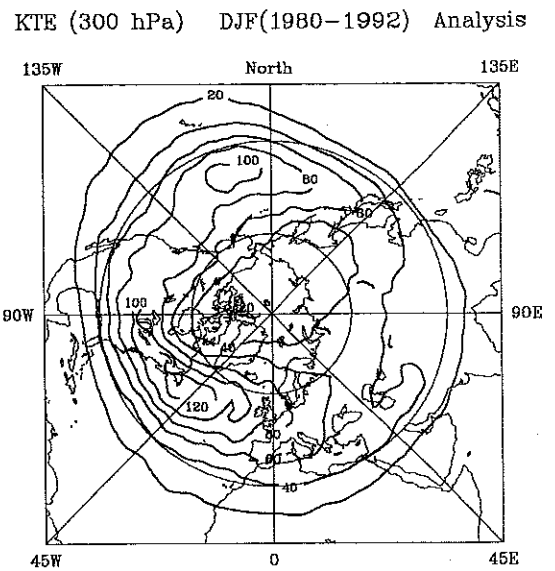Left: ECHAM-4 (mean of two realizations). Right: ECMWF analysis (1980-1992).

Figure 29   Latitude-height (pressure in hPa) distributions of zonal mean transient eddy kinetic energy in the bandpass regime (top) and lowpass regime (middle), and stationary eddy kinetic energy (bottom), respectively. Units: m^2/s^2.
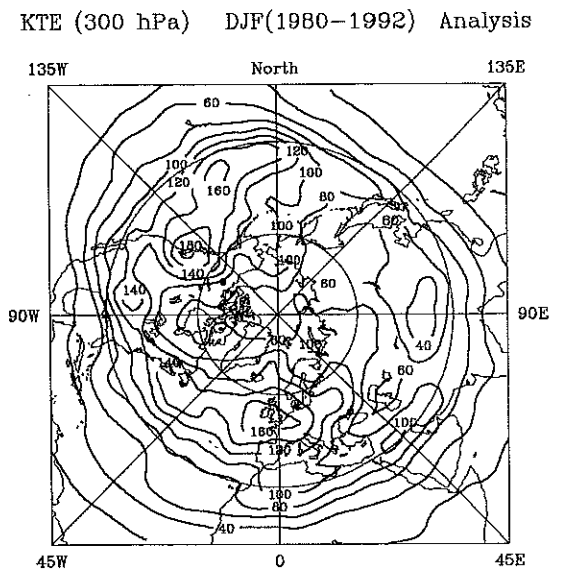Left: ECHAM-4 (mean of two realizations). Right: ECMWF analysis (1980-1992).

KTE (300 hPa)   DJF(11–26) ECHAM4

KTE (300 hPa)   DJF(1980–1992) Analysis

bandpass–filtered

bandpass–filtered

KTE (300 hPa)   DJF(11–26) ECHAM4

KTE (300 hPa)   DJF(1980–1992) Analysis

lowpass–filtered

lowpass–filtered

Figure 30   Transient eddy kinetic energy (m^2/s^2) at 300 hPa in the bandpass regime (top) and lowpass regime (bottom), respectively.
Left: ECHAM-4 (mean of two realizations). Right: ECMWF analysis (1980-1992).